UNIVERSITY OF LIVERPOOL

Characterisation of Junctions in Molecular Electronics

Thesis Submitted in accordance with the requirements of the University of Liverpool for the degree of Doctor of Philosophy

by

SAMAN NAGHIBI

May 2022

Acknowledgement

It was a long journey, and I met so many wonderful people along the way. Some of those folks provided me with the best support I could have asked for, and I cannot express my gratitude in words.

I begin with my supervisor Professor Richard Nichols, a true gentleman who has been patient and supportive from the start. Richard has given me the confidence and motivation I needed to complete my PhD. He was constantly present and gave me the freedom to manage my time. Richard, I am not exaggerating when I say you are the best mentor I have ever had, so thank you so much for all your fantastic support when I needed it the most.

Dr Andrea Vezzoli, a wonderful friend, teacher, supporter, and honest critic. Thank you for listening to me and answering all my silly questions for the past few years. Just seeing your hard work has been enough inspiration for me, but you have always gone above and beyond with your incredible support and kindness. You are a wonderful person, and as I've always said, I couldn't have finished my PhD without you.

My mum and dad, the ones who have always stood behind me and given me everything they have. I cannot express my appreciation in a single paragraph because I have so much to say about your generosity. My mother, who has taught me to love myself and others, had always supported me, laughed with me, and cried with me when I was upset. Mum, you are a beautiful person, and I adore you. My father, a kind man who has given up on so many things to help me succeed. You have given me courage and strength, and I am so proud of you every time I look back. You're a great father, as well as a

wonderful pilot. So, to both of you, thank you so much for everything you have given me, for which I will be forever grateful. I love you so much.

My lovely sister, you have always been there for me. We have grown up together and shared many incredible memories. I learn from you every day because you are hard-working and encouraging. Thank you so much for helping me get this far and inspiring me to keep going. I will need you forever as I still have a lot to do, and you always show me the best way. I consider myself fortunate to have you because you are the best sister and lawyer in the world.

My aunt and uncle, cousins, and their families. You have been a tremendous help to me, and this PhD would have been much more difficult without your assistance. You have been very giving and kind, and I have felt safe because of you all in the UK as my family. It is impossible to express my gratitude in a few words, but I am grateful for all of your incredible help.

Katrina, my best friend, a genuinely nice human being who has always been there for me. I consider myself so lucky to have you in my life as I cannot imagine how I would deal with the challenges without you. You always make me laugh, which helps me forget about my difficulties. Thank you for your encouragement and support, Kat. We still need to go to Amsterdam together soon.

It is not always simple to put things into words, especially when it comes to Sean. You know that you are more than just a friend. You are an excellent person who makes me happy, even though you sleep a lot, and I need to come up with a treatment to stop that. We have had a great time together, and I'm

sure we will have many more in the future. Thank you for your support and presence when I needed it.

Professor Martin Feelisch, a superb teacher who helped me obtain my PhD position. I am incredibly grateful for all your assistance and support. Working in your group at the University of Southampton was one of the most fortunate experiences of my life.

It has been fantastic to make so many friends while working on my PhD. I am grateful to Edmund, Xiaohang, Jonathan, James, Alex, Chuanli, David and Nicolo for their encouragement and kindness.

I also want to thank our colleagues at the University of Zaragoza, Lucia Herrer, Ivan Martn, Jose Mara Bonastre, Santiago Martn, Jose Luis Serrano, and Pilar Cea, as well as the University of Western Australia, Varshini Kumar, and Paul Low, and the University of Warwick, Sara Sangtarash, and Hatef Sadeghi.

I would like to thank the Royal Society of Chemistry, Apple Inc., and the University of Liverpool for their assistance during my PhD.

Saman Naghibi
Liverpool, May 2022

Abstract

Single-molecule electronics is a field of nanoelectronics in which the electronic components are single molecules. It combines engineering, physics, and chemistry expertise to realise circuit parts at the limit of miniaturisation. A number of approaches for measuring the charge transport characteristics of single molecules have been developed since a single molecule may behave as an effective electronic component. Mechanically controllable break junctions and scanning tunnelling microscopes have been used to study the electronic transport properties of single-molecule junctions. The most common method for studying the electronic characteristics of single-molecule junctions is the scanning tunnelling microscope-based break-junction (STM-BJ) technique.

In the first part, various pyrrolodipyridines (carbazole-like) molecular wires were studied and modified. By chemically controlling the bridging nitrogen atom in the tricyclic ring structure, it is possible to vary the electrical conductance and quantum interference patterns. Eight distinct N-substituted pyrrolodipyridines were produced and tested utilising an STM break junction for single-molecule electrical characterisation. The importance of the pyrrolic nitrogen in enabling conductance over the chemical bridge and managing quantum interference is shown by correlations of these experimental results with theoretical calculations. The considerable chemical modulation seen in the meta-connected series is absent in the para-series, indicating a rivalry between (a) meta-connectivity quantum interference processes and (b) the

pyrrolic nitrogen's ability to assist conductance, which can be regulated by chemical substitution.

In the second part, charge transport in an oligophenyleneethynylene molecular junction mediated by host-guest interactions with pillar[5]arenes was studied. For oligophenyleneethynylene, intermolecular conductance pathways arises in the junction due to π stacking between molecules. The pillar[5]arene can be used to form a "molecular sheath" around the OPE, preventing dimeric connections from forming by separating and restricting the interaction between single-molecule wires. Excellent performance of pillar[5]arene in hosting molecules in their cavity can help the development of single-molecule supramolecule studies, as well as inspire a variety of creative designs of molecular electronic systems around intermolecular interactions.

In the last part, molecular junctions were formed with the organic 6-oxo-verdazyl radical using the scanning tunnelling microscope break-junction process. Even at ambient temperature, the verdazyl moiety remained stable within the junction, and electrochemical gating allowed in-situ reduction of the verdazyl radical to its the anionic state in a single-molecule transistor design. Due to bias adjustment, changes in the resonances of the radical molecule with regard to the Fermi levels of the metallic electrodes was observed. At room temperature, single molecules of verdazyl were able to sustain their radical behaviour, exhibit transistor-like switching behaviour, and rectification. These characteristics open the path for more research into the electrical and magnetic properties of radical in molecular junction.

Table of Contents

Table of Figures

List of Tables

List of Acronyms and Synonyms

LB	Langmuir-Blodgett
STM	Scanning Tunnelling Microscopy
I-V	Current-Voltage
SAM	Self-Assembled Monolayer
MCBJ	Mechanically Controlled Break Junction
NDR	Negative Differential Resistance
AFM	Atomic Force Microscopy
MO	Molecular Orbital
HOMO	Highest Occupied Molecular Orbital
LUMO	Lowest Unoccupied Molecular Orbital
M	Metal
OPI	Oligophenyleneimine
FN	Fowler Nordheim
G	Conductance
Γ	Electrode-Molecule Coupling
Φ	Barrier Height
QI	Quantum Interference
T(E)	Transmission Coefficient
E_F	Fermi Energy
pKa	Acid Dissociation Constant
I(s)	Current-Distance
CB	Cucurbituril

P5A	Pillar[5]arene
OPE	Oligophenyleneethynylene
BJ	Break-Junction
SOMO	Singly Occupied Molecular Orbital
DFT	Density Functional Theory
LUSO	Lowest Unoccupied Singly Orbital
HOSO	Highest occupied spin orbital
Pt	Platinum
Ag	Silver
Cl	Chlorine
Fe	Iron

CHAPTER 1

INTRODUCTION

1.1. Molecular Electronics

A primary focus of molecular electronics is the study of the electrical properties of materials at the molecular level, especially their charge transport behaviour and quantum effects. In recent years this has included electrical characterisation of single molecules and single nanostructures. In the case of single molecules this has provided a platform to quantify the energy gap between the molecular orbitals and the Fermi level of the metallic electrodes, the molecule-electrode coupling, charge transport mechanisms in the molecules and thermoelectric properties. Such measurements can help in the design of organic and inorganic molecular targets with multifarious electrical properties when contacted in electrode junctions. [1,2]. Organic electronics, on the other hand, is a more established field of contemporary electronics that deploys and studies organic materials such as conducting polymers and bulk molecular and nanostructured materials [3]. Here organic electronics contributes to the design of electrical and optoelectrical devices that take advantage of the macroscopic features of organic materials [4]. So far, the most successful commercial products in this field include organic photovoltaic (PV) devices, organic light-emitting displays, light-emitting diode displays (LED), liquid crystal displays (LCD), organic transistors, [2] infrared imaging, and biochemical sensors [5]. On the other hand, applications of molecular electronics are early stage, but sensors which can electrically detect single molecules are a promising avenue. There are various developments in this respect including carbon nanotube sensor devices which have been deployed

to analyse the activity of a single enzyme molecule connected to a nanotube in real-time [4].

Although organic electronics has had very great technological success the replacement of traditional semiconductor device electronics with molecule electronics is very far from reality. However, the importance of molecular electronics can be seen by its contribution to the understanding of charge transport through molecules and across interfaces. These advances in understanding have been facilitated by the use of techniques such as break junction STM or large area junctions. Experimental and theoretical advances have ensured that this field has emerged as a rapidly developing area of nanoscience, demonstrating the interdisciplinarity of the topic [2].

Understanding charge transport in single-molecule has important applications across a wide variety of academic fields including in chemistry, materials science, physics, and biology. An example of the latter is the detection of DNA, proteins, and antibodies binding, which can be used to observe the activity of enzymes significant in biology [4]. In chemistry one application area has been the application of single-molecule electrical methods in electrochemistry. Single molecule techniques can detect, manipulate, and [2] characterise the faradaic response of individual redox molecules [6], as well as to regulate molecular conduction via gate electrodes in single-molecule experiments employing electrochemical control [7]. Single molecule measurements can be performed over a wide range or environments (UHV, ambient, solution, electrolyte, ionic liquids etc) and temperature (from ultra-low to over ambient). However, it should be noted that single-molecule

conductance measurements are a challenge in terms of reproducibility. Forming a reliable single molecule in the junction between the metallic electrodes is not straightforward and doing it consistently is considerably more challenging [8]. However, the insights afforded by such methods into charge transport is very significant and single-molecule electrical measurements and associated theory are growing areas of research.

1.2. History of Molecular Electronics

The innovation of the transistor and the introduction of subsequent circuits in the 1950s revolutionised electronics. In 1956 a German scientist, Arthur von Hippel, initiated a basic molecular engineering approach [9]. This concept introduced by Hippel lead initiated the first steps into molecular electronics [10]. Molecular electronics, as is studied today, can be traced back to the end of the 1960s and early 1970s, when various groups started studying electronic transport through molecular monolayers. For example, Hans Kuhn discovered a novel method to fabricate Langmuir-Blodgett (LB) films for molecular electronics measurements. This approach placed these LB monolayer films in a sandwich configuration between metal electrodes, enabling measurement of the junctions' electrical conductivity [3]. Later, Ari Aviram studied molecules designed with the aim of conferring rectifying properties to molecular electronic junctions. Here the target molecule featured an electron donor (tetrathiafulvalene) and an electron-accepting group (tetracyanoquinodimethane), with these two groups being separated by an insulating bridge to prevent coupling between their π levels [11]. This was a

major advance in the theoretical development of molecular electronics concepts, although Aviram's idea remained a hypothetical concept for many years until it could be demonstrated experimentally.

The innovation of scanning tunnelling microscope (STM) by Gerd Binnig and Heinrich Rohrer in 1981 opened new doors for many subject areas, including surface chemistry and physics, nanoscience, catalysis, and eventually also molecular electronics, where it provided the realistic opportunity to study single molecules and their electronic transport properties. Atomic-sized metallic contacts were an important development in nanoscience in the late 1980s[12,13], and this was to latter play an essential role in nanoelectronics. Such atomic scale metallic wires provided the platform for contacting molecules for electrical characterisation down to the single molecule level. The connection between the quantum properties of single atoms and molecules and macroscopic current-voltage (*I-V*) response of the electrical circuits is a vital aspect of molecular electronics [14].

In 1988 Aviram and collaborators used a scanning tunnelling microscope to measure the *I-V* characteristics of an hemiquinone-catechol molecule. They studied switching and rectifying features of the molecule by preparing self-assembled monolayers (SAMs) on gold substates and performed the measurement using a platinum tip to collect *I-V* scans in different substrate areas. In very flat areas of the substrate, only asymmetric Au-Pt junctions were recorded, while in the rough areas where the molecules are adsorbed, considerably different junction responses were seen. Their results featured a current peak at -200 mV as the bias voltage was scanned in the negative

direction. This only occurred in the negative scans which was taken as evidence of a rectifying behaviour, akin to that predicted in 1974. They concluded that the catechol moiety behaves as an electron donor, and hemiquinone behaves as an acceptor and this conveys the rectification to the molecular junction [14].

The earliest charge transport experiment in single-molecule junctions was conducted in 1997. Reed, used a mechanically controlled break junction (MCBJ) technique to make a junction of benzene-dithiol between gold electrodes. They prepared a SAM of benzene-dithiol on gold by putting a gold wire in a solution of benzene-dithiol in tetrahydrofuran until breakage took place, and as a consequence, two tips of atomic sharpness covered with the benzene-dithiol monolayer were formed. They left the solvent to evaporate in an argon atmosphere, and a piezo controlled bendable substrate was used to bring the tips together to run I-V scans [14]. Other important innovative work was performed by Reed, who developed a nanopore technique for fabricating metal SAM heterojunctions. These nanopore devices were used to study the rectifying behaviour of the molecule junctions [15]. Molecular junctions also exhibiting negative differential resistance (NDR) electrical signature also came into focus. In this time period, Stoddart. showed that rotaxane and catenane junctions could behave as reconfigurable switches [16,17] in crossbar junctions. In these junctions the molecular material is sandwiched at the crossing point of overlaid metallic leads, giving a platform for direct electrical characterisation. However, it was not until the next decade that the STM and

conducting AFM were developed for making electrical measurements on single molecules.

1.3. Scanning Tunnelling Microscope

A scanning tunnelling microscope (STM) is one of the most advanced instruments available for forming contacts and junctions at the atomic and molecular scale [18]. In the standard operation of an STM the tip is held at a very close distance to the metallic substrate and a small tunnelling current flows between tip and surface on application of a bias potential. For an empty tunnelling junction, the current decreases exponentially as the tip is withdrawn away from the sample surface. Alternatively, the metallic tip can be driven into the metallic substrate and then withdrawn to make atomic size contacts. Repeating the indentation of the metallic tip into the surface can "anneal" and clean the metallic contacts even under ambient conditions and can help in the formation of good quantity atomic junctions.

High speed and versatility are the most significant advantages of the STM. However, as the atomic size contact is formed while withdrawing the tip from the substrate, measurement of the exact atomic configuration of the contact is not possible [19]. Compromised stability when changing external variables such as temperature, magnetic field and electrochemical potential, and the short lifetime of the contacts due to the sensitivity of the STM to the vibrations are the main disadvantages of the instrument. Recently ultra-high vacuum STMs that work with high stability at very low temperatures and strong magnetic fields are widely available [19]. However, these have disadvantages that they

cannot be applied under ambient or solution conditions or with electrochemical control.

In the STM, the tip is typically manually approached to the substrate using some form of stepper motor [20]. A bias is applied between the tip and the substrate and the z-piezo is expanded to approach the tip to within electron tunnelling distances of the substrate. The piezo approach stops when the desired set-point current is obtained. At this stage, the separation of the tip and substrate is typically between 5 to 15 Å [21]. To control the movement of the tip precisely, the piezo drive is used to control the tip on the three axes in the tunnelling regime. Constant current mode and constant height mode are the two methods of imaging a surface using STM. In the former method, the feedback loop keeps the current constant during scanning, and the outcome is a plot of tip movement with respect to the substrate [21]. In the latter method, which is suitable for very flat surfaces, the feedback loop keeps the height of the tip constant during scanning, and the outcome is a plot of current [21].

1.4. Charge Transport Properties in a Single Molecule

Energy levels (molecular orbitals (MOs)) are quantised in molecules, while energy-band dispersion of bulk materials is continuous and condensed. [22]. There is an energy gap between the highest occupied (HOMO), and the lowest-unoccupied molecular orbital (LUMO) called the HOMO-LUMO gap. The HOMO-LUMO gap differs from molecule to molecule, just as the Fermi level of bulk electrodes differs from metal to metal [22]. While

establishing a reliable molecule-electrode attachment is challenging, the successful formation of the molecular junction between two metallic electrodes can lead to the transition from discrete molecular states to more continuous states, resulting from hybridisation between molecular orbitals and electronic states of the substrate [23].

Different mechanisms for the current flow through molecules have been recognised, including coherent and incoherent tunnelling, hopping, and Fowler-Nordheim tunnelling [24–29]. Understanding and controlling the physics of charge and energy flow at the molecular level are fundamental challenges in molecular electronics. A molecule contacted to two metallic electrodes provides an excellent platform to study charge dynamics on the nano-scale [30–33]. A single orbital connected to two metallic leads is a simple model for capturing the crucial physics of charge transfer across a single-molecule junction (Figure 1.1) [30].

A single-level model contains a molecular orbital contacted to the two metallic electrodes. Figure 1.1 shows a molecular orbital coupled with leads on the left and right, and there is no direct coupling between the electrodes. By applying a bias voltage, electrons transfer from the Fermi level of the left lead to the molecular orbital and then transfer to the drain (right lead).

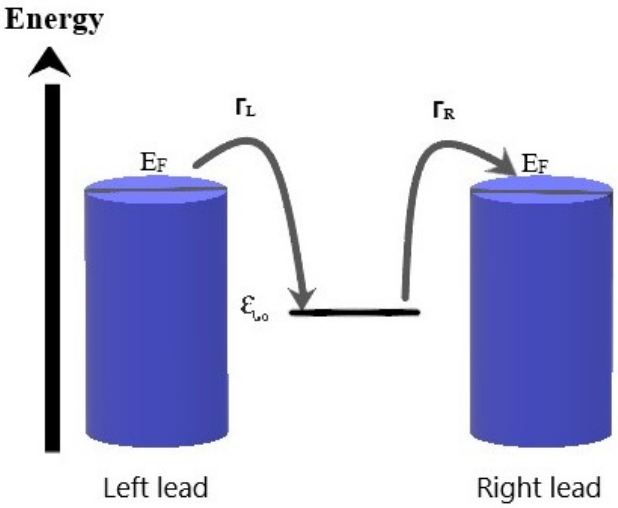

Figure 1.1. Here there is no direct coupling between the leads in this single-level model for a molecular orbital coupled to two leads. E_F is the lead Fermi energy, ε_0 is the orbital energy, and Γ_L is the coupling between the molecular orbital and left electrode and Γ_R is the coupling between the molecular orbital and right electrode.

In Figure 1.1, E_F is the Fermi level of the metallic contacts, ε_0 is the orbital energy and Γ_L and Γ_R are the coupling between the molecular orbital and left and right lead, respectively. If the coupling is symmetric $\Gamma = \Gamma_L = \Gamma_R$, the conductance is:

$$G = G_0 \frac{\Gamma^2}{(E_F - \varepsilon_0)^2 + \Gamma^2} \qquad \textit{Equation 1}$$

Here E_F is the junction Fermi energy, and G_0 is the quantum conductance. Charge transport takes place through the highest occupied molecular orbital (HOMO) when $E_F - \varepsilon_0 > 0$ or the lowest unoccupied molecular orbital (LUMO) when $E_F - \varepsilon_0 < 0$. This basic model gives a reasonable understanding of the actual transmission mechanism in the junction [30]. In asymmetric coupling, $\Gamma_L \neq \Gamma_R$, the molecule is coupled more robustly to either the left or

right contact. Assuming that the left contact is coupled more to the LUMO of the molecule ($\Gamma_L > \Gamma_R$), the current I and the LUMO occupancy n can be found using the equations 2.

$$I = \frac{2G_0\Gamma_s\Gamma_t}{e(\Gamma_s+\Gamma_t)}\left[arctan\frac{2\varepsilon_0+eV}{\Gamma_s+\Gamma_t} - arctan\frac{2\varepsilon_0-eV}{\Gamma_s+\Gamma_t}\right] \qquad \textbf{\textit{Equation 2}}$$

Here, e is the elementary charge. Contributions from the substrate and the tip play an essential role in the LUMO occupancy n of the molecule in a biased junction [34]. In equation 2, Γ_s and Γ_t represents the coupling of the molecule to the substrate and the tip. Asymmetric coupling of the molecule to the electrode can impart rectifying properties, so the conductance at a given positive voltage would be different from the conductance at the same, but negative voltage. Quantification of the asymmetric coupling originating from measurements of transport is not necessarily straightforward, but the single level model provides a basic theoretical framework.

In metal-molecule-metal junctions, the Fermi level alignment is an essential factor in defining the charge transport mechanism. [35]. At thermal equilibrium, when a metal is in contact with a molecule, the Fermi levels in the two materials must be equal. The HOMO-LUMO gap is usually several electron volts [36]. Typically, at least for tunnelling transport, the Fermi level of the metallic electrodes locates close to the centre of the HOMO-LUMO gap and does not energetically align with them at zero bias [37]. The difference in the energy level results in a contact barrier, and depending on the height of this barrier, charge transport in the junction shows different behaviours [38]. The

gap between the metal work function, Φ_m, (the energy difference between the metal Fermi level and the vacuum level) and the electron affinity, X, of the molecule (the energy difference between the molecule conduction band edge and the vacuum level) is the barrier height, Φ_{Bn}. (Figure 1.2).

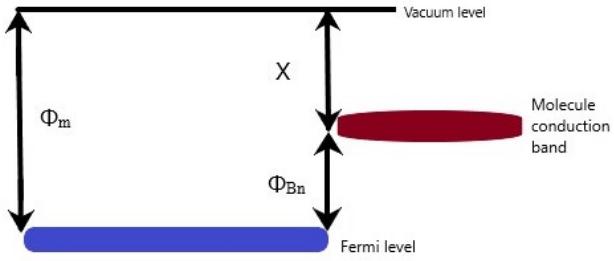

Figure 1.2. Under thermal non-equilibrium conditions, the energy band diagram of metal close to the molecule.

At the nanoscale, an electrical circuit does not follow Ohm's law, and this is most simply illustrated by considering chain of single metal atoms, such as those formed in mechanically-controlled break-junction (MCBJ) experiments with gold contacts. In systems with macroscopic dimensions, the resistance has a linear correlation with the length of the wire. On the other hand, at nano-scale limits, for example, a chain of single metal atoms, the resistance is unaffected by the length of the wire, since the resistance is quantised in units of $h/2e^2$. In a typical measurement using scanning tunnelling microscope (STM), when a metallic contact with a single or few metal atom widths is broken, the conductance can be observed to be quantised. By slow retraction of two metallic electrodes in contact, the whole contact area experiences structural rearrangement until it ends up with its final stages with only a few bridging atoms [39]. The conductance of a single chain of metal atoms with one

conductance channel is close to $2e^2/h$. This value is referred to as one quantum unit of conductance. Yanson, presented an example of a conductance histogram from data that involved stretching a gold nano-contact using a mechanically controlled break-junction (Figure 1.3). The conductance drops in a series of marked vertically descending steps. Rearrangement of the atomic structure causes these steps [40,41]. The conductance of the last plateau for monovalent metals (e.g. lithium, sodium, potassium) is close to $1G_{0,}$ and this plateau originates from a single atom contact. This is also the case for other metals such as gold (Figure 1.3). The contact can be stretched to form a chain of single atoms over distances of up to 20 Å (Figure 1.3).

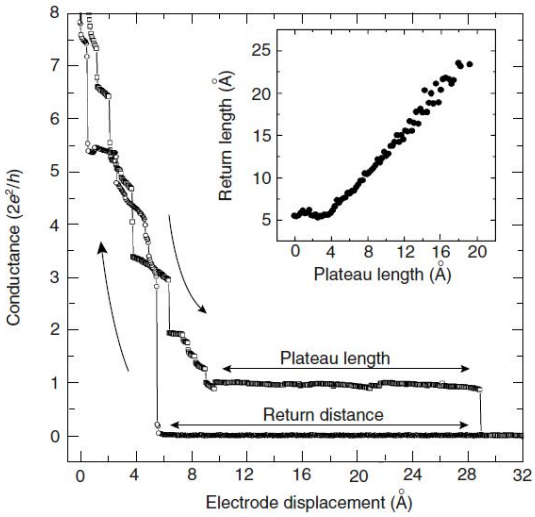

Figure 1.3. In an MCBJ, conductance is a function of the separation of the two gold electrodes. The traces begin at higher conductance values, and then following a jump that opens a tunnelling gap, a prolonged plateau with a conductance close to 1 G0 is seen. Figure is taken from A. I. Yanson, Formation and manipulation of a metallic wire of single gold atoms, NATURE, VOL 395, 1998.

1.4.1. Quantum Tunnelling

Electron tunnelling is a quantum mechanical phenomenon involving a particle going through a barrier that is classically considered the forbidden area [42]. A straightforward example of classical mechanics would be a ball with kinetic energy (the energy it possesses due to its motion) of 100 J rolling on a flat surface. The ball now faces a hill and acquires potential energy of 10 J at the top of the hill. In this case, the ball can rollover the hill without any difficulty. In classical mechanics, the possibility of the ball rolling over the hill in this circumstance is 100%. On the other hand, if the ball encounters a higher hill and the ball's potential energy on top of that hill is 200 J, the ball will roll partially up the hill, stop, and then return down. In this case, the possibility of having the ball surmounting the hill is 0 %. Since, in this case, the ball cannot progress beyond the hill, this is classed as energetically forbidden. Now consider the quantum mechanical situation where a wave function now describes the ball. This wavefunction might be localised, but it would be suddenly observed on the other side of the hill if it encounters the hill. When the wavefunction of a bound state with energy E meets a barrier with potential energy V_x, the wavefunction extends beyond the limits of classical motion into the region where $V_x > E$. This phenomenon by which the quantum particle can be found in the classically forbidden area is called quantum tunnelling. Quantum mechanics allows the particle to penetrate the barrier and then come out from the other side. This procedure relies on the probability of a quantum object, for example, an electron, to tunnel through a

barrier since the particle also has wave characteristics [43]. By such means, tunnelling electrons can travel between two metallic electrodes when they are sufficiently close. An effective insulating medium between the electrodes raises the height of the potential barrier between the electrodes. If the insulation thickness is small enough, the current can still flow from one electrode to another [44,45]. The height of the barrier (ϕ), the barrier width (s), and the decay of the wave function within the barrier are essential parameters in the tunnelling.

Simmons suggested a theory in which an electrical current can pass through an insulating barrier between two metallic electrodes under two conditions: 1) electrons of the metallic electrodes have adequate energy to overcome the potential barrier and pass between two conduction bands and 2) the barrier must be small enough to let electrons travel through it [46,47]. The Simmons' model has been widely used in molecular electronics due to its relative simplicity. This model, and it has been widely used in the analysis of tunnel barriers [28,48]. Here, the voltage and current density in a junction is:

Equation 3

$$J = \frac{qA}{4\pi^2 hs^2}\left(\phi - \frac{eV}{2}\right).exp\left(-\frac{2s\sqrt{2m}}{h}\sqrt{\phi - \frac{eV}{2}}\right) - \left(\phi + \frac{qV}{2}\right).exp\left(-\frac{2s\sqrt{2m}}{h}\sqrt{\phi + \frac{eV}{2}}\right)$$

Where s is the width of the barrier, A is the junction area, m is the mass of electron, ϕ is the height of barrier, e is the electron charge and V is the applied bias [4746].

Imagine two metal electrodes separated by an insulator with a layer thickness *s* between them. When the two electrodes are subjected to the same potential, the system is said to be in thermodynamic equilibrium, and their Fermi levels are the same, i.e., $\phi_1 = \phi_2$ in Figure 1.4 [46,47].

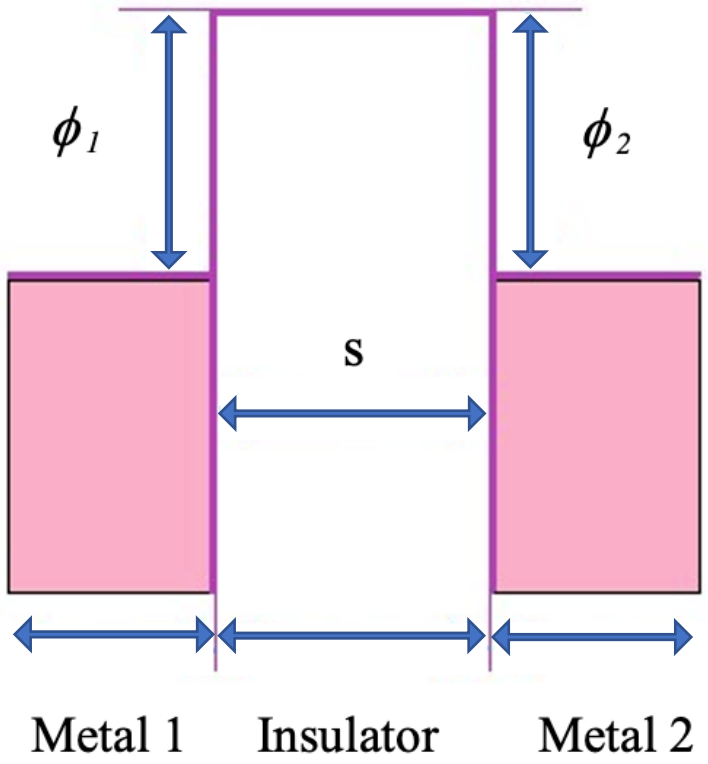

Figure 1.4. Potential barrier in the metal-insulator-metal of system with a rectangular shape of the barrier between the electrodes when the system is at equilibrium.

In case of very small voltages where $\overline{\phi} \gg eV$, where the averaged barrier is $\overline{\phi} = \frac{\phi_1+\phi_2}{2}$, it is possible to assume $\overline{\phi}$ is independent of V, so the tunnelling current is linearly proportional to the voltage (Figure 1.4) [47], [46].

However, if the potentials of the electrodes are different, current flow between them is possible. Figure 1.5 depicts the energy diagram of electrodes with a bias energy of eV applied to them. In case of intermediate bias voltages where $eV \leq \phi_2$ and the average barrier height is $\overline{\phi} = \frac{\phi_1 + \phi_2 - eV}{2}$, the potential barrier between the metallic electrodes has a trapezoidal shape showing the asymmetry of the barriers [46,47].

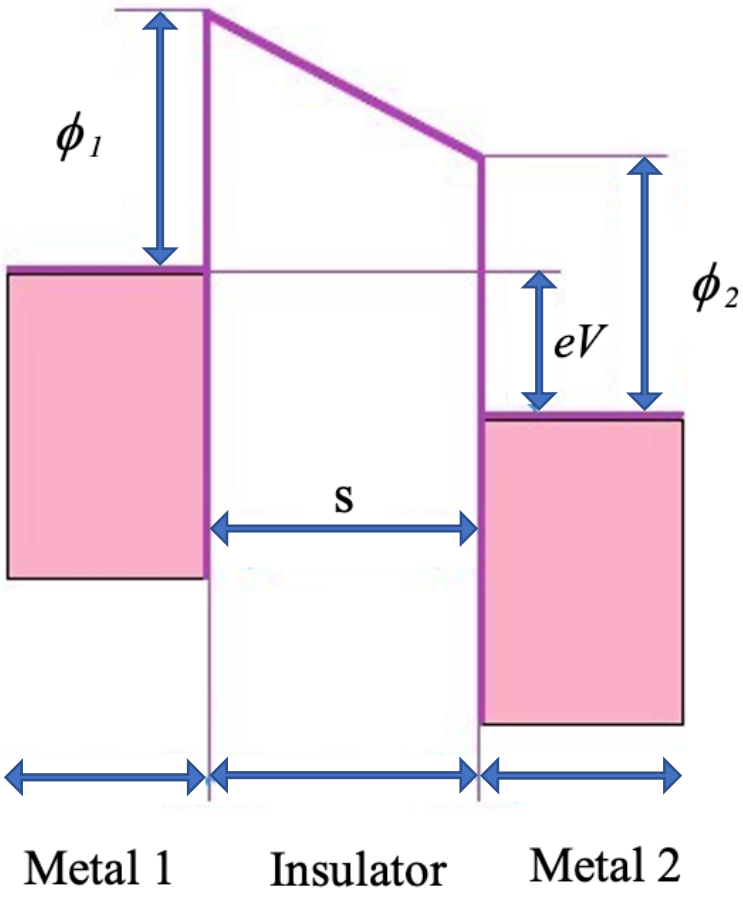

Figure 1.5. Potential barrier in the metal-insulator-metal of system with trapezoidal shape of the barrier between the electrodes when $eV \leq \phi_2$.

At high voltages (field emission mode) $eV > \phi_2$ the average barrier height is $\frac{\phi_1}{2}$. Under this condition, the barrier between metallic electrodes is triangular (Figure 1.6) [47], [46].

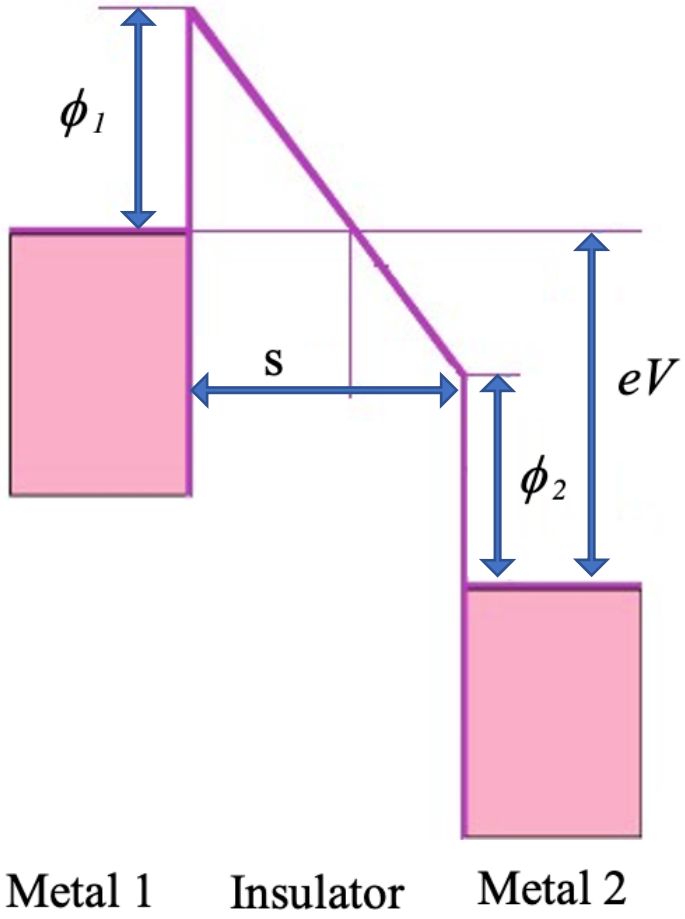

Figure 1.6. Potential barrier in a metal-insulator-metal system with a triangular shape of the barrier between the electrodes when $V \gg \phi_2$.

In case of very high voltages where $eV \gg \phi_2$, the Fermi energy of electrode 2 is located very far beneath the conduction band of electrode 1. Under this circumstance, tunnelling of the electrons from electrode 2 to 1 is impossible as every available level in metallic electrode 2 is empty, so this situation is similar to the field emission from a metallic electrode, and equation 3 can be

written in a shorter form of the well-known Fowler-Nordheim tunnelling equation (explained in Section 1.3.2.5) form [46,47]:

$$J \propto V^2 \exp\left(-\frac{4d\sqrt{2m}\phi^{\frac{3}{2}}}{3qhV}\right) \qquad \textbf{Equation 4}$$

In some circumstances, this model may not be appropriate since it gives a simple description of tunnelling, and it also ignores hopping and superexchange processes [46,47,49]. When applying the model, it is crucial to define different conditions under which it can be used and its constraints. Two main limitations of the Simmons' model are: 1- The potential is spatially averaged and 2- A linear relation between applied voltage and potential change.

The Simmons' model relies on averaging the potential-thickness profile of the barrier $\phi(V,x)$, which leads to a distinctive parameter known as an averaged barrier potential $\overline{\phi}(V)$. Simmons considers the potential barrier should be averaged when the junction is introduced to a bias, and one considerable drawback of this assumption is that the model neglects the asymmetry present between the barrier heights at the two electrodes. Regardless of the restrictions of Simmons model, it has the advantage of simplicity in comparison to other models with more complicated mathematical structures [50].

Having established that tunnelling is one of the main conduction mechanisms in molecular electronics, it is feasible to obtain current density, barrier height and other transport parameters for direct tunnelling when $V < \phi_2/e$ from the Simmons model using the equation 4 [46,48,49].

1.4.2. Charge Transport Mechanisms

1.4.2.1. Coherent Tunnelling

Coherent tunnelling is a process in which electrons are transmitted through a structure without any phase-coherence breaking events. The term "coherent" refers to the absence of interactions with the environment [51]. In a molecular wire with no or negligible scattering, coherent tunnelling can take place.

A wire with no scattering is called ballistic, and a length of a ballistic conductor is shorter than the mean free path of the electrons. In the case of equilibrium, when no voltage is applied through the junction, no current flows due to the symmetry of the device. The Fermi level of the left electrode is raised when a bias is applied to it, and an electron from an occupied state on the left electrode tunnels to an unoccupied state on the right metallic electrode, and during this procedure, the energy of the molecule is preserved. In coherent tunnelling, the current rises linearly with the applied slight bias.

1.4.2.2. Incoherent Tunnelling

Incoherent tunnelling is the case of electron tunnelling through a series of barriers, and the electron residence is long enough to experience phase change [52]. In this case, the barrier can be taken to have a vibrational mode with a frequency ν. The applied bias is strong enough to cause the electron lose an energy quantum of $h\nu$ to excite a vibrational mode of the barrier and tunnel into a different empty state. The process is then inelastic tunnelling, and the

applied bias voltage determines the overall tunnelling current. [53]. Qian, used a system to increase and record the light generation, which resulted from enhancing inelastic tunnelling. Inelastic electron tunnelling leads to a transformation of electrons to higher energy levels, leading to light generation on their way back to the lower states. However, emission efficiency from inelastic tunnelling is very low since most of the tunnelling happens coherently. Qian, used a set of nanocrystals assembled into metal-insulator-metal junctions to show efficient light generation resulting from enhanced inelastic tunnelling. The ability of the inelastic tunnelling to produce photons can be enhanced by making a plasmonic structure with a considerable local density of optical states. Single-crystalline silver nanocrystals have been used to make a tunnel junction with a gap distance of about 1.5 nm. A layer of polyvinylpyrrolidone was used to encapsulate two ordered silver single-crystal cuboids to make the junction [54]. The polymer works as an insulating barrier [55] and the length of the polymer used to encapsulate cuboid silver electrodes can control the gap distance of the tunnel junction. A powerful plasmonic field was generated by the plasmonic mode inside the nano tunnelling gap, which results in a massive boost of the emission efficiency by inelastic tunnelling [54].

1.4.2.3. Coulomb Blockade

A Coulomb blockade is characterised by the existence of a small charge island between two metallic electrodes. If the charge island is small enough and

contains N electrons, an energy gap exists between the energy of the final (Nth) electron and the energy of the first unoccupied electron state (N + 1) [56]. This gap is equal to:

$$E_c = \frac{e^2}{C_{dot}} \qquad \textbf{Equation 5}$$

Here, C_{dot} is the total capacitance and e is the elementary charge. As a result, if the the energy gap is greater than the thermal energy in the system (k_BT, where k_B is Boltzmann's constant and T is the temperature), quantum mechanical tunnelling of electrons will be impossible in this situation because the only free orbitals into which electrons can tunnel to the molecule are those with higher energies than the electrons in the electrodes (Figure 1.7a) [56]. Now assume that a gate is utilised to electrostatically modify the energy levels of the molecular orbitals in relation to the electrodes. In that situation, the N+1 unoccupied orbital may be shifted beneath the left electrode, giving electrons possibility to tunnel through the molecule one at a time. (Figure 1.7b) [56,57].

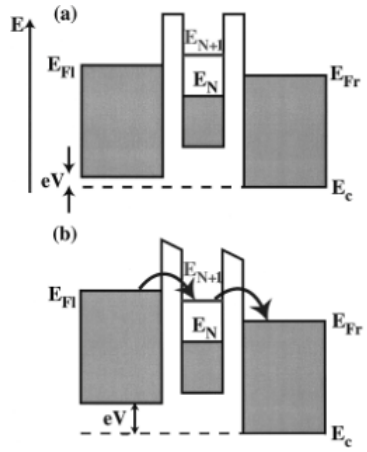

Figure 1.7. a) The energy gap between the last (Nth) electron energy and the first empty electron state (N + 1). b) Showing tunnelling of single electrons after pushing the empty state below Fermi energy of the left electrode. The Figure is used from reference [48] with the permission of the publisher (Elsevier Science Ltd).

Coulomb blockading can be observed for small metallic or semiconducting nanoparticles when the energy of charging exceeds the thermal energy (k_BT). Sometimes the redox charging of molecules such as phthalocyanines with a single metal ion core and an "organic shell" has been referred to as Coulomb blockading [58–61]. For such molecular junctions, this is strictly speaking better referred to as redox charging, with the electron (hole) going through the organometallic structure and residing on the single metal ion core. If the capacitance is small enough, Coulomb blockading leads to a relatively large charging energy that can exceed the thermal energy [58–60].

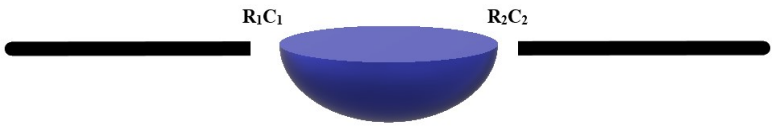

Figure 1.8. Tunnel junctions in series with tunnelling resistances and capacitances, shown as R_1, R_2, C_1 and C_2.

As a simple single-electron device, it is possible to consider a small quantum dot connected to the reservoir through a tunnelling junction [62]. Here, C_{dot} is the total capacitance ($C_{dot} = C_1 + C_2$), and e is the elementary charge. The system has two tunnel junctions in series with tunnelling resistances R_1 and R_2. For such a system, the total capacitance of the dot comprises two capacitances C_1 and C_2, which are related to each junction (Figure 1.8) [52]**.** By adjusting the bias voltage of the gate electrode, one electron can tunnel onto the dot. If the total capacitance is small, and E_C exceeds the thermal energy,

no electron can tunnel through the dot unless an external bias is applied to conquer the Coulomb blockade [52].

Lee, reported on the analysis of MoS_2 monolayer behaving as a single electron transistor with the use of low work function metal electrodes [63]. The single-electron tunnelling through a quantum dot showed Coulomb blockading at low temperature. Zinc was chosen since it has a small work function close to the electron affinity of bulk MoS_2; hence it leads to a minimal barrier at the metal-semiconductor junction. In the case of $k_BT << E_C$ (here E_C is the charging energy corresponding to a total capacitance of the MoS_2 single-electron transistor), the conductance versus back-gate voltage curve showed periodic conductance oscillations as a function of gate voltage and suppressed conductance regions separate the conductance peaks. These features are characteristic to single-electron charging related to the Coulomb blockade phenomena [63].

1.4.2.4. Hopping

The relative alignment between the energies of the Fermi levels of the metal contacts and those of the molecular orbitals of the bridge can play a crucial role in determining the charge transport mechanism for M-SAM-M junctions, where M = metal contact and SAM = self-assembled monolayer [35]. The highest occupied molecular orbital (HOMO) and lowest occupied molecular orbital (LUMO) play a vital role in conduction through SAMs sandwiched between metal contacts. This role can be viewed as being analogous the that

of conduction and valance bands in semiconductors. The energy difference between the LUMO and HOMO is usually several electron volts depending on the electronic structure of the molecular bridge [52]. The Fermi level of the metallic contact often sits around the centre of the HOMO-LUMO gap, and it may not coordinate with either HOMO or LUMO of the molecule [64]. This misalignment in the energy levels results in a contact barrier, and charge transport through the molecule relies on the height and thickness of the barrier [65–68]. If conduction is by hopping, then charge transport is thermally activated [38]. Hopping is generally the predominant charge transport mechanism in long molecular wires. The current density of the hopping conductance is given by [24]:

$$J \propto V exp\left(-\frac{\phi}{kT}\right) \qquad \textbf{Equation 6}$$

Where ϕ is the barrier height, V is the applied bias, and T is the temperature. Thus, electrons hop from one isolated state to another in the molecule in a thermally activated mechanism, depending on the temperature.

In single-molecule junctions, the transition from tunnelling to hopping was studied by Hines, using scanning tunnelling microscopy while they used the break junction technique to investigate the emergence of these long molecular wire junctions throughout the pulling process. Four conjugated molecular "wires" with different length values from 3.1 to 9.4 nm were used in the junction (molecule 1 was the shortest and 4 the longest). Conductance decreased upon moving from molecule **1** to molecule **2**, while the conductance showed no dependence on the temperature. By contrast, the

conductance of molecules **3** and **4** showed no length dependence, but their conductance was highly dependent on temperature. This trend is in line with conduction occurring by two various mechanisms in the molecular wires depending on their length: a coherent tunnelling mechanism in the shorter molecules and by an incoherent charge hopping process in the longer molecules. For the single conductance determinations at 40 ˚*C* the conductance value of molecule 1, with the length of 3.1 nm, was 9.8×10^{-6} G_0, while this value shows a large drop to 4.6×10^{-8} G_0 for molecule 4, which is 9.4 nm long. G_0 is the quantum conductance given by $2e^2/h$, where e is the electron charge, and h is Planck's constant. [24]. Similar deductions were made for SAM molecular junctions in an earlier study by Choi, [69]. In this case, the conducting AFM technique was used to form Au-SAM-Au junctions by pressing the gold-coated c-AFM tip on the top of a SAM. SAMs of conjugated oligophenyleneimine (OPI) wires were formed, ranging in length from 1.5 to 7.3 nm. Analysis of I-V data and temperature dependence showed a change in transport mechanism from tunnelling to hopping at around 4 nm for this series of OPI SAMs. These and other studies, at both the single-molecule and large area junction level, supports the notion of tunnelling charge transport mechanisms in shorter molecules and thermally activated hopping in the longer ones [69].

1.4.2.5. Fowler-Nordheim Tunnelling

When electrons injected from a metal pass through a barrier under an applied voltage, a form of electron tunnelling known as Fowler Nordheim (FN) tunnelling can occur [70]. In FN tunnelling, current J can be calculated quantitatively using equation 7. FN tunnelling is a charge transport mechanism that, like coherent tunnelling, is independent of the temperature and shows a strong dependence of the tunnelling current on film thickness and the applied bias voltage [67]:

$$J \propto V^2 \, exp\left(-\frac{4s\sqrt{2m}\phi^{\frac{3}{2}}}{3ehV}\right) \qquad \textbf{Equation 7}$$

Here, e is the electron charge, s is the tunnelling distance, m is the effective mass of the electron, h is Planck's constant, and ϕ is the tunnelling barrier height. FN tunnelling occurs when the applied voltage surpasses the barrier height; hence, the charge transport mechanism switches from quantum tunnelling (which takes place at low-bias voltages) to field emission or FN tunnelling (at the high-bias regime). The transition voltage is an experimental estimate of the energy gap at the transmission point between the Fermi level and the LUMO orbital (the barrier height, ϕ) [52]. Field emission is defined as the process of electrons escaping from a material's surface in the presence of a sufficiently large electric field [71]. When a highly positively charged metal is placed near a substance, the positive charges within the conductor draw the free electrons out of the material. The restrictive forces will be overcome if

the positive potential on the conductor is strong enough, and free electrons will be released from the material's surface [72].

FN tunnelling is unmistakably quantum-mechanical, with no classical analogue. As a result of the applied voltage, the rectangular barrier alters to a trapezoidal shape, enabling electrons to tunnel more easily [43], [38,52]. If the applied bias voltage exceeds the barrier height, the barrier shape changes again from trapezoidal (Figure 1.5) (direct tunnelling) to a triangular (FN tunnelling) form (Figure 1.6) [38], and the transport mechanism shifts from quantum mechanical tunnelling at low bias voltage to field emission at high bias voltage values [52].

Noghuchi and colleagues studied the *I-V* characteristics of a Co(II) complex of a tetraphenylporphyrin derivative [73]. Based on their *I-V* measurements, they calculated a barrier height of 0.5 eV. They observed the shift from direct to FN tunnelling by measuring the molecule in the bias range of ∓ 1. They display their data in a FN plot $\left(ln\frac{I}{V^2} \propto \frac{1}{V}\right)$, and their results demonstrate a slope change around applied bias values greater than 0.3 V, when FN tunnelling becomes dominant. However, for bias levels smaller than 0.3 V, a logarithmic of current dependence is seen, indicating that direct tunnelling is occurring in the junction (Figure 1.9) [73].

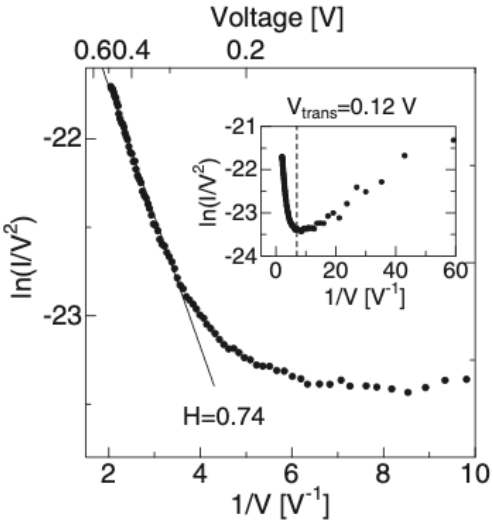

Figure 1.9. An example of a Fowler–Nordheim plot. The FN plot with enlarged scales is shown in the inset. The direct tunnelling to FN tunnelling transition voltage (V_{trans}) is 0.12V. The plot is taken from reference [73] with the permission of the publisher. (Copyright (2007) The Japan Society of Applied Physics).

Wang and colleagues investigated the electrical conduction mechanism of an alkanethiol self-assembled monolayer. They selected this system because it is well-characterised and has an excellent metal-molecule-metal connection. A tunnel junction was formed between the metallic electrodes due to the large HOMO-LUMO gap of about 8 eV in the molecule [66]. The thiolate group's bonding to the gold surface is robust, with a bonding energy of 1.7 eV [68]. The molecule was already examined using STM and AFM by other groups in the past, and it was claimed direct tunnelling was the primary charge transport mechanism [68]. However, Wang, found those studies insufficient in determining the transport mechanism because they were all done at ambient temperature. Hence, they measured *I-V* characteristics in a sufficiently broad temperature range to identify the charge transport mechanism of the self-assembled alkanethiol molecular systems [67]. Over the temperature range of

300 to 80 K, they observed no substantial temperature dependence of the SAM (from V = 0 to 1 V), and as a result, they concluded that the alkanethiol conduction mechanism is direct tunnelling in that range of bias voltage. Tunnelling in a junction can be classified as either direct ($V < \phi/e$) or Fowler-Nordheim ($V > \phi$ /e), depending on the bias applied in comparison to the barrier height (ϕ). Because of their unique voltage dependency, these two tunnelling procedures could be differentiated experimentally [74]. Wang, showed the FN plot exhibits no significant voltage dependency, confirming no apparent FN tunnelling in the bias range of 0 to 1 eV, which means the barrier height is greater than the applied bias. They showed electrons tunnelled through a trapezoidal barrier by direct tunnelling when the applied voltage was less than the barrier height ($\phi/e < 1.39$ eV) [67], [69]. When the applied voltage was more than 1.39 eV, electrons tunnelled through a triangular barrier by Fowler–Nordheim tunnelling [74], [69].

1.5. STM Based Single-Molecule Conductance Techniques

The invention of scanning tunnelling microscope and techniques based on this instrument initiated a new era in measuring and understanding electron flow through single molecules. In 2000, a review paper by Aviram, described molecular structures that might be suited as molecular rectifiers, switches, and storage. Later in the early 2000s, a sequence of papers elucidated measurements on such molecular devices might be performed in a defined

way and even down to the level of single molecules, and this has subsequently led to a better understanding of charge transport characteristics of molecules.

1.5.1. STM-Break Junction Technique

In 2003 Xu and Tao developed the *in-situ* break-junction technique as a new method for repeatability forming and breaking single-molecule junctions using an STM [75]. The break-junction technique is now the most common method for measuring the conductance of single molecules [52]. Xu and Tao used a gold STM tip as one electrode and a gold substrate as the other electrode for forming molecular junctions. During the break-junction cycle, a fixed bias voltage is set between the metallic tip and the substrate. The tip is forced to engage into direct metallic contact with the substrate, either covered with pre-adsorbed sample molecules or with the target molecules dissolved in solution. The tip is engaged with the surface using the piezoelectric control to achieve a pre-set upper current limit. The current limit is chosen to correspond to the formation of metal-metal contact (typically >> G_0). As the tip is retracted, the metal filament between tip and substrate narrows to the point where there are a defined number of gold atomic filaments (channels) connecting between the two leads. After this point, steps are seen in the conductance of the junction versus retraction trace as single metal atomic contacts sequentially break at the gold neck between the tip and substrate. These conductance steps correspond to integers of conductance of single metal atomic contacts. Each “quantised” step can be predicted for metal

junctions such as gold, with ideal single channels, to show conductance of $N \times G_0$ (where is $G_0 = 2e^2/h$ and N is an integer, h is Planck's constant, and e is the electron charge) [76].

As the STM tip continues to withdraw from the substrate at a given rate, the gold-gold neck thins to a single gold atom wide filament, which then itself breaks. This then opens a nanogap between the tip and the substrate followed by the relaxation of the gold contact atoms. This very rapid relaxation is called "snap back" and gives rise to the snapback calibration distance used to estimate junction stretching length. For Au-Au junctions in typical STM-BJ experiments, this snapback adjustment has been estimated to be around 0.5-0.6 nm [77]. Depending on the molecular size, this initial size may be large enough to host a target molecule in-between significantly if it is tilted, but in any case, the tip continues to retract, and the gap opens up further. Stepwise features may then be seen in the conductance versus retraction distance traces, and these conductance steps with values smaller than the G_0 may be related to an integer number of molecules trapped in the junctions (Figure 1.10b). Finally, the molecular junction breaks following further tip withdrawal, and the break-junction cycle ends (Figure 1,10c).

Due to the stochastic nature of the junction making and breaking process, there is expected to be variability in the traces and steps corresponding to junction breaking. For this reason, it is imperative to repeat the process of engaging and retracting the tip thousands of times to collect a considerable number of traces. Statistical analysis in 1D conductance and 2D conductance-distance histograms is then used to affirm the most probable conductance and

junction break-off values. This statistical method gives reliable, most probable conductance values for a wide range of molecular targets. In addition, recent advances have been made in data collection and analysis with unsupervised classification algorithms, which are able to sort data into different classes (e.g. different conductance values or junction stretching characteristics) sometimes with no prior assumptions [78–80]. Machine learning is also being applied to such recognition and sorting of single-molecule data [81–85].

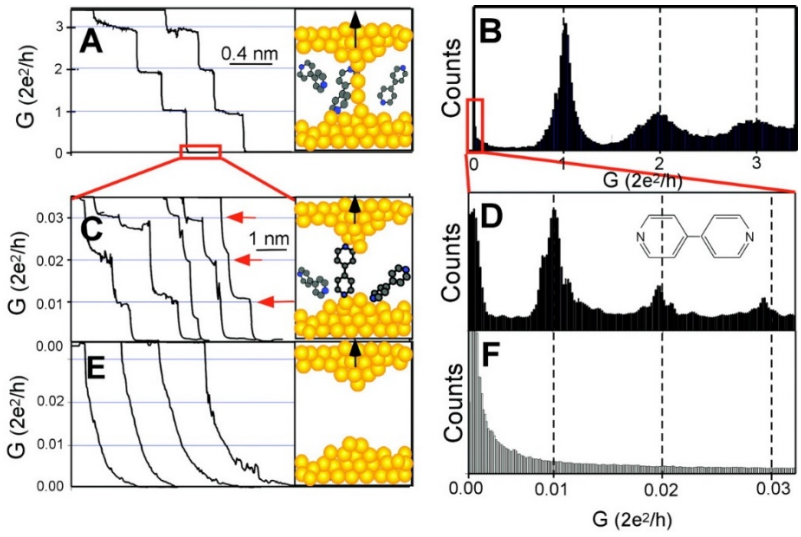

Figure 1.10. As the tip is moved away from the substrate, the conductance of a gold contact established between a gold STM tip and a substrate drops in quantum steps approaching multiples of G_0 (= $2e^2/h$). (**B**) In (A), a conductance histogram generated from 1000 conductance curves reveals explicit peaks near 1 G_0, 2 G_0, and 3 G_0 because of conductance quantisation. (**C**) If molecules like 4,4′ bipyridine are available in the solution, a new sequence of conductance steps arise after the contact is shown in (A) is entirely broken, related to the breakdown of the final quantum step. The stable molecular junction here between tip and substrate electrodes is responsible for these stages. (**D**) As shown in (C), a conductance histogram generated from 1000 measurements indicates peaks around 1 ×, 2 ×, and 3 × 0.01 G_0 attributed to one, two, and three molecules, respectively. (**E** and **F**) There are no such steps or peaks in the same conductance region when molecules are absent. Used with permission from reference 70. Copyright (2003) by the American Association for the Advancement of Science.

1.5.2. Current-Time Technique

Nichols and Haiss used the STM to establish a fixed-gap junction between the tip and the substrate. In this technique, the distance of the junction can be altered by changing the set-point currents. Formation and deformation of the single-molecule junction cause fluctuations in the current [43]. The amplitude of the current pulse can be used to obtain the conductance of the single-molecule. The current-time or $I(t)$ technique is an attractive alternative method when direct contact or crashing of the electrodes with each other is not favourable. This is the case, for example, when the tip and substrate are different materials such as GaAs substrates and gold tips [86]. A primary requirement when using this technique to determine a single molecule is finding an optimal gap distance that corresponds with the length of the target molecule or somewhat shorter. In this respect, the separation of the metallic tip from the substrate should be shorter than the length of the fully stretched molecule [52].

1.5.3. Current-Voltage Technique

It is possible to collect large numbers of I-V scans during molecular junction formation as the tip is retracted and the junction stretched. The retraction may be done in a stepwise manner to yield $I(V;z)$ data. This method has now been applied to a great deal of molecular junction systems, and good examples included the study by Pires, of alkanedithiol molecular conductance under

ultra-high vacuum [87] and the study of the bias dependent conductance of porphyrin tapes by Leary, [88]. The *I-V* curves will be very sensitive to the electronic structure of the molecular bridge, including both the molecule electronic structure, the contacts and the coupling between the molecule and leads. Analysis of I-V curves can help determine the relative energy gap between the Fermi level of the metallic electrode and the molecular conduction orbital in a junction and the coupling, using suitable models such as the single-channel transport model described below.

On the other hand, *I-V* measurements do not directly inform whether the charge is transported predominantly by either the HOMO or LUMO of the molecular junction [89]. Here thermopower measurements can help in determining the weather transport is HOMO or LUMO mediated. The *I-V* behaviour of a single molecule can also help in determining any rectifying or negative differential resistance behaviour [90].

Two models for the analysis of the *I-V* curves are the single-channel transport model and the Simmons model. Both models use assumptions and have limitations. The Simmons model has been used rather widely to analyse the *I-V* measurements, but its applicability for the molecular junctions may not be so justified as for thin insulating oxide films [91]. In the presence of highly insulating oxide tunnel junctions, the approximation of the energy barrier similar in height to the offset between the Fermi level and the oxide valence band works well for a square barrier. Through a tunnel junction consisting of molecules, however, there is a rather sizeable electronic coupling. Consequently, using the three-parameter Simmons equation (*A (*junction

area), *s* (width of the barrier) and ϕ (barrier height)) parameters for molecular junction data becomes challenging due to the possibility of physically unreal values for the fit parameters. For example, it is not easy for the Simmons model to make a correct relationship between the *A* (junction area), *s* (width of the barrier) and ϕ (barrier height) parameters, which means the value of *s* would increase with molecular length, but the model comes with a dramatic increase in *A* and a slight raise in ϕ. In molecular junctions, there is a comparably robust electronic coupling between molecules and metals. As a consequence, it is challenging to relate molecular junction data to the Simmons model.

The single-channel transport model describes the transmission through a single-molecule junction. In theory, electron transport can occur in many molecular orbitals at the same time. However, in many cases, HOMO or LUMO is closest to the metal's Fermi level and dominates transport in a particular voltage range. The single-channel transport model can be used to explain such a circumstance [92]. The molecular orbital is measured with regards to the electrodes' Fermi energy, which is set to zero [92]. The voltage supplied across the junction determines this location at finite bias. The scattering rates $\Gamma_{R,L}$, which characterise the coupling strength to the metal electrodes, are also essential elements in this model. The I-V characteristics of this model can be determined using the Landauer approach where, the transmission probability is crucial. This model reasonably explains the exponential decrease of the low-bias conductance as a function of the distance between the electrodes in all types of tunnel barriers since the transmission

controls the conductance [92]. This model can be considered for a single-molecule if the coupling of the metal-molecule is considerable enough and direct tunnelling is the charge transport mechanism [89,91].

1.6. Structure-Property Relationship of Single-Molecule Junctions

The relationship between the structure and properties of the single-molecule junctions can be devolved into two parts: the anchoring group and the electrode material [93].

1.6.1. Anchor Group

The anchoring groups link the electrodes to the molecular wire, and the chemical attachment can be through either covalent or non-covalent bonds. To make a molecular bridge, anchor groups are required at each end of the molecule. The nature of the interaction between the anchoring group and the metallic electrode, in addition to the type of the anchor groups, have essential influence in the conductance of a molecule [93,94]. A wide range of anchoring groups have been used to link molecules to the metallic electrodes, such as thiol (R-SH), sulphide (R-S-R), disulphide (R-S-S-R), thiocyanate (R-SCN), alcohols (R-OH), amines ($R-NH_2$), alkene ($R-CH=CH_2$), phosphide ($R-PR_2$) and selenide (R-Se-R) [95]. Dative interactions or covalent bonding are generally most suited for effectively binding the anchor groups to the metallic

electrodes. Gold is by far the most commonly used metallic electrode in single molecule electronics, and the molecular bridge can be formed with electron donation to a Lewis acidic gold atom from a lone pair or a donor. Some of the predominantly used anchor groups to gold may be classed as σ-donors, such as amines and thiomethyl. Such dative contacts are considered as well suited since they minimise the conductance distribution and limit the Au-linkers contact geometry distributions by binding with undercoordinated gold adatoms on the electrodes [94]. π donors have also been deployed as anchoring groups, including fullerenes and π-conjugated hydrocarbons [96].

Because of the variability in the electrode-anchor group geometry, discrepancies may arise between measurements, which may be influenced by the method for junction formation or other different experimental conditions. To ameliorate variability from one junction formation to the next and to achieve a statistical view of the most probable conductance value of the molecular target, thousands of measurement traces are collected to form the conductance histograms as previously explained. As discussed in Section 1.3, the conductance is dominated by the molecular orbital closest in the energy to the Fermi level of the electrode. So, the conductance is highly dependent on the energy difference (ΔE) between the Fermi level and the conducting orbital and the electrode-molecule's coupling strength Γ [93]. Computations, such as first principle DFT transport calculations, can also be helpful as a guide the nature of the carriers and the conducting orbital.

1.6.2. Electrode Material

Gold has often been the contacting metal of choice for achieving reproducible and consistent determinations of molecular conductance by the break-junction technique. Other metals have also been successfully used, such as silver, platinum, cobalt, and nickel [97–99]. Some of these metals oxidise in air, and this has been overcome in the case of nickel by using careful electrochemical control [100].Single-molecule conductance determination has also been achieved with semiconductor contacts [101] and graphene [102]. In the future, measurements under UHV conditions may also be used to overcome surface oxidation issues.

One of the critical features that affect the conductance of the single-molecule junctions is the density of the state of the metal at the Fermi level [93]. For example, alkanes terminated with isothiocyanate were measured separately using Pd and Pt electrodes [103]. The measurements showed higher conductance of the junction when Pd electrodes were used. Palladium d- band provided better coupling with the anchor group π orbitals close to the Fermi level. Therefore, a better d character of Pd compared to Pt and Au offers improved d-π interaction of the metal-molecule [104].

1.7. Thesis Outline

Investigating how molecular structure influences electron transport through molecules remains an essentially academic pursuit, with relevance to many

diverse scientific areas, including electrochemistry, molecular photovoltaics, molecular and organic electronics, and electron transport in biology, including redox-active metalloenzymes and photosynthetic and respiratory pathways. Although this has been a very active area of science in recent years, there are still broad aspects under investigation, including the influence of the environment, charge transport mechanisms, charge transport in supramolecular systems, quantum interference and the influence of molecular structure on the molecular conductance. There are technological avenues that might be addressed as well, including molecular thermoelectrics, the integration of molecules within devices and how the coupling of light within molecular electrical devices might be deployed. The research presented in this thesis uses modern and state-of-the-art methods to measure single-molecule conductance, such as break-junction methods, current-voltage determination, and flicker noise analysis methods. Such measurements have been made at ambient temperatures in different environments, including organic solvents and air. In Chapter 3, the impact of quantum interference on the molecular conductance of a series of pyrrolodipyridines is presented. As an aromatic hydrocarbon composed of two benzene rings fused on either side of a five-membered ring, pyrrolodipyridine has a strong aromatic system with a bridge nitrogen atom in the centre of the five-membered ring. The molecule shows fascinating delocalisation of electrons. A variety of pyrrolodipyridines (carbazole-like) molecular wires were investigated and modified. Chemically modulating the bridging nitrogen atom in the tricyclic ring structure allows to adjust the electrical conductivity and quantum interference patterns. This

Chapter shows how a phenyl ring can behave as an insulator or conductor depending on the substitution pattern around the ring. In the case of the substituent being on the para or ortho position of the ring, high conductance is obtained, while the ring with meta-connected substituent shows lower conductance because of the destructive quantum interference. Chapter 4 presents an approach to minimise the influence of intermolecular phenomena in the molecular junctions by encapsulating the molecular targets with a small molecular cage. The encapsulation of the molecular wire within the host cage impedes the formation of multi-molecular junctions.

Pillar[5]arene rings are deployed here as the cage with different lead molecules in order to investigate the effectiveness of the host molecules in reducing intermolecular interactions in the junction. Pillararenes are excellent hosts for molecules with electron-donating groups, and they are well suited to study host-guest chemistry at the single entity level. Chapter 5 presents a study of verdazyl radicals within gold break junctions. They are stable radicals even within ambient environments, and they maintain their radical character as molecular wire in the junction between gold electrodes. They show higher conductance than their closed-shell tetrazine counterparts. Other research groups have attempted to form stable radical single-molecule junctions at room temperature, but these studies resulted in the loss of open-shell character [105]. By contrast, the single-molecule junction conductance of verdazyl radicals was successfully measured. The radical molecule was electrochemically reduced while the molecular conductance was measured using the in-situ STM break-junction technique.

CHAPTER 2

MATERIALS AND METHODS

2.1. Introduction

In this Chapter the materials and chemicals which were used for experiments and sample preparation will be discussed. Following that, experimental methods and data collecting are outlined. The final part of this Chapter summarises the contributions made by colleagues and collaborators to the projects.

2.2. Sample Preparation

Hydrochloric acid, hydrogen peroxide, sulfuric acid, mesitylene, and tetrahydrofuran (THF) were purchased from commercial sources. For the break-junction studies in Chapter 3 and 5 as well as single-molecule-I-V and flicker-noise measurements in Chapter 5, 1 mM solution of the compounds were prepared in mesitylene if they were soluble enough. Some of compounds in Chapter 3 had low solubility in mesitylene so a mixture of mesitylene and THF (4:1) was used. In Chapter 4, self-assembled monolayers were made form in acetone solutions (dry, analytical-grade acetone from Fisher Scientific was used). This was done by immersing substrates in a 1 x 10^{-4} M solutions containing the complex and leaving them at 20 °C for 24 hours.

In Chapter 5, electrochemically controlled STM-BJ experiments were performed in 1 mM solutions of the target molecular wire in the ionic liquid 1-butyl-3-methylimidazolium triflate (Merck), that was previously dehydrated by heating for >16 hours at 120 °C in vacuo (~8 mbar) in the

presence of 20% w/w 4 Å molecular sieves (Merck). Since just heating the ionic liquid under a vacuum may not be sufficient, molecular sieves were used to boost the efficiency of dehydration (water removal). Molecular sieves also help to keep the ionic liquid solution dry for a few days following the dehydration procedure.

For all scanning tunnelling microscopy (STM) experiments, liquid sample cells made of polytetrafluoroethylene (Teflon) or polychlorotrifluoroethylene (PCTFE) were utilised. The cells were properly cleaned prior to each experiment by sonicating them in three different cleaning solutions for 15 minutes each: first in piranha solution (in a 1:3 ratio, 30 w/w hydrogen peroxide was added to concentrated sulfuric acid to make piranha solution - note, handle piranha solution with great care), then in Milli-Q water, and finally in acetone.

STM gold tips (99.99 % pure gold wire, 0.25 mm in diameter, bought from Goodfellow Cambridge Ltd,), were cut with cleaned scissors and used in all conductance studies. The tips were electrochemically etched for measurements in polar solvents like ionic liquid in Chapter 5, so gold wire is placed in a 1:1 combination of hydrochloric acid and ethanol solution for etching [106] then for electrochemical STM experiments, the tip was coated with insulating wax (Apiezon W40). A coiled platinum wire (Goodfellow 99.99+%) was used as counter electrode and an electrochemically chloridised Ag wire (Goodfellow 99.999+%) was used as reference electrode [107].

All experiments were performed with Au tips and Au-on-mica (Advent Research Materials Au 99.99+% evaporated on freshly cleaved Agar Scientific muscovite mica using a Korvus Technology Tau e-beam evaporator) or Au-on-glass (Arrandee Metl GmbH) substrates.

For UV-Vis measurements, pyrrolodipyridines compounds were dissolved in dry acetonitrile (Sigma-Aldrich spectrophotometric grade), and measurements were done in 1 cm quartz cells.

Cyclic voltammetric measurements of the compounds in Chapter 5 were performed for 1 mM of target molecules dissolved in CH_2Cl_2 with tetrabutylammonium hexafluorophosphate as supporting electrolyte (Sigma-Aldrich) and 20 mM of the target molecule (verdazyl) in ionic liquid (1-butyl-3-methylimidazolium triflate) (Merck).

For NMR characterisation of the compounds in Chapter 3, 4 and 5 DMSO-d6 and D_2O were used to prepare the solutions for the analysis.

2.3. Experimental Setup

The fabrication and characterisation of single-molecule connections were carried out using a modified Keysight 5500 scanning tunnelling microscope. It uses a custom 4-channel current amplifier based on the design by Meszaros, [108] STM-BJ and electrochemical control-STM-BJ experiments were carried out. When it came to controlling the tip position and substrate bias, the Keysight N9610A electronics did the task, while the electrochemical potentials were applied by a bipotentiostat that was built into the STM

controller. A National Instruments NI9215 USB DAQ with custom Python software are used to record the 4-channel output of the preamplifier at a rate of 10 kSa/s. The STM was equipped with a Femto DLPCA-200 single-channel preamplifier with a wide bandwidth for single-molecule *I-V* measurements. A dual-channel Keysight 33522B Arbitrary Waveform Generator (AWG) applies a bias to the substrate and controls the position of the tip, by applying a voltage ramp to the STM piezoelectric transducer via a Keysight N9447A breakout box. Substrate bias, position of the tip and current amplifier output are obtained at the same time at 20 kSa/s with a National Instruments PXI system (24-bit PXI-4464 DAQ, PXIe-1062Q chassis, PXIe-PCIe8381 interface). A 10 kΩ resistor between the AWG and the substrate presents overload of the preamp when in contact during the high-voltage ramps.

UV-Vis data was acquired on a Perkin Elmer λ25 spectrometer, in the region 190-500 nm.

Cyclic voltammetry measurements were conducted in a standard three-electrode cell, with Pt disc working electrode, Pt wire counter and Pt wire pseudo-reference electrodes for the measurements in CH_2Cl_2 and with a Au disk working electrode, Pt wire counter and Pt wire pseudo-reference electrodes for the measurements in ionic liquid with data collected from an EmStat3+ potentiostat. The ferrocene/ ferrocenium ($E_{1/2}$ = 0 V) and decamethyl ferrocene/ decamethyl ferrocenium couples ($E_{1/2}$ = –0.55 V versus ferrocene / ferrocenium) were used as internal references for potential measurements.

NMR characterizations were performed in Bruker AV-500 for the molecules in Chapter 3, 4 and 5. The NMR characterisations of molecules in Chapters 3, 4 and 5 were done by Dr Vezzoli at the University of Liverpool, collaborators at the University of Zaragoza and the University of Western Australia, respectively.

2.4. Data Acquisition

In the break-junction technique the formation of junctions is accomplished by repeatedly forcing Au tip into a gold substrate and then withdrawing it in a solution of the target molecular wire at a constant speed of 20 nm/s. Throughout the process, the current is measured at a constant tip-substrate bias of 200 mV. When the point contact is disrupted, end groups of the molecular target bind with undercoordinated Au atoms to produce Au-molecule-Au junctions in the nanogap, which are subsequently stretched until they break. The conductance is calculated as $G = I/V$ in units of the quantum function of conductance ($G_0 = \frac{2e^2}{h} \cong 77.48\ \mu S$). Thousands of conductance versus electrode separation traces are collected and combined into the conductance histograms for each indentation-withdrawal cycle. A typical break-junction trace displays a succession of plateaux at various integers of G_0 caused by charge transport via one or a few Au atoms, as well as molecule-dependent plateaux at considerably lower conductance values than the G_0. During an STM-BJ experiment, the traces are aligned to the rupture of the metallic nano-contact. These are then used to create 2D conductance versus

electrode separation density plots, which illustrate the conductance development as the two electrodes are dragged apart. A Python script was used to transform raw STM-BJ data into conductance-distance traces. The approach data was eliminated, and only data from the withdrawal part of the experiment was used for analysis. For each molecule, thousands of traces were recorded and plotted as logarithmically binned conductance histograms without data selection. A detailed example of a break-junction experiments was described in Section 1.4.1.

The tip is engaged with the surface using the piezoelectric control to achieve a pre-set upper current limit (Figure 2.1 a). As the tip is retracted, the metal filament between tip and substrate narrows to the point where there are a defined number of gold atomic filaments (channels) connecting between the two leads (Figure 2.1 b) [76]. As the STM tip continues to withdraw from the substrate at a given rate, the gold-gold neck thins to a single gold atom wide filament (Figure 2.1 c), which then itself breaks (Figure 2.1 d). This then opens a nanogap between the tip and the substrate followed by the relaxation of the gold contact atoms (Figure 2.1 e).

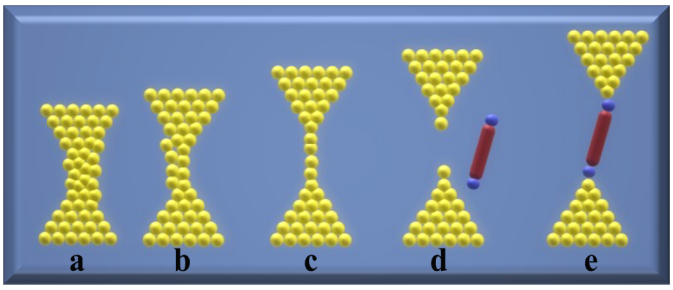

Figure 2.1. Schematic illustration of single-molecule break junction technique. **a**) Au tip is engaged with Au substrate, and the upper limit current is achieved, and **b**) tip starts to retract. **c**) Upon further retraction, a single Au-Au channel remains between the tip and the substrate. **d**) Nanogap opens after more retraction, but the gap is too small to form a junction. **e**) Gap is wide enough for the target molecule to attach to the uncoordinated gold atoms and form a molecular junction.

For the *I-V* technique a modified STM-BJ method is employed. The tip is pushed into the substrate, then withdrawn in steps related to the length of the molecule of interest (the length of the molecule was used in Chapter 5 was 1.1 nm). In stage one, the tip-substrate bias is kept at a stable value (200 mV) for 25 mS, then in stage two, the voltage is ramped from +2 to -2 V for 50 mS to acquire the *I-V* characteristics, and in stage three, the bias is held stable at 200 mV for another 25 mS. To analyse the data, the software selects 50 data points from the beginning of stage one and 50 data points from the end of stage three and calculates the average for each group. The software keeps the data if the data range is between 10^{-2} G_0 to 10^{-6} G_0, this is to avoid any noisy data close to the noise level of the instrument and any gas molecules (molecules in the gap not properly connected) that show up just after the $1G_0$. All these traces are accumulated and shown in the final plot of the logarithm of current against voltage.

Flicker noise measurements were used to distinguish through-bond from through space tunnelling in the molecules in Chapter 4. Flicker noise measures the noise in the break-junction technique. At ambient temperature, the primary source of noise in the break-junction technique is due to the motion of the metallic atoms, which results in variations in the molecules and electrodes coupling, and Flicker noise is capable of separating the noise related to through-space coupling from the through-bond coupling. This technique expresses the number of available conductance channels and their transmission [109].

In the flicker-noise (noise-power) technique, which analyses the current signal of molecular junctions in the frequency domain, the noise power is calculated by integrating the power spectral density between 100 Hz and 1 kHz. The noise power examines the power-law dependence on conductance ($NP \propto G^n$). The scaling exponent n is near to 1 when charge transport is entirely through-bond and this rises towards 2 when charge transport includes a through space contribution. Using terphenyl molecular wires as an example, it was found that the scaling component associated with the single-molecule junction was 1.16, rising to 1.78 for the stacked dimeric junction [109]. A "pull and hold" STM-BJ experiment, in which the tip is withdrawn in a step-like manner, and its position relative to the substrate is maintained constant for 100 milliseconds between each step was carried out. The junction current is measured at high speed (100000 Sa / s), sliced between steps, and sent for data selection using an automated algorithm to calculate average conductance and perform Fourier transform (FFT) analysis. The power spectral density is

calculated using the FFT algorithm throughout the whole frequency spectrum. The noise power in this region was plotted against G_{AVG} (average of the conductance of the slice of interest) to produce the plots which were obtained via numerical integration between 100 Hz and 1 kHz. The 1 kHz and 100 Hz cut-offs were selected because they have been shown to be effective in minimising the contributions to noise power coming from thermal noise (> 1 kHz) and mechanical vibrations (100 Hz).

To determine the energy gap between HOMO and LUMO experimentally, a UV-Vis spectrometer was used in the region of 190-500 nm. The maximum wavelength, the peak related to the strongest photon absorption, was used to calculate the energy gap between resonance and anti-resonance orbitals in the molecules in Chapter 3.

2.5. Contributions

The study in Chapter 3 was in collaboration with Lancaster University where Dr Mohsen Al-Khaykanee performed the theoretical calculations, and at the University of Liverpool, Dr Andrea Vezzoli undertook the synthesis of the molecules in this Chapter. In Chapter 4, molecules were synthesised and characterised by the group of Professor Santiago Martin (Lucia Herrer, Ivan Martin, Jose M Bonastre, Jose Luis Serrano, and Pilar Cea) at the University of Zaragoza. The work in Chapter 5 was in collaboration with the University of Western Australia and the University of Warwick. The molecules were synthesised and characterised by the group of Professor Paul Low (Varshini

J Kumar, Jian-Zhong Wu, Martyna M Judd, Elodie Rousset, Marcus Korb, Stephen A Moggach, Nicholas Cox) at the University of Western Australia and the calculations were done at the University of Warwick by Dr Sara Sangtarash and Dr Hatef Sadeghi.

CHAPTER 3

N-SUBSTITUTED PYRROLODIPYRIDINES

3.1. Background and Scope

Electron transport through a molecular junction is defined by an energy-dependent transmission function. The transmission function takes account electrons tunnelling across molecular orbitals (MOs) with various phases, resulting in quantum interference (QI) phenomena [110]. When a single molecule attached to two metallic electrodes, the charge transport can be represented by a Landauer-Buttiker zero bias transmission model [111]:

$$G = G_0 T(E_F) \qquad \textbf{Equation 1}$$

Where G_0 denotes the quantum of conductance and $T(E_F)$ indicates the transmission coefficient at the Fermi level. Transmission function is a function of the entire system, including the molecule, the leads and the lead-molecule contact. If the metallic electrodes make a poor contact with the molecule, $T(E)$ vs E will express the isolated molecule's energy-level structure [110]. When an electron passes from one gold electrode to the next, it can maintain phase coherence and avoid inelastic scattering. There is evidence that this is a realistic assumption for short molecules [112]. However, when the molecular length increases, the likelihood of inelastic scattering (from phonons or other electrons) increases [113].

On the nanoscale, charge transport is controlled by quantum effects and hence the phase of the tunnelling electrons is important [114]. An electron can tunnel through various MOs when it enters a molecular junction [114]. When an

electron wave travels across several conduction routes (molecular orbitals), phase differences can occur, resulting in quantum interference (QI). This effect can either raise (constructive QI) or decrease (destructive QI) the chance of electron tunnelling.

In the case of an isolated molecule, the system can be considered as "closed", and it consists of molecular orbitals and discrete energy levels derived by solving the Schrodinger equation [110]. If the molecule is coupled to the electrodes the system is open, and electrons entering a molecule continuously flow between the two contacts under bias voltage. In this situation, figuring out the transmission coefficient *T(E)* of the molecule, which indicates how electronic waves of energy E enter the molecules through metallic electrodes will be the main focus [110].

A Greens function can be used as a technical means for representing the pattern of interference. Greens function enables for visual analysis of the actions related to a source of force or to a charge concentrated at a point. As a basic example, consider a vocalist at the entry to an auditorium who sings a note with a constant frequency. If the note is maintained for long enough, the auditorium will experience a standing wave with a complicated pattern of nodes and antinodes. The magnitude of the standing wave at location *j* corresponds to the Greens function *G(j,i)* when the vocalist is at position *i*. If a window at location *j* is opened and its location corresponds with an antinode of the standing wave *G(j,i)*, the window will emit a loud sound [110]. This is a case of constructive interference in action. If the window is positioned near a node, however, no sound will escape, then It is believed that destructive

interference happens. The auditorium and the sound wave are analogous to a molecule and an electron wave in this analogy, and *i* and *j* designate atomic orbitals at certain places within a single molecule in a model based on atomic orbitals. *G(j,i)* is the amplitude of a wave at *j* because of a source at *i*.

It is important to find new methods to regulate quantum interference, since this could lead to useful functional molecular devices like thermoelectric convertors [115] insulators [116]. Introducing methods to control the quantum interference will open a new door for controlling the charge transport at the molecular level.

In linear conjugated or para-oriented systems, constructive interference can arise, whereas in cross-conjugated or meta oriented molecules, destructive interference can be found [117]. Aradhya conducted an experiment on a stilbene compounds that included a higher-conductance para-terminated 4,4-di-(methylthio)stilbene, and a lower-conductance meta terminated 3,3'-di(methylthio)stilbene [110]. At the Fermi level, the para molecule yields constructive interference, while meta leads destructive interference (Figure 3.1) [117]. The examples above shows how QI between several pathways can cause resonances (constructive QI) or anti-resonances (destructive QI) in the charge transport transmission curve. If this happens close to the electrode Fermi energy, conductance of the molecule can be particularly sensitive to adjustments in the environment, such as different in the surrounding atmosphere, temperature, gate voltage, or molecular conformation or electrode spacing [110].

The energies of molecular orbitals such as the HOMO and LUMO can be gained by solving the Schrodinger equation using DFT calculations. Changing the bias voltage adjusts the relative alignment of the molecular orbitals to Fermi level of the electrode, giving the opportunity of determination of energy dependence of the transmission [117]. The impact of the inter-orbital coupling between the HOMO and LUMO on the QI is influenced by this change in the energy level relative to the Fermi energies of the contacts.

Meta molecules (a molecule with substituents at the 1 and 3 positions of an aromatic ring) show an anti-resonance in the transmission function which is situated within the HOMO-LUMO gap, showing meta molecules have high energy dependence. However, there is no anti-resonance for para molecules (a molecule with substituents at the 1 and 4 positions of an aromatic ring) and hence less energy dependency is predicted for them (Figure 3.3) [117].

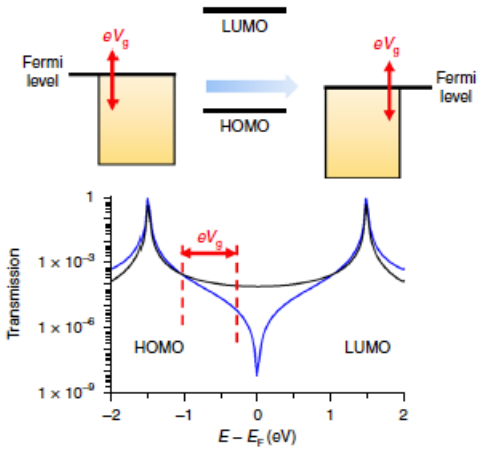

Figure 3.1. Top: changing the gate voltage causes the molecular energy levels to vary in relation to the Fermi energy level of the electrode. Bottom: Resonance (black line) and anti-resonance (blue line) around Fermi energy. The black curve is showing the transmission functions of constructive, and the blue curve is illustrating the transmission function of destructive interference effects. This Figure is taken from reference [117] with permission of the publisher, Nature Materials.

The easiest illustration of constructive QI is provided by the Breit-Wigner formula for electrons with energy *E* travelling through an orbital of a single molecule [110]:

$$T(E) = \frac{4\Gamma_1\Gamma_2}{(E-\varepsilon_g)^2+(\Gamma_1\Gamma_2)^2} \qquad \textbf{Equation 2}$$

$\varepsilon_g = E_g - \sum$, is the eigenenergy E_g of the molecular orbital moved by a value of $\sum$ after coupling of the metallic electrodes to the orbital. Γ_1 and Γ_2 are the couplings of the orbital to the metallic electrodes 1 and 2. The Breit-Wigner formula demonstrates that electron transmission is greatest when the electron resonates with the orbital of the molecule, in other words when the energy of electron is equal with the energy of the orbital [110].

In molecular electronics, and in particular single-molecular electronics, one of the key aims is understanding, employing, and manipulating the wave-like nature of the electrons [118,119]. Understanding the relationship between the electronic structure of molecular junctions (as described by the molecular orbitals and their energies) and electrical current, as well as how it may be influenced by chemical design, is essential for understanding the impact of quantum interference. QI has been increasingly used in molecular electronics to control charge transport through molecular junctions and has been a topic of particular interest in single molecule electronics. [120–129]. The ability to control QI allows the adjusting of charge transport through molecular

junctions by manipulating either the destructive or constructive interference of waves traversing a junction [114].

In aromatic rings (molecules with ring planar, continuous unhybridized π orbitals, and odd number of delocalised electron pairs), any adjustment of the atom types inside the ring can affect the QI. Also, fused aromatic rings are excellent candidates for probing QI as they provide different ways to control their connectivity, including conjugation, substitutions, and heteroaromaticity. These features have provided the basis for chemically controlling the electrical properties of a molecular bridge, through the nitrogen heteroatom in the fused aromatic pyrrolodipyridine. This has presented an efficient method to tune QI and molecular conductance [130]. The pyrrolodipyridine offers a locked coplanar geometry to its two aryl units, which provides a stable configuration with no change in the inter-ring dihedral angle. The tricyclic scaffold of these fluorene-like compounds offers a good platform for studying quantum interference through systematic changes. Different bridging atoms and functional groups can be substituted at positions X and R, respectively (Figure 3.2). Also, molecular bridges with meta or para connectivity to the metallic electrodes can be synthesised [130].

It will be shown that the QI characteristic coming from meta-connectivity is driven away from the Fermi energy of the electrodes and effectively turned off in a sequence of meta- pyrrolodipyridines (Figure 3.3).

Fermi level is an estimate of an equilibrium electronic energy of a solid. The Fermi level is assumed to be placed below the bottom of the conduction band and above the top of the valance band. The location of the Fermi level

determines if the solid is a metal, an insulator, or a semiconductor. The valence band is the highest of those filled with electrons, and the conduction band is the next empty band at higher energy [131].

In highly coupled meta- pyrrolodipyridine, the density of the electron on the pyrrolic N can be changed by electron-donating or electron-withdrawing substituents. Modulation of electron density will change the coupling of the lone pair of the N to the aromatic core and thereby the conductance of the molecules. In meta-pyrrolodipyridines, the change in the conductance resulting from different couplings of the lone pair can be controlled; however, in para- pyrrolodipyridines, the conductance remains unchanged. NMR characterisation of meta and para oriented pyrrolodipyridines are shown in Chapter 7, Section 7.1.3.

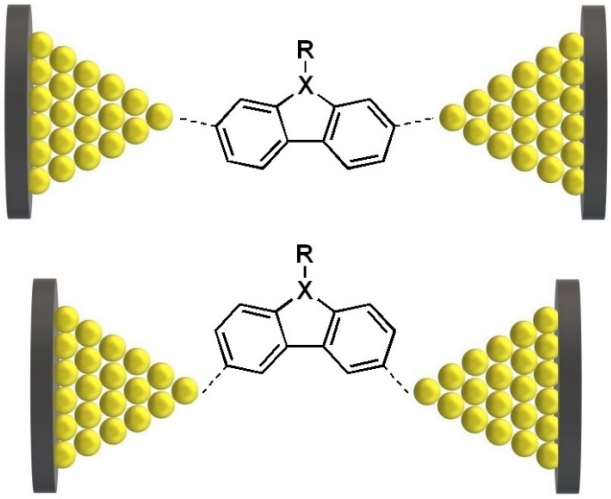

Figure 3.2. Structure of a) para connected and b) meta connected fluorenyl molecules. The dashed lines show the connections to the metallic electrodes here.

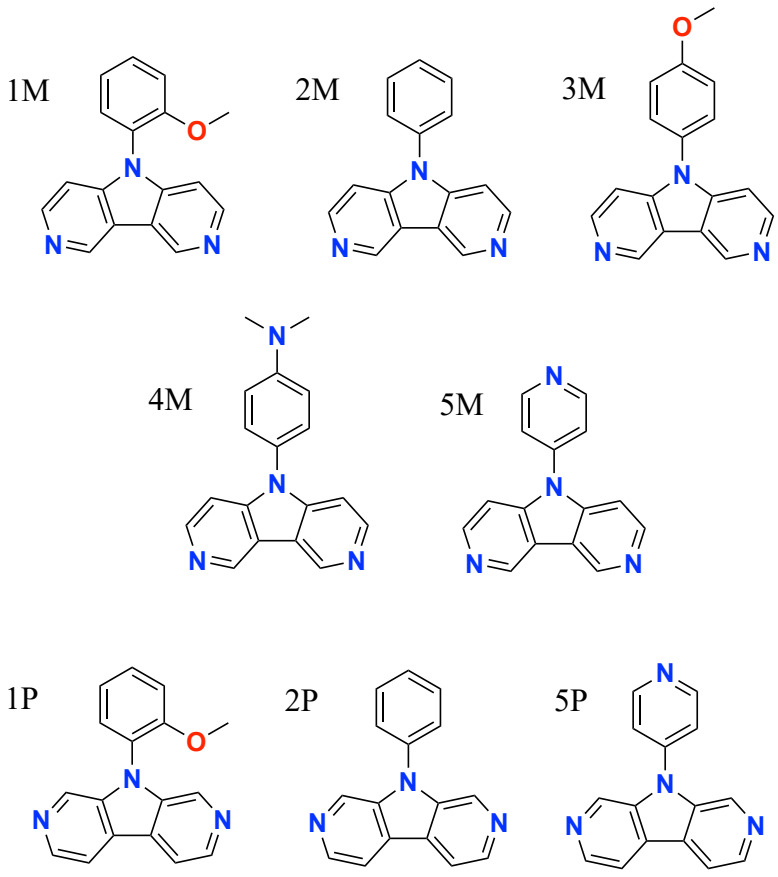

Figure 3.3. Structures of meta (M) and para (P)-connected pyrrolodipyridines used in the study.

Chemical substitution can alter the molecular conductance, and some investigations have been directed towards this [132]. In the system with para connectivity, the change in the conductance is a result of the modification of the aromaticity of the tricyclic system. When X is changed to different substituents which increase the aromaticity, this would decrease the conductance of the molecular junction [133]. On the other hand, the conductance of the molecule with meta connectivity shows no dependence on aromaticity because of the QI effect, and here the charge transport is dominated by the substituents on the pyrrolic N of the molecule in the junction [132,133]. In the case

of the meta connected tricycle, if N is placed at the position X in Figure 3.2 (meta-pyrrolodipyridines), a higher conductance would be observed than O (meta-dibenzofurans) and Si (meta-silafluorenes) in the same position, and this is not in line with the predictions of the conductance being controlled by the aromaticity of the molecule [132,134]. Pyrrolodipyridines show a higher conductance since the lone pair of the N provides better electronic transmission by offering a new pathway which promotes charge transport. This alluring capability of pyrrolodipyridines attracted so much interest in studying the relation between the chemical structure and the QI.

By using different substituents on the pyrrolic N, the electron density of the N changes based on the electron-donating or withdrawing behaviour of the substituents, which has a considerable impact on the conductance of the molecule, while in para-connected tricycles, the conductance remains the same regardless of changes in X (Figure 4). Later on in the Chapter it is shown that there is a decreased influence of destructive QI for meta-connected pyrrolodipyridines and finally a switching off this phenomenon when the QI dip is moved away from the Fermi level of the metallic electrodes. This complements other competing methods of controlling QI, such as the use of the electrochemical or electrostatic potential, which alter the energy alignment with the electrodes Fermi energy [117,135,136].

3.2. Results and Discussion

The conductance of the molecular wires is affected by the presence of different substituents on the pyrrolic nitrogen in the meta-connected molecules (**1M** – **5M**). In the conductance histograms, the conductance characteristics of the meta compounds **1M** – **5M** are shown in the conductance histogram in Figure 3.4a, and the changes in conductance with the pyrrolic nitrogen substituents are apparent. The conductance value of the meta-compounds changes by more than one order of magnitude after altering the substituents on the pyrrolic N. In contrast, the conductance of the para counterparts (**1P**, **2P** and **5P**) is essentially unaffected (Figure 3.4b). Individual conductance histograms of the molecules are presented in the appendices (Chapter 7, Section 7.1.1).

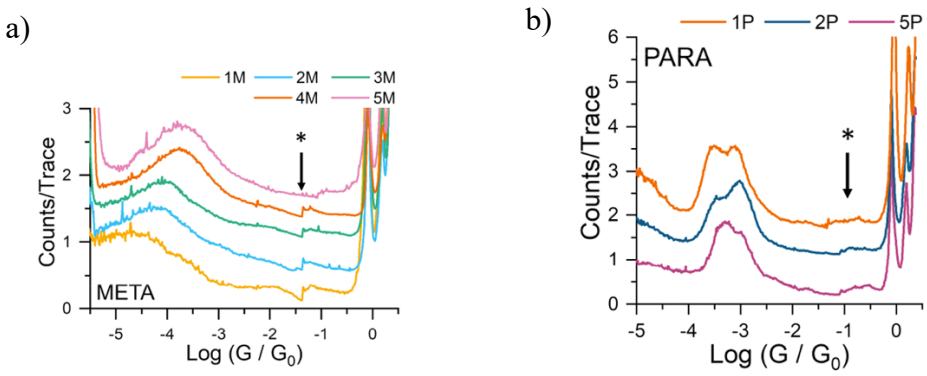

Figure 3.4. **a)** Conductance histogram of molecules **1M** to **5M** and **b)** conductance histogram of compounds **1P**, **2P** and **5P**. Figures taken from reference [130] with the permission of the publisher. The asterisk in the conductance histograms denotes a minor artefact caused by our 4-channel preamplifier transimpedance switch.

Overall, the findings indicate that charge transfer efficiency (molecular conductance of pyrrolodipyridines) and the electronic state of the bridging

pyrrolic N are related. Empirical evidence for understanding how molecular conductance varies across these series of compounds can be obtained by focusing on relationships between molecular conductance and particular parameters used by physical organic chemists. The electrical behaviour of the pyrrolodipyridine junctions is influenced by the charge density on the pyrrolic N atom, and an applicable physical parameter that can be related to the density of charge on the N is the acidity of the protons on the anilinium ions, which corresponds to the aniline building block utilised in the pyrrolodipyridine synthesis (Figure 3.5). When the logarithm of conductance is plotted against the pK_a (in water) of the corresponding anilinium ion (Figure 3.6 and table 3.1), there is a strong relationship with the conductance values of these molecular wires.

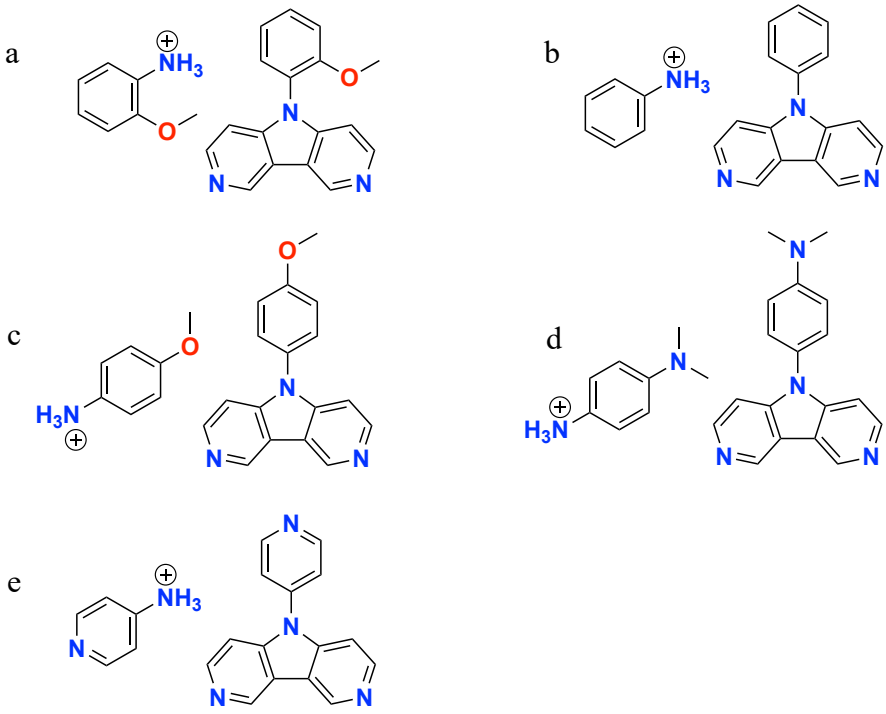

Figure 3.5. Molecular structure of meta- pyrrolodipyridines and the corresponding anilinium ions of the respective substituent. a) **1M**, b) **2M**, c) **3M**, d) **4M** and e) **5M** pyrrolodipyridines.

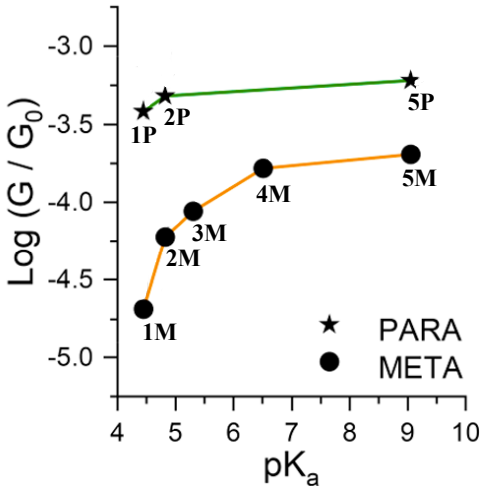

Figure 3.6. 1M - 5M and **1P**, **2P** and **5P** logarithmic conductance vs pKa. The pKa used here is for the anilinium ion derived from the aniline used in the synthesis of the pyrrolodipyridines. pKa value are taken from the CRC handbook of Chemistry and Physics [137].

The correlation between pK_a and conductance values in Figure 3.6 shows an upper limit of ~$10^{-3.7}$ G_0 for conductance that can be obtained for these molecules, and this is evident in the histograms, which show that compounds **4M** and **5M** have very comparable conductance values close to this limit. It is possible to use a simple structural model to explain the results arising from the correspondence between the charge on the pyrrolic N and molecular conductance. A new conductance pathway opens since the lone pair on the N behaves as a mediator for charge transport. This new pathway suppresses the quantum interference caused by the meta pathway and thereby offers higher conductance (as pictorially represented by arrows in Figure 3.7). Higher conductance (up to $10^{-3.7}$ G_0) for the molecular junctions is achieved by increasing the electron density of the pyrrolic N as a result of the higher aryl-aryl coupling offered by the lone pair (Figure 3.4a).

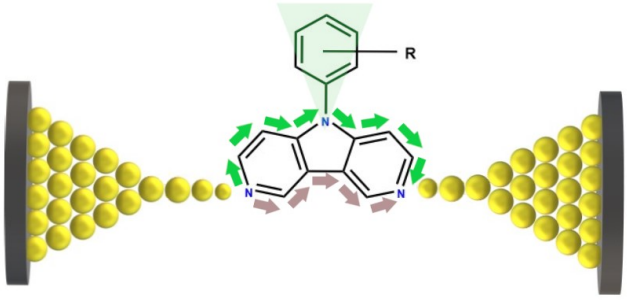

Figure 3.7. Data is interpreted within a model which takes account of quantum interference phenomena arising from current flow through different pathways across the molecular bridge. The charge transport channel (purple arrows) leads to destructive QI. The bridging atom provides an alternate pathway (green arrows), and its efficiency is regulated by the electron density on the pyrrolic N.

For classic electronic circuits following Kirchhoff's law, at any junction in the electrical circuit, the total currents coming to the junction must have the same value as the total current flowing out of the junction. Also, the directed sum of potential variations (voltages) around any closed circuit is zero, which means that in a complete loop of the circuit, the sum of all voltages throughout components that supply electrical energy must be the same as the total of all voltages throughout other constituents in the same loop. However, molecular electronics circuits which are subject to quantum interference effects function in a fundamentally different manner to classical electrical networks. For the classic circuit the overall conductance is simply equal to the sum of the individual contributions of different pathways.

Table 3-1. Molecular conductance values, log (G/G_0) and pKa of the corresponding anilinium ion. For the substances studied in this work, conductance values, errors, and physical constants are shown. [a] Values taken from the CRC Handbook of Chemistry and Physics. There is a substantial relationship between the value of pKa and the conductance of **1M**-**5M**. Changing the pKa value of the corresponding anilinium ions has no effect on the conductance of **1P**, **2P**, or **5P**.

Compound	**Conductance (G_0) / S**	**Log $(G / G_0) \pm \alpha$**	**pKa of the corresponding anilinium ion [a]**
1M	3.2×10^{-5}	-4.7 ± 0.3	4.49
2M	5.6×10^{-5}	-4.2 ± 0.3	4.87
3M	8.3×10^{-5}	-4.1 ± 0.3	5.36
4M	1.6×10^{-4}	-3.8 ± 0.2	6.59
5M	1.9×10^{-4}	-3.7 ± 0.3	9.17
1P	8.3×10^{-4} (H) 3.7×10^{-4} (L)	-3.1 ± 0.2 -3.4 ± 0.4	4.49
2P	1.0×10^{-3} (H) 4.7×10^{-4} (L)	-3.0 ± 0.2 -3.3 ± 0.3	4.87
5P	1.0×10^{-3} (H) 5.9×10^{-4} (L)	-3.0 ± 0.2 -3.2 ± 0.3	9.17

QI effects result from the presence of several routes in a single-molecule junction, necessitating a thorough DFT analysis for a better understanding of the behaviour of the conductance of the molecular junctions studied.

The optically measured and calculated HOMO-LUMO gaps are listed in Table 3.2. Theoretical HOMO-LUMO gaps have been computed for isolated molecules and for the compounds were in junctions. For the latter case the gap quoted is that between their HOMO and LUMO transmission resonances. The HOMO-LUMO gaps for the isolated compounds are bigger than the gaps between transmission resonances for the corresponding molecule in the junction. This is due to the fact that when the molecule is isolated, the broadening of the molecular orbitals is limited due to the weak or no coupling with the electrodes. Only when coupling of the molecular orbitals to the electrode is significant, the electronic states of the molecule and electrodes overlap, causing a broadening of the energy levels of molecules. Therefore, HOMO-LUMO gap E_g is smaller for the molecule connected to the metallic electrodes as $\varepsilon_g = E_g - \sum$, is the eigenenergy E_g of the molecular orbital changed by a value of $\sum$ after coupling of the metallic electrodes to the orbital.

Table 3-2. Theoretical and experimental HOMO–LUMO gaps in eV. **a)** Data from the experiment: Eg = 1241.5/ABS, using UV-Vis spectroscopic technique. **b)** The isolated molecules' theoretical HOMO–LUMO gaps. **c)** Theoretical gaps in Au-molecule-Au structures between HOMO–LUMO transmission resonances.

Compound	**E_g (Exp.) [a]**	**$E_{g\,DFT}$ (Iso.) [b]**	**$E_{g\,DFT}$ (Au-M-Au) [c]**
1M	4.90	3.43	3.30
2M	5.13	3.51	3.30
3M	5.37	3.42	3.30
4M	5.48	3.47	3.30
5M	5.15	3.50	3.30
1P	5.38	3.10	2.90
2P	5.37	3.01	2.85
5P	5.37	2.91	2.70

Transmission coefficient $T(E)$ was calculated for electrons of energy E travelling between the metallic electrodes through a molecular junction by the collaborators at the University of Lancaster [138]. The transmission coefficient $T(E)$ was computed for the compounds **1M**-**5M** and **1P**, **2P** and **5P** (Figure 3.8). Ground state energies, binding energies, molecular conformations, and trends in HOMO–LUMO gaps in molecules can all be predicted using DFT. The main challenge in DFT calculations is finding the correct HOMO and LUMO level locations relative to electrode Fermi energies. The DFT calculations give a slightly smaller HOMO-LUMO gap, and this can be

corrected by experimentally measuring the HOMO-LUMO gap using techniques like UV-Vis spectroscopy measurements. When the HOMO–LUMO is known empirically by measuring the energy gap associated to the maximum wavelength using UV-Vis spectra (Figures are shown in Chapter 7, Section 7.1.2), a scissor correction is applied to the DFT calculations. If the relative locations of the HOMO and LUMO levels to the Fermi energy of the metallic electrodes are identified, the Fermi level ought to be corrected to the right amount. The anticipations for transport characteristics are expected to be the most precise when the two energy differences $E_L - E_F$ and $E_H - E_F$ have been determined by experiment. Without a scissor operator, the LUMO resonance is expected to be fixed around the Fermi Level of the electrode, thus cancelling out the substituent impact on molecular conductance (Figure 3.8a). As demonstrated in Table 3.2, the theoretical and optical bandgap values vary by more than 1 eV, indicating that DFT underestimates this value [139,140].

As mentioned earlier, the HOMO-LUMO gap cannot be correctly estimated using DFT, and the computed gaps are less than the optically determined gaps. To solve the problem, the optical bandgap of the compounds was used to perform a scissor correction [141–143]. Hence, the new HOMO-LUMO gap is consistent with the experimental data of the molecule. Figure 3.9 shows the transmission curves of para-connected molecules after scissor correction. Here, DFT shows a smaller influence on transmission at the Fermi level in these compounds in comparison to their meta counterparts, which leads to independence of the conductance to N-aryl substitution in pyrrolodipyridine.

Since $G = G_0 T(E_F)$, where $T(E_F)$ is the transmission coefficient at the Fermi level of the metallic electrodes anticipated by DFT calculations, the conductance value of the molecular junctions can be derived from the transmission curve.

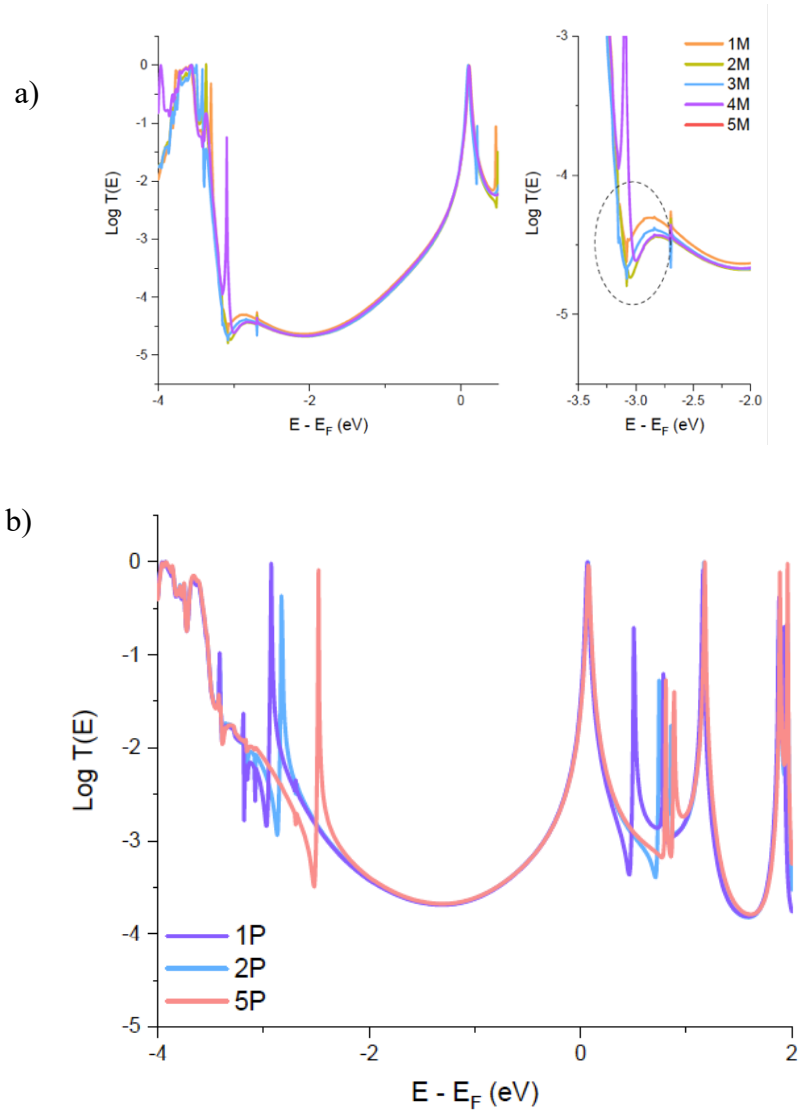

Figure 3.8. a) Transmission curves for meta-connected compounds **1M**–**5M** without the scissor operator (left) and magnification in the area where the quantum interference characteristic appears (right). b) Transmission curves for para-connected molecules **1P**, **2P**, and **5P** without the scissor operator.

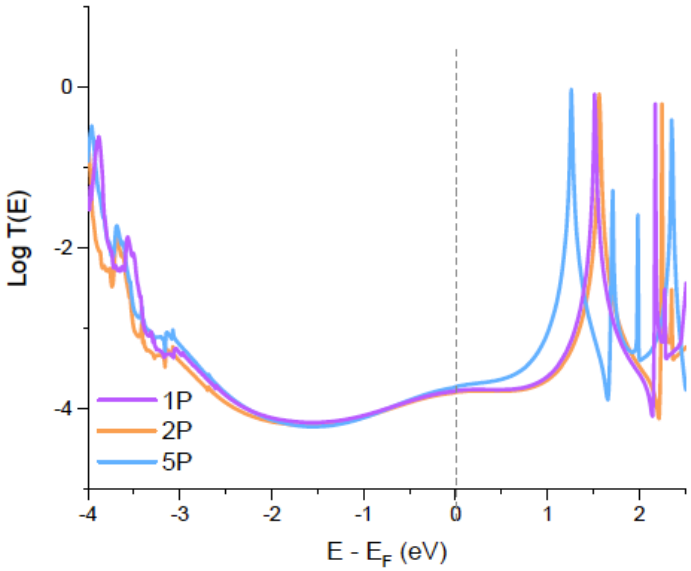

Figure 3.9. Transmission curves with scissor correction for **1P**, **2P** and **5P**.

Since the nano-environment and the local geometry of the metallic electrodes which are continuously changing throughout an STM-BJ experiment dominates the definite position of the Fermi energy of the electrodes, anticipation of the exact position of Fermi level is not easy. As a result, precise prediction of the molecular conductance is not feasible, but essential information about the molecular conductance may be derived from the *T(E)* behaviour within the HOMO-LUMO bandgap where E_F lies. In the calculated *T(E)* profile, all the meta-compounds exhibit a destructive quantum interference resulting in an apparent dip in the transmission curve (Figure 3.8a). However, the dip caused by destructive QI is significantly pushed toward the nonconducting HOMO orbital and is not as severe as that seen in simple meta-connected aryls. The bridging nitrogen atom that connects the two pyridyl rings is responsible for these effects since it causes a significant

asymmetry of the transmission within the HOMO-LUMO gap region (Figure 3.10).

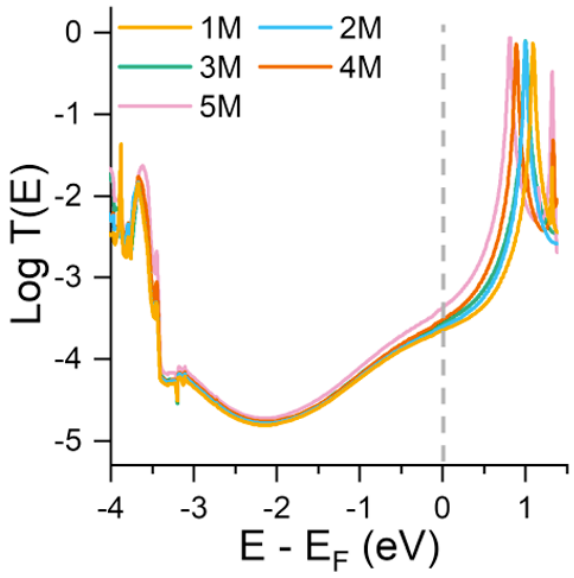

Figure 3.10. Transmission curves for molecules **1M** to **5M** after scissor correction.

This destructive QI is manifested as a dip in transmission curve that is results in the lower conductance of these meta-molecular wires. As discussed earlier, the change in conductance of meta- pyrrolodipyridines across the **1M** to **5M** series can be attributed to variations in the charge density on the pyrrolic N. The theoretical study (DFT calculations) by the University of Lancaster group supports the experimental results (Figure 3.10). This shows that the computed transmission coefficient of the molecular junctions at the Fermi level decreases in the same order as their experimental conductance values drop, i.e., **5M** > **4M** > **3M** > **2M** > **1M**. The decrease in the transmission coefficient in this molecular series is visible in the transmission curve when zoomed in at the Fermi level (Figure 3.11). Note that the LUMO is the closest orbital to the Fermi energy and is therefore said to be responsible for charge transport.

When the log $T(E)$ against $E - E_F$ plot is magnified close to the Fermi energy of the electrode this trend in the transmission coefficient can be clearly seen (Figure 3.11). These results from the transmission coefficient predicted by DFT for meta molecules agree with the experimental data from pyrrolodipyridines break-junction studies.

To assess the *T(E)* behaviour in the HOMO-LUMO gap for the para-connected compounds, the same calculations were performed (Figure 3.9). Transmission curve of para molecules show no dip within the HOMO-LUMO gap, indicating that there is no destructive QI in these molecular junctions. This is in line with the experimental results obtained using the STM-BJ where para molecules show higher conductance.

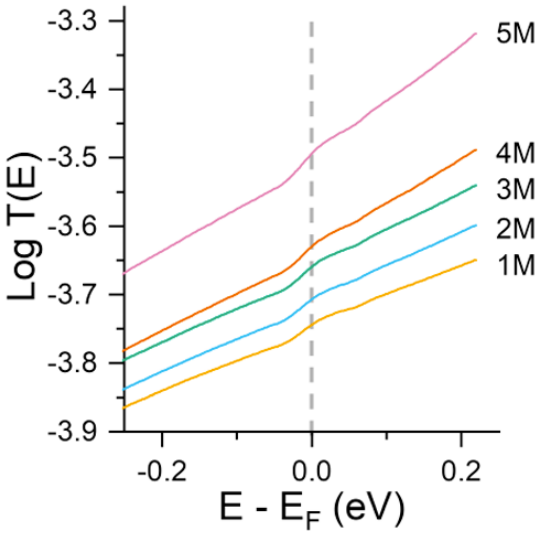

Figure 3.11. Magnified Transmission curve after scissor correction from –0.25 to 0.25 eV for the series of molecular junctions **1M** to **5M**. Fermi energy predicted by DFT is shown as a dotted grey line.

In Figure 3.8a, the energy position of the interference phenomenon is not significantly affected by the substituents on the pyrrolic nitrogen showing the

dip remains close to the non-conducting orbital. For para- pyrrolodipyridines regardless of the type of the substituent on the pyrrolic nitrogen, *T(E)* in the HOMO-LUMO gap remains largely the same. Based on DFT calculations, the transmission coefficient at the Fermi level is affected less in para-compounds, and therefore, the conductance of pyrrolodipyridine is not dependent on the N-aryl substituent (Figure 3.9).

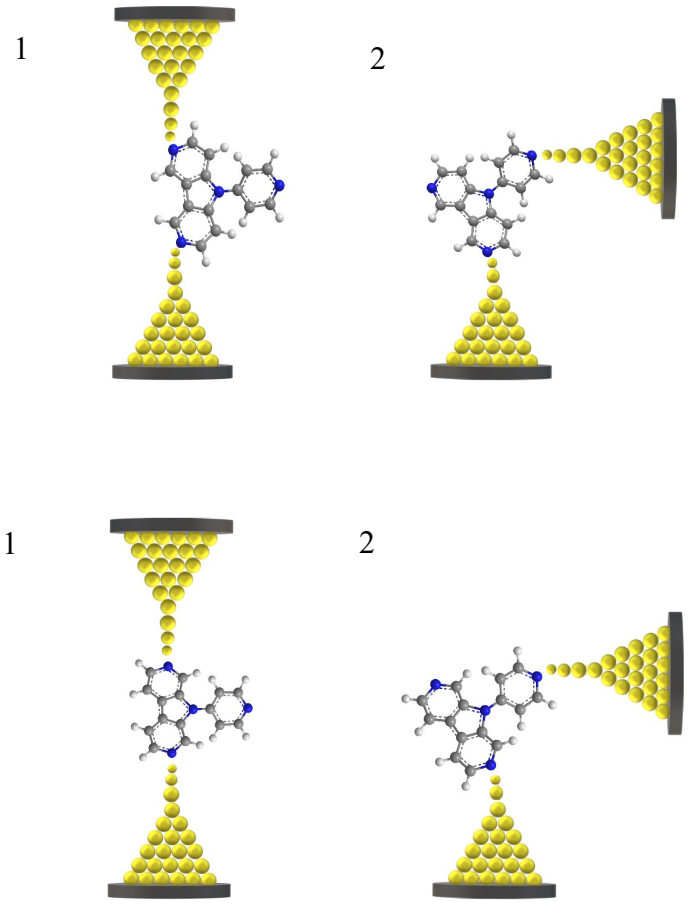

Figure 3.12. Structure and relative transmission curves for the junctions of compounds **5M** (top) and **5P** (bottom) in the two potential binding geometries (left versus right) enabled by the presence of a pendant 4-pyridyl moiety.

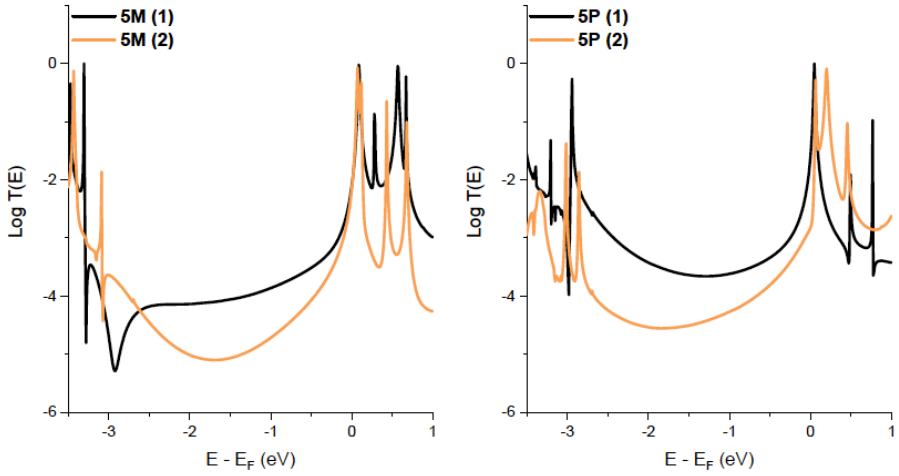

Figure 3.13. The transmission curves are the ones without use of a scissor operator.

The pyridyl ring linked to the carbazolic N of molecules **5M** and **5P** provides an extra binding mode, and in both compounds, this leads to a shoulder with lower conductance in the histograms. DFT transport calculations were done by the team of collaborators at the University of Lancaster to determine which potential geometry which is most likely to be obtained during an STM-BJ experiment for these compounds. As depicted in Figure 3.12, in both compounds (**5M** and **5P**), the geometry which offers a higher conductance is when there is electrode contacting to the pyridyl groups at opposite facing end of the pyrrolodipyridine. In this case, the transmission curve shows a higher transmission probability at the Fermi level of the electrode (black lines in Figure 3.13). The lower conductance originates from the junctions made through the pendant additional pyridyl ring, and the transmission curve confirms the lower transmission probability of this junction geometry (Orange lines in Figure 3.13).

3.3. Conclusion

This study of N-substituted pyrrolodipyridines shows that it is feasible to chemically regulate conductance by altering the substituents and the position of the gold electrode connection to the molecular bridge, i.e. the connectivity. The meta connectivity leads to quantum interference, but this can be progressively switched off in a series of meta-d pyrrolodipyridines by tuning the substitution on the N atom of the pyrrolodipyridines. This is because changing of electron density adjusts the coupling of the lone pair of the N and the aromatic framework of the pyrrolodipyridines, thereby tuning the conductance of the compounds in the molecular junction. In this way it is possible to control the conductance of meta- pyrrolodipyridines by changing the coupling of the lone pair, although, by contrast, the conductance remains the same in para- pyrrolodipyridines. This QI effect arising from the meta connectivity is competing with alternative, high-conductance pathway over a single atom (pyrrolic N), whose density of electron can be modified by convenient chemical substitution in meta- pyrrolodipyridines. In other words, the quantum interference, which is a result of the meta-connectivity trend, and suppresses conductance, can be controlled just by the substitution on a single nitrogen atom in the conductance path.

In this work, an advanced way to dominate quantum interference in molecular junctions by changing the charge on only a single atomic component of the molecular have been illustrated. This approach expands the ways which can be used nowadays to control quantum interference.

CHAPTER 4

MOLECULAR ELECTRONICS OF PILLARARENE

4.1. Background and Scope

One ambitious goal of nano and supramolecular science research has been to attempt to develop practical nanoscopic devices inspired and scaled down from functional macroscopic systems [144–146]. With this in mind, various nanodevices for technical or biological purposes have been created and characterised, [150–153]. A definition of “reaching the nanoscale” is when one device dimension is controllably less than 100 nm. One relatively straightforward way of achieving this is through the assembly of monolayer films. Monolayer devices have been assembled by different molecular deposition techniques, such as self-assembly and Langmuir-Blodgett film formation [154]. Highly compact monolayers made entirely of “molecular wires” have been created in both instances [155,156]. The molecular structure, the interface with the electrode, and intermolecular interactions all contribute to the molecules' spatial arrangement when forming 2D molecular films [157,158].

Intermolecular interactions can complicate the single molecule behaviour by providing alternative conduction pathways in molecular junctions. In this respect, new methods are required for the fabrication and assembly of molecular junctions that minimise the impact of intermolecular phenomena, which complicate the measurement of true single-molecule conductance. Enclosing each molecular wire in an insulating "sheath" may be a possible solution to the problem. When a single-molecule configuration is desired, the sheath aims to inhibit intermolecular interactions and the formation of multi-molecular connections by evenly spacing and separating the molecular wires

arranged on a surface. The focus is on host-guest chemistry since there are a variety of defined systems that have been utilised as host for active molecules, resulting in supramolecular complexes with a variety of interesting applications [159,160].

Organising structures that consist of two or more chemical entities will exhibit specific intermolecular interactions has now grown to the extensive field of supramolecular chemistry. A significant strategy in supramolecular chemistry has been the deployment of host-guest chemistry based on macrocyclic compounds. Unlike linear structures macrocyclic compounds have repeating units with no terminal ends, and they can be formed into symmetrical structures such as cyclic, ring or cavity structures with nanoscale dimensions. The cavity of some macrocyclic structures can accommodate guest molecules which can make them more capable of complexation in comparison to linear compounds with the same number of building blocks. Entropy losses of macrocyclic compounds during complexation can be less than linear compounds as linear ones need to change their structure to form host-guest complexes [161].

Pillararenes are relatively new types of macrocyclic compounds, which have para-alkoxybenzene units connected by methylene bridges at the 2 and 5 positions [162]. Pillar[n]arenes were discovered by accident. In 2008, Ogoshi and colleagues attempted to synthesise phenol-paraformaldehyde resins using a featureless phenolic derivative, 1,4-dimethoxybenzene, that resulted in the discovery of pillar[n]arenes, which are intriguing macrocycles [163]. At first they could not figure out why they achieved high yields of pillar[5]arenes.

Pillararenes have a structure which can be compared with calixarenes. However, there is a noticeable difference between pillararenes and calixarenes, which is the connection position of the methylene bridges, since in calixarenes the phenolic units are connected by methylene bridges in the meta position [162]. Different functional groups can be attached to the rim of pillararenes because of the ease of their synthetic modification (Figure 4.1).

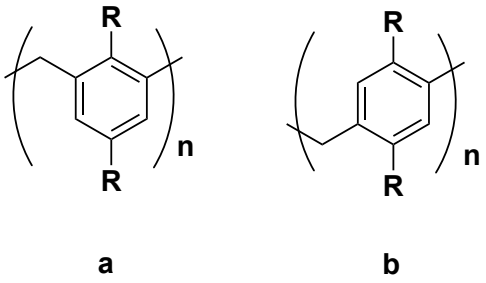

Figure 4.1. Structure of a) Calixarene and, b) Pillararene.

The solubility of the macrocyclic hosts plays an essential role in the ability and selectivity of the host-guest complex formation [164]. The most favourable situation involves very low conformational change during host-guest complexation to keep entropy loss low. This leads to a robust host-guest complexation. Increasing the conformational rigidity is a useful approach to improve the host-guest complexation capabilities. However, very symmetrical structures with rigid conformation can have low solubility.

Macrocyclic molecules such as pillararenes with their spacious cavity are among some of the most desirable compounds in super-molecular chemistry. These compounds have very well-defined cavities to host different guest molecules. The ability of pillararenes to host the guest molecule inside their cavity depends on the size of their cavity and the chemical structure of

constituent units and functional groups. Guest molecules such as viologens are electron-poor cationic molecules. These molecules can reside inside the electron-rich cavity of pillararenes. Pillar[5] and pillar[6]arenes prefer to accommodate electron-poor molecules, such as cationic molecules and molecules containing electron-withdrawing groups, in their cavities [164]. The size of the pillar[5]arenes cavity is approximately 5 Å offers some smaller or "slender" molecules enough space to reside in their cavity, such as pyridinium and imidazolium [165].

Functionalisation of the rim can also be used to control the host-guest complexation. Alkoxy groups on the rims of the pillar[5]-and pillar[6]arene cavities are electron-donating moieties, and they cause a negative inner surface of the cavity of these molecules. On account of the high electronegativity of oxygen, alkoxy groups may be considered electron-withdrawing, however the substitution effect in aromatic compounds can change this situation. Substituent will have different effect when they are bound to the alkyl chain compared to when they are directly bound to benzene rings. In case of a benzene ring, since the substituents can form resonance structures, they may exhibit either electron-donating tendencies or electron-withdrawing ones depending on the exact details.

The inductive and the resonance effects are two especially significant substituent effects. If an atom (or molecule) with a significant level of electronegativity is bound to an alkyl chain, the inductive effect influences the single bonds (σ-bonding). On the other hand, the resonance effect has impact primarily through the double or triple bonds (π-bonding). As an

example, the acidity of aromatic carboxylic acids is strongly influenced by the resonance effect. The acidity of aromatic carboxylic acid will vary based on the type and position of substituents that are bonded to the phenyl ring. When the acidity strength of a substituted aromatic carboxylic acid (pKa) is compared to the acidity strength of aromatic carboxylic acid itself (pKa_H), it is observed that the type of the substituent and its ring position (meta, or para) can alter the pKa significantly. The pKa values of the respective compounds may be represented as:

$$\sigma = pka_H - pka \qquad \textbf{Equation 3}$$

The pKa value varies according to the position of the substituent on the aromatic ring (meta or para). The substituent is electron-donating when σ is negative and electron-withdrawing when σ is positive. In the case of an alkoxy group, if the substituent is in the para position, it works as an electron-donating group, dispersing negative charge via the inductive/resonance effect and stabilising the molecule; if the substituent is in the meta position, it acts as an electron-withdrawing group.

The *I*(*s*)-STM method has been previously used to investigate the conductance of host-guest complexes comprised of cucurbituril and viologen molecular wires moieties, with the viologens being effectively complexed by crown ethers on the cucurbituril (CB) host [166]. Complexation of viologen molecular wires within CB host led to an increase in the molecular conductance.

The work in this Chapter focusses on pillar[n]arenes (P5A), which have good characteristics for chemical sensors based on host-guest processes. P5As have

high association constants, and they can be spontaneously deposited on surfaces, forming layers[167–169]. Although a large number of molecules have been discovered to function as cavity guests inside the P5A, none of them has been studied using single molecule electronics methods [165,170–172].

This Chapter describes how pillar[5]arenes may function as a supramolecular hosts for a molecular wire that is extensively used as a molecular wire (oligophenyleneethynylene, OPE). It is shown how the pillar[5]arenes-OPE complex can be self-assembled and used to fabricate dense monolayers. It is then demonstrated how the pillar[5]arene forms a "molecular sheath" for the OPE, thereby inhibiting the formation of dimeric connections by separating and blocking the interaction between single-molecule wires.

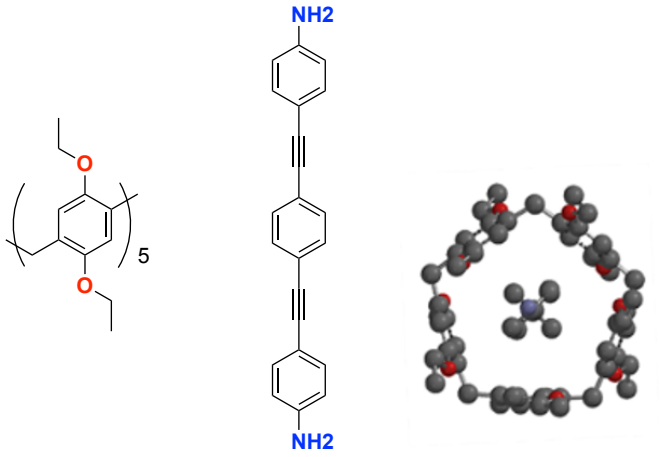

Figure 4.2. Chemical structure of compounds **2** (pillar[5]arene) and **4** (oligophenyleneethynylene (OPE)), and molecular models for the host-guest complexes **2⊂4**.

The conductance of the OPE-P5A guest-host complex has been determined using the STM-BJ technique. To enable the formation of single-molecule junctions, an amine-terminated OPE with amine termini on both ends was

deployed. The **2⊂4** (P5A and OPE) complex for the single-molecule electronics measurements, featuring the OPE with amine termini at both ends, is illustrated in Figure 4.2. Unfunctionalized P5A was used so that it could not interact with the metallic electrodes and served only as a non-conducting sheath. NMR characterisations of **2**, **4** and **2⊂4** are shown in Chapter 7, Section 7.2.1.

4.2. Results and Discussion

It has been shown in the literature [173] that aromatic molecular wires can stack in molecular junctions. Such stacking of the aromatic conjugated molecular wires leads to dimeric junctions in which each monomer is bound to the respective electrodes via just one of its termini. For such dimeric molecular junctions charge tunnels through a new eigenchannel formed by the efficient π-π interaction. This effect can be seen in oligophenylenes, imidazoles, (oligo)thiophenes and also oligophenyleneethynylenes (OPEs) [174]. Charge transfer via stacked dimers is linked with lower conductance values than the equivalent single-molecule junctions because the channel formed by the non-covalent π-π connection is usually less transparent to tunnelling than covalent interatomic bonds [175–177]. The experimental work presented here shows that these π-stacking phenomena can be impeded through molecular encapsulation.

Single-molecule charge transport characterisation was carried out using the scanning tunnelling microscopy - break junction (STM-BJ) method. STM-BJ

measurements in air have been compared with those in solvents. To demonstrate the formation of stacked junctions, STM-BJ measurements in air on a sub-monolayer of compound **4** was performed. Adsorption of compound **4** on gold was achieved placing a droplet of a 1 mM acetone solution on the gold slide for one hour and then rinsed with ethanol. Figure 4.3c indicates that the π stacking junction significantly contributed to the conductance histogram, which features a most intense peak at $\sim 10^{-5.3} G_0$, as, as well as a secondary peak at $\sim 10^{-4.2} G_0$. By taking the electrode snapback of 0.6 nm into account, the junction extension distance of the intense peak at $\sim 10^{-5.3} G_0$ corresponds to electrode separations greater than the length of molecule. This shows that this signal originates from stacked dimers rather than monomers [159]. From these results recorded with the STM-BJ in air it is concluded that π stacking occurs strongly for this compound.

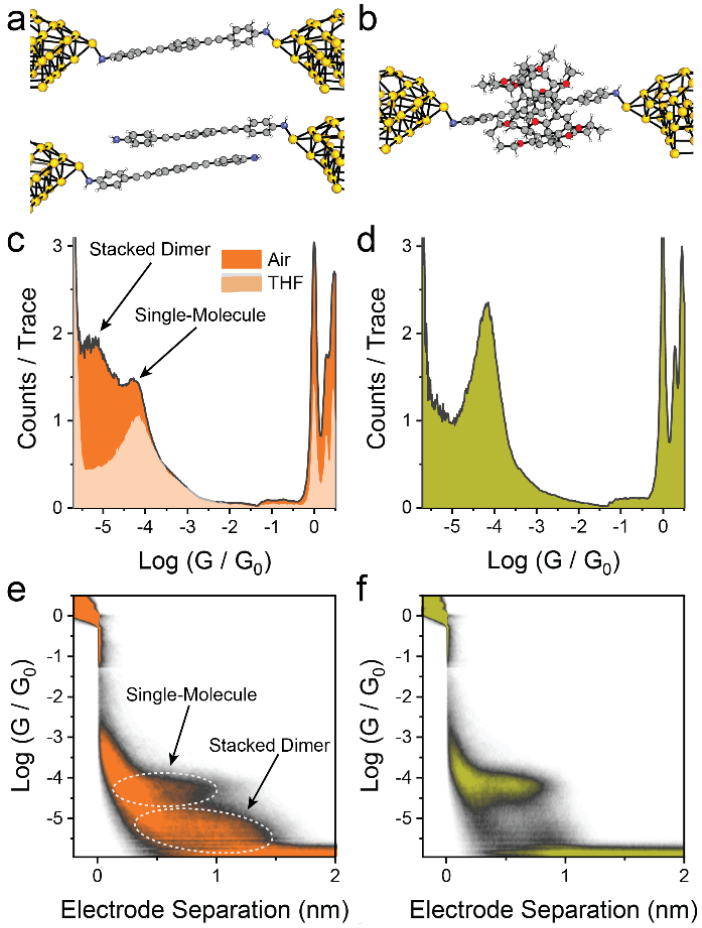

Figure 4.3. STM-BJ studies. (a) idealised structures of a single-molecule junction of **4** (top) and its stacked dimer (bottom) for qualitative demonstration of the junction. The length of the junction in the top and bottom models do not correspond to the actual configuration of the molecule(s) in the junction. (b) structure of the **2⊂4** complex junction. (c) 1D conductance histogram of **4** measured in air, 200 mV bias (dark orange) and in THF (bright orange). (d) 1D conductance histogram for the complex measured in air, 200 mV bias. (e) Conductance – electrode displacement density map for **4** in air. (f) Conductance – electrode displacement density map for **2⊂4** in air. Histogram and density map in (c) and (e) compiled from 5209 traces with no data selection. Histogram and density map in (d) and (f) compiled from 5209 traces with no data selection. Histogram for **4** in THF (c) normalized at 0.5 intensity. Colours in (a) and (b): C = grey, N = blue, H = white, O = red, Au = yellow. Dashed contours in (e) as guide to the eye.

Next the measurements in air just described are compared with those made in solvents to see if the environment effect formation of the stacked dimer. Conductance measurements of compound **4** were performed using the break-

junction technique in an 8:2 v:v mixture of mesitylene and tetrahydrofuran. It is apparent that there is no detectable formation of stacked dimers as only a single conductance peak at $\sim 10^{-4.2} G_0$ exists in the histogram (Figure 4.3c) (individual histograms are shown in Appendices Chapter, Section 7.2.2). Therefore, solvation of **4** in mesitylene/THF prevents the formation of dimers.

Next a gold substrate was incubated in an equimolar solution of **2** and **4** for one hour, followed by STM-BJ measurements in air. Only the single-molecule conductance peak is observed, and the conductance versus electrode separation density map did not reveal any notable characteristics beyond the molecular length of **4** (Figure 4.3d). The appearance of a single peak associated to the single-molecule junction in Figure 4.3d indicates that the pillararene cage prevents through-space tunnelling arising from pi stacking of **4** if the ratio of **2** and **4** is 1:1.

Flicker noise analysis was performed on the junctions to establish the supramolecular nature of the junctions generated with molecule **2** in air. Flicker noise measurements can clearly distinguish between through-bond and through-space coupling at the single molecule level. Using this technique, which analyses the current signal of molecular junctions in the frequency domain, the noise power is calculated by integrating the power spectral density across a frequency window. The range between 100 Hz and 1 kHz was chosen here. The noise power will correlate with a power-law dependency of the conductance ($NP \propto G^n$), with the scaling exponent n being near to 1 when charge transport is entirely through-bond. This rises towards $n = 2$ when charge transport includes a through space contribution.

Figure 4.4 presents the results for compound **4**, showing normalised noise power versus average conductance, in order to evaluate their relationship. Since their conductance values are too close as can be seen in this Figure, the contributions from the stacked dimer and single-molecule junction cannot be distinguished from one another. However, the overall noise power follows the power-law dependence with a scaling exponent of about 1.5, showing through-space tunnelling plays a significant role in charge transport. By contrasts, flicker noise measurements of the complex **2⊂4** (Figure 4b) gave a scaling coefficient of about 1.1, illustrating the through-bond tunnelling is responsible for the charge transport.

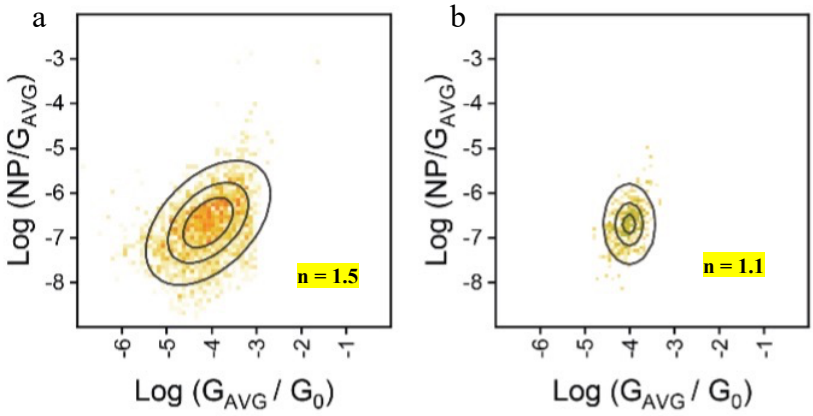

Figure 4.4. (a) Power spectral density (PSD) flicker noise analysis for **4. A** scaling exponent (n) of 1.5 confirms the existence of both through-bond and through space couplings (b) PSD flicker noise analysis for the **2⊂4** complex. A scaling exponent (n) of 1.1 confirms the existence of predominantly through-bond coupling due to successful encapsulation of **4** by **2**. Flicker noise heatmaps in (a) and (b) compiled from respectively 12706 and 15282 traces using the data analysis routine described in Chapter 2. Solid contours in (a) and (b) are the 25%, 50% and 75% height of the 2D Gaussian fit to the map.

To further investigate the efficiency of pillararene in blocking π-stacking and through-space tunnelling in the junction, the STM-break junction method was used to study another conjugated aromatic compound (4-(methylthio)phenyl)-2,2':5',2''-terthiophene (compound **5**) (Figure 4.5). The charge transport through **5** allows to further explore the significance of intermolecular contacts in the junction. The STM-BJ measurements on these thiophene target molecules with just one thiomethyl (-SMe) anchoring group, described in the text below, show that they form stacking junctions with detectable conductance. These STM-BJ characterisations were performed in mesitylene-THF (9:1 v:v) for compound **5** with a gold substrate and tip.

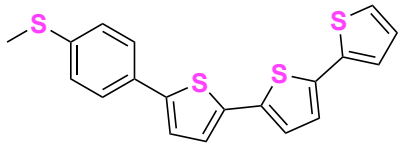

Figure 4.5. Chemical structure of (4-(methylthio)phenyl)-2,2':5',2''-terthiophene (Compound **5**).

Figure 4.6a shows 1D and 2D conductance histogram for **5** in mesitylene and THF (9:1 v/v) which give a main peak at $\sim 10^{-3.1} G_0$. Since **5** only contains a single thiomethyl anchoring groups this indicates that π-stacking junctions are formed as thiophenes are considered to be poor anchoring groups [178]. After adding the electrode snapback of 0.6 nm, the main conductance feature at $\sim 10^{-3.1} G_0$ in the 2D histogram which is attributed to the stacked dimer shows an electrode break-off separation of about 1.2 nm. This extension is very close to the length of this compound (~1.3 nm, measured using Spartan

20). After further elongation of the tip, a second peak appears at lower conductance ($\sim 10^{-4.9}$ G_0) which is related to formation of a differently configured stacked dimer (Figure 4.6a). The conductance peak at the lower value has an electrode separation of 1.45 nm. The higher conductance peak is associated with shorter dimer, while the lower conductance peak is associated with longer dimer. The junction lengths measured from the 2D histograms after addition of the snapback correction correlate well with these respective stacked dimer structures.

The same experiment was performed for a solution of **2⊂5** using the STM-BJ. In this case no clear single-molecule conductance peak was detected. The conductance versus electrode separation density map (2D histogram) showed no notable characteristics of the formation of the junction for the measured equimolar solution of **2⊂5** (Figure 4.6b).

This can be interpreted as the pillararenes sheath encapsulating the lead molecule and thereby preventing formation of stacked dimers. Next a 1:2 solution of **2⊂5** was measured with the STM-BJ to characterise the junction in the presence of an excess amount of **5** in the solution. Figure 4.6c shows in the presence of excess **5** peaks at $\sim 10^{-3.1} G_0$ and $\sim 10^{-4.9}$ G_0 appear. These conductance peaks correspond to the π-stacking junction, showing that when there is not enough pillararene cage to host all of the guest molecules the excess of **5** then leads to π -stacked dimers.

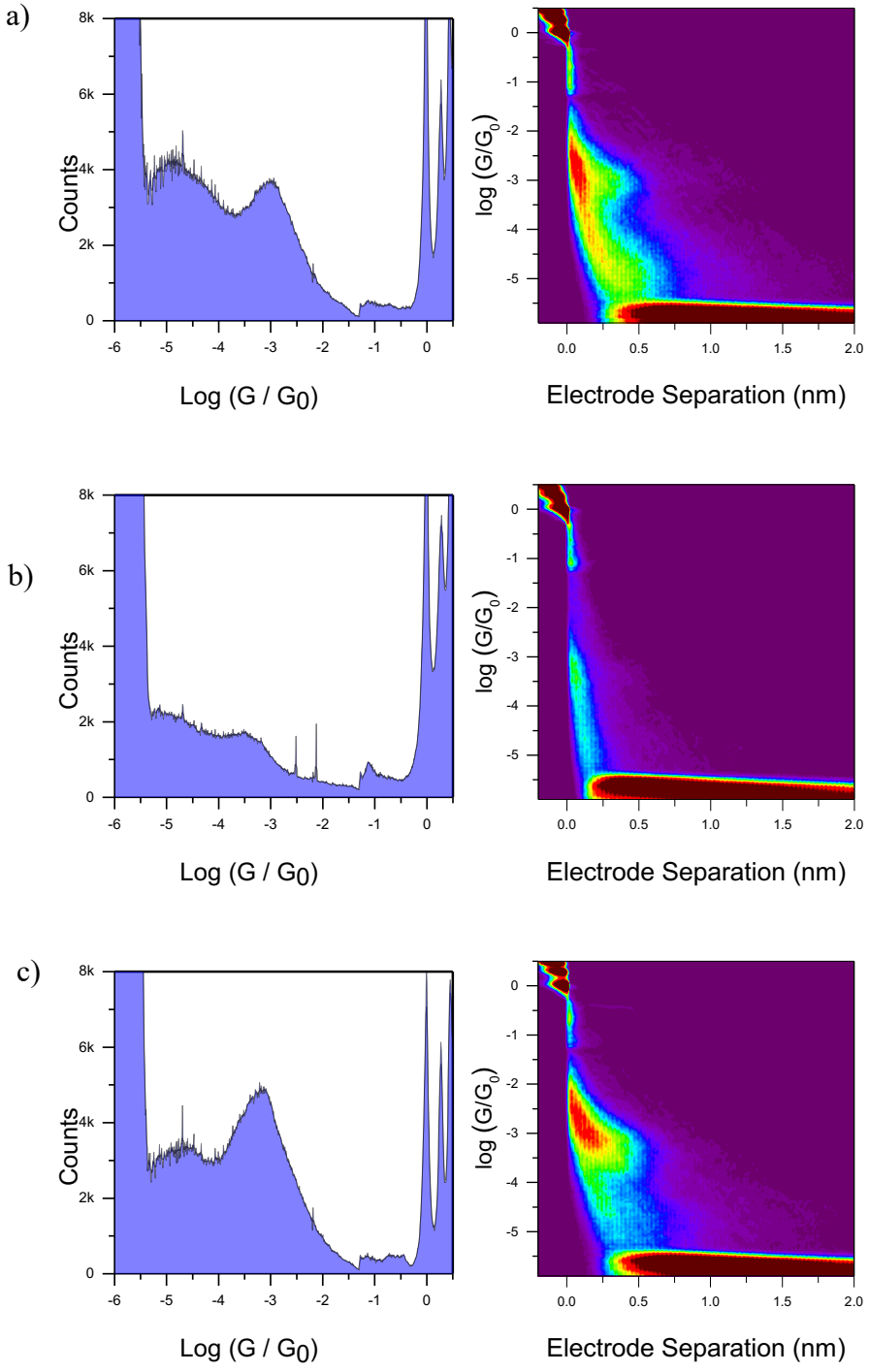

Figure 4.6. STM-BJ measurements for a variety of solutions containing **a**) compound **5** only, **b**) equimolar quantities of **2** and **5** to stoichiometrically form **2⊂5** host guest complex and **c**) a solution of **2** and **5** used to form **2⊂5** where, however, the concentration of **5** is twice as much as **2**. Measurement recorded at 0.2 V bias for 1 mM solutions in mesitylene and THF (9:1 v/v). Histogram and 2D density map compiled from a) 4836 b) 4731 and c) 4228 individual scans, no data selection, 100 bins / decade, 100 bins / nm.

4.3. Conclusion

It has been demonstrated that compound **4** shows through-bond and through-space tunnelling in the junction. The charge transfer through stacked dimers results in a lower conductance value in comparison with through-bond tunnelling in the single-molecule junction. The π stretched junction showed the most intense peak, along with a secondary peak at higher conductance related to the single-molecule junction. When the **2⊂4** complex was measured using the same technique, only the single-molecule conductance peak emerged. It has not been possible to observe any notable characteristics beyond the molecular length of compound **4** at the presence of **2** in the conductance versus electrode separation density map. The conductance of compound **5** was measured using the break-junction method, and multiple conductance peaks related to the formation of different π stacked junctions were seen. Then the **2⊂5** complex was measured, and no conductance peak was seen in the histogram. Flicker noise analysis confirmed the occurrence of both through-bond and through-space tunnelling for compound **4**, while the **2⊂4** complex showed only through-bond tunnelling in this analysis.

These findings give insights into the control and monitoring of molecular assemblies and devices at the nanoscale, as well as fundamental knowledge of the regulation of intermolecular transport. This study could aid in the development of single-molecule investigation of supramolecular structures, as well as providing inspiration for a variety of creative design techniques for the fabrication of high-performance organic devices based on molecular designs exploiting intermolecular interactions.

CHAPTER 5

SINGLE-MOLECULE ELECTRONIC STUDIES OF VERDAZYL

5.1. Background and Scope

Many radicals are highly reactive, but some substances exist in their pure form as stable radicals [179–183]. One of the most stable radical classes are verdazyl radicals which show complete redox reversibility [184,185]. The unpaired electron is delocalized on the verdazyl ring's N_1–N_2–C_2–N_3–N_4 atoms (Figure 5.1).

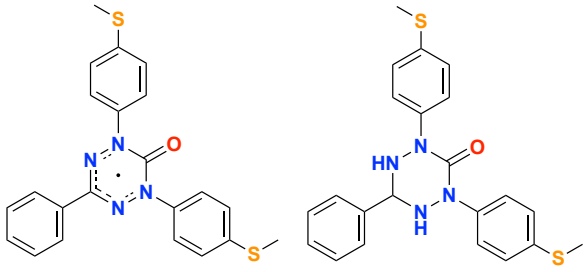

(1) **(2)**

Figure *5.1.* Molecular structures of the oxoverdazyl (**1**) and tetrazin-3-one precursor (**2**).

The unpaired electron's delocalization is the primary explanation for the remarkable stability of the verdazyl radical [185–187].

Intramolecular interaction of the unpaired electron with a pair of electrons of a donating group or the empty π^* orbital of an electron-withdrawing group may occur and lead to delocalisation effects which can be explained using molecular orbital theory and molecular orbital diagrams. Since the HOMO of the radical is singly occupied, the orbital is called the SOMO (Singly Occupied Molecular Orbital). In the case of an electron-donating group, a new lower-energy filled bonding-orbital and a singly occupied new SOMO that is higher in energy than the original SOMO are made due to the SOMO

interaction with the lower energy lone pair. While the energy of the unpaired electron has raised, the energy of the lone pair producing the new bonding orbital has decreased, resulting in a net drop in the molecule's energy. Electron-donating groups, therefore, assist in the stabilisation of radicals (Figure 5.2a).

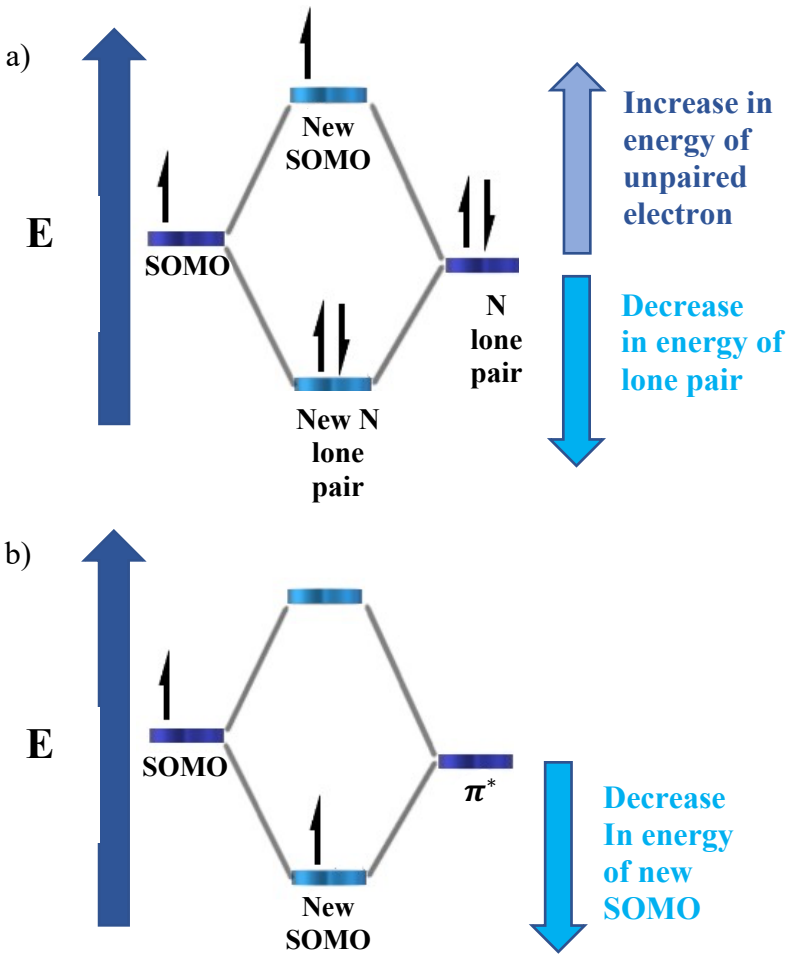

Figure 5.2. Molecular orbital diagram of a radical interacting with **a)** an electron-donating group and **b)** an electron-withdrawing group.

Several stable, organic open-shell compounds have been prepared and characterised since synthesis of the triphenylmethyl (trityl) radical by Gomberg in 1900 [188], and they have been deployed in devices like batteries,

and light-emitting diodes [189]. Semi-occupied molecular orbitals (SOMOs) in open-shell materials within molecular junctions have energies near to the Fermi level of metallic electrodes, which is a desirable property in molecular electronics [110,190] . Such orbitals cause an extra transport resonance around the electrode Fermi level, resulting in high efficiency of transport and desirable traits like rectification and non-linear characteristics [191]. The effect can be computationally modelled and seen in the transmission curve (the probability of an electron tunnelling through a molecular wire as a function of its energy). The presence of a SOMO causes constructive quantum interference and induces multiple sharp transport resonances (spin-up and spin-down) close to the Fermi energy of the metallic electrodes. Therefore, such open-shell orbitals in the junction leads to sharp transport resonances at the electrode Fermi level in the transmission function $T(E)$ [192], as shown in Figure 5.3a.

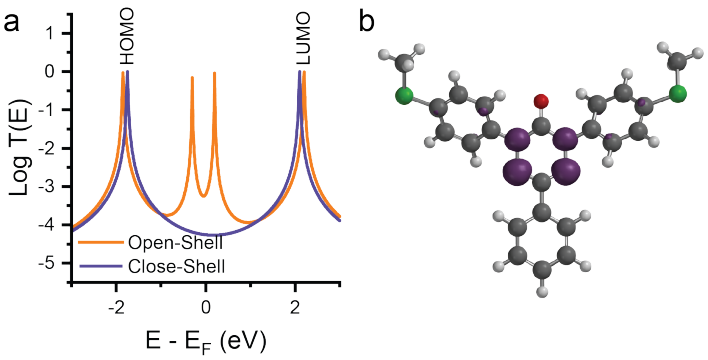

Figure 5.3. a) A transmission curve for a closed-shell and an open-shell material is shown as an example. Additional resonances at the Fermi energy of the metallic electrode exist in the open-shell (radical) molecule. **b)** Map of spin density (purple) for the radical **1** (oxoverdazyl) (B3LYP/6-31G DFT, Spartan '18).

Organic radicals have potential to be deployed in molecular thermoelectrics [115,193,194] and spintronics [195–198], in addition to their favourable charge transport attributes. All previous efforts to include stable organic radicals in single-

molecule measurements at ambient temperature have arisen at the radicals losing their open-shell nature [199], or they have ended up not showing the predicted boost in charge transport efficiency [200]. These results are not unexpected because the materials employed possessed either a strongly delocalised radical state (polyhalogenated trityl compounds) [201,202] or a low oxidation potential (-0.29 V versus Fc/Fc^+ for a Blatter radical, to [199], which resulted in disappearing the SOMO when in contact with the metallic electrodes. Blatter radicals are the type of radicals with three functional aromatic sites. They are versatile since each aromatic site gives various opportunities for modifying their characteristics.

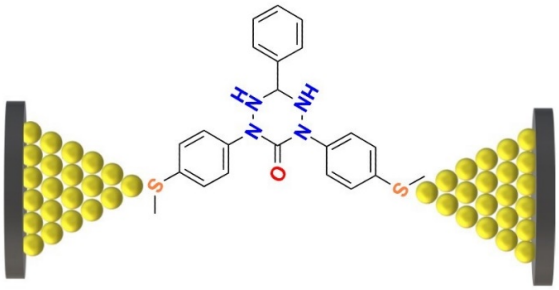

Figure 5.4. Illustration of **2** in contact with two Au electrodes as a single-molecule junction.

In this Chapter, the oxoverdazyl (**1**) (Figure 5.4b) can be wired into a single-molecule junction between two gold electrodes. In such junctions it retains its radical character and exhibits significantly improved conductance value comparing to its closed-shell tetrazin-3-one precursor (**2**) (Figure 5.4a). These findings are related to the heteroatomic and poorly conjugated structure of molecule **1**, which results in a powerful localisation of the radical state [203] on the nitrogens of the oxoverdazyl core (as anticipated by the determined spin

density map in Figure 5.3b) [184]. This enables molecule **1** to preserve its radical character, even when in contact with the two metallic electrodes at ambient temperature. The existence of a radical state in the single-molecule junction is demonstrated by reversible in situ electrochemistry of compound **1**. The in-situ electrochemical STM-BJ also demonstrates single-molecule transistor characteristics of **1**. The presence of the localised SOMO also imparts other significant features to the single-molecule device, including rectification and nonlinear current-voltage characteristic. UV-Vis characterisation of **1** and **2** are shown in Chapter 7, Section 7.3.3.

5.2. Results and discussion

With a conductance peak placed at $10^{-3.4}$ G_0, the oxoverdazyl radical **1** (Figure 5.5) shows an order of magnitude higher conductance than its closed-shell counterpart **2** ($10^{-4.3}$ G_0) (Figure 5.6). Following further analysis, it is determined that the molecule is extended to its stretched form inside the junction. This is concluded from analysis of features in the 2D histograms of conductance versus distance. 2D histograms were generated without data selection for **1** and **2** and these are shown in Figure 5.5 and 5.6, respectively. In both cases sloping conductance "clouds" from electrode separations just after breaking of the Au-Au contacts to ~0.6 nm. Here the junction conductance decreases with elongation until a fully expanded junction is created shortly before the junction ruptures. This junction rupture distance in the 2D histograms is sued to estimate the maximum extension of the

molecule junction. The plateaus corresponding to the molecular junctions extend to electrode separations of 0.6 nm (1.2 nm considering for the electrode snapback). This value of 1.2 nm is in excellent accordance with the molecular lengths of **1** and **2**, which were computed using density-functional theory (DFT, Spartan '18, B3LYP/6-31G) to be 1.35 nm, 1.29 nm for compound **1** and **2**, respectively.

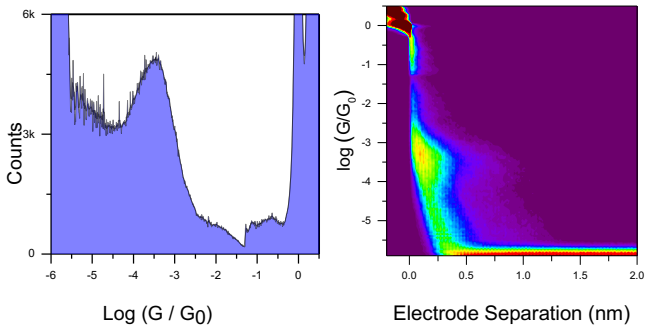

Figure 5.5. STM-BJ measurements for Au|**1**|Au junctions at 0.2 V bias in 1 mM in mesitylene. Histogram and 2D density map compiled from 7807 individual scans, no data selection, 100 bins / decade, 100 bins / nm.

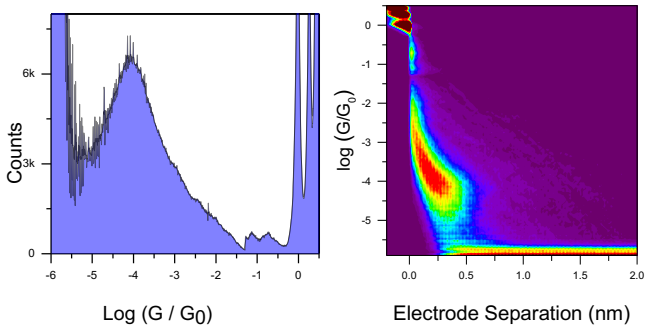

Figure 5.6. STM-BJ measurements for Au|**2**|Au junctions at 0.2 V bias in 1 mM in mesitylene. Histogram and 2D density map compiled from 7322 individual scans, no data selection, 100 bins / decade, 100 bins / nm.

Calculations of the zero-bias transmission coefficient of **1** and **2** were made using DFT to understand further the conductance behaviour of the molecules. These were performed by the collaborators at University of Warwick. For **1**, a pair of strong resonances (spin up and spin down) originating from the existence of a SOMO (that is, ∝- HOSO (spin-up) and β-LUSO (spin-down) frontier spin orbitals), is found near to the Fermi level, but in **2**, only a large HOMO-LUMO gap is seen (see Figure 5.7). Within the whole HOMO-LUMO gap, the existence of the two sharp SOMO resonances boosts the value of $T(E)$ for compound **1** beyond 10^{-3}. On the other hand, for of closed shell compound **2** the Fermi level is shown to be towards the bottom of a transmission function dip in the large HOMO-LUMO gap in the transport profile (see orange curve in Figure 5.7)**.**

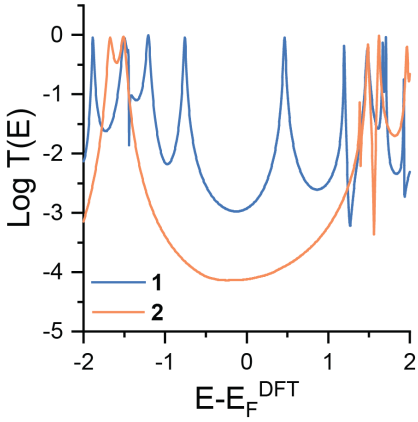

Figure 5.7. Transmission curves for compounds **1** and **2** relative to the Fermi energy of the electrodes.

Compound **1** exhibits electrochemically reversible one-electron oxidation to its monocation and one-electron reduction to the monoanion, just like other 6-oxo-verdazyl radicals (see Figure 5.8) [184]. This defined electrochemical behaviour offers the opportunity to switch **1** between its open shell radical

state and the closed shell state (reducing from the open shell radical to the closed shell anionic form). Therefore, in order to show that the enhanced conductance of **1** is a result of charge transport assisted by a SOMO, single-molecule experiments under electrochemical control were performed.

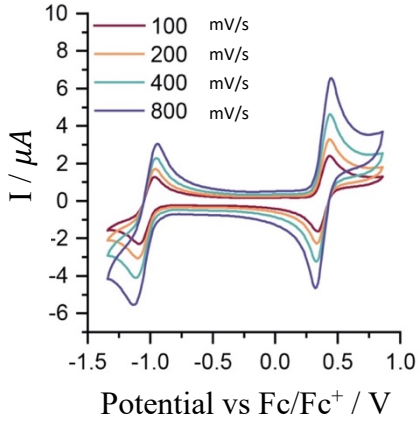

Figure 5.8. Cyclic voltammetry of compound **1**, with 0.1 M tetrabutylammonium hexafluorophosphate as supporting electrolyte after degassing with CH_2Cl_2. Potentials are referenced to the decamethylferrocene/decamethylferrocenium redox couple.

The electrochemical behaviour of **1** was also determined in the ionic liquid using cyclic voltametric techniques. The reduction of **1** shows adequate chemical reversibility and quasi-reversible electrochemical characteristic (Figure 5.9). Open-shell **1** can be cycled between the neutral radical and the anionic state. Upon moving to 0 V (vs Fc/Fc^+), **1** was irreversibly oxidised to cationic state. This behaviour is attributed to the insolubility of the cationic molecule in ionic liquid (1-butyl-3-methylimidazolium triflate). As the voltage becomes less positive, it precipitates and prevents its reduction.

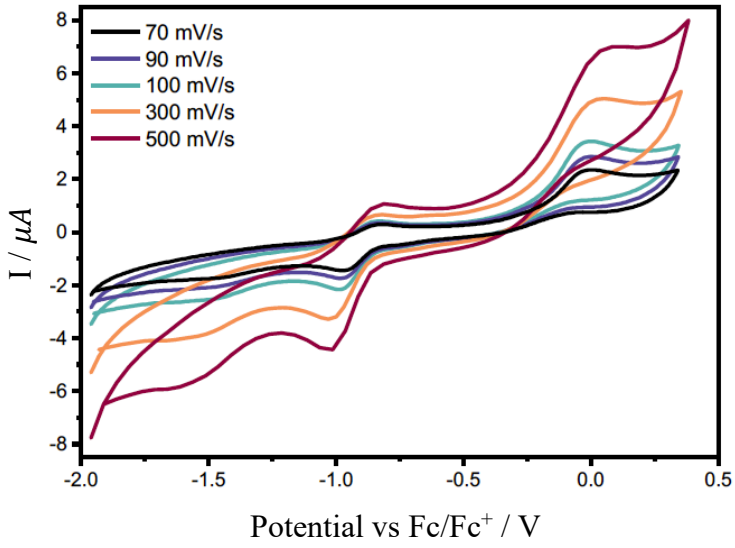

Figure 5.9. Cyclic voltammetry of 1 in the ionic liquid 1-butyl-3-methylimidazolium triflate. Au disk working electrode, Pt wire counter-electrode and Pt wire pseudo-reference electrode. Potential referenced to the ferrocene/ferrocenium redox couple using ferrocene as internal standard.

To perform the STM measurements under electrochemical control, a bipotentiostat was used to apply a voltage between the STM gold tip and substrate (the working electrode) and a Pt counter-electrode against an Ag/AgCl reference electrode (Figure 5.9). All but the very end of the STM tip is protected with Apiezon wax [202] to decrease faradaic current.

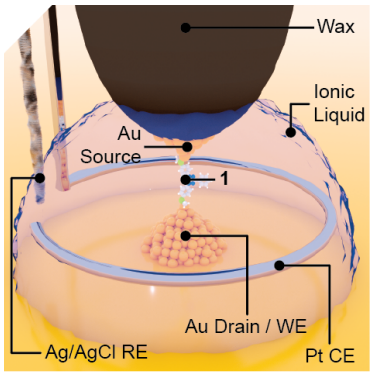

Figure 5.10. The molecular junction is shown in place in the 4-electrode configuration system, which was employed for the single-molecule electrochemical gating.

The bipotentiostat keeps the Au tip continuously biased against the substrate so that the STM tip is a second working electrode. In effect, the STM tip and gold substrate operate as the source and drain in the electrochemically gated setup. The STM-BJ technique is employed to form the molecular junction with compound **1** in the ionic liquid (1-butyl-3-methylimidazolium triflate) electrolyte [203]–[205]. This configuration had an open circuit potential of around -0.4 V against the ferrocene/ferrocenium redox pair. From 0.5 V to -0.8 V against Fc/Fc^+, the conductance of **1** stayed at levels similar to those achieved without electrochemical control (Figure 5.11). When **1** is in its open-shell state in the potential window, from 0.5 V towards -0.8 V the conductance values remain almost the same (higher than the closed-shell state).

When the potential is lowered more to -1 V vs Fc/Fc^+, the conductance of **1** decreases by nearly an order of magnitude and then proceeds to drop when the potential is decreased more. For the reduced **1**, HOMO is responsible for the transport resonance where its energy is much lower than the Fermi level.

Notably, by reversing the potential, the open-shell state can be regained, emphasising the reversible transistor characteristics of junctions formed with compound **1** (Figure 5.12c). The attempt to measure single-molecule conductance of **1** at the cationic (oxidised) was unsuccessful. since the measurement of the molecular conductance at potentials higher than 0.5 V vs Fc/Fc^+ was impossible because of high noise under these conditions. This is assumed to be arise from the cationic species not being soluble in the ionic

liquid, causing it to accumulate at the working electrode, blocking further junction formation.

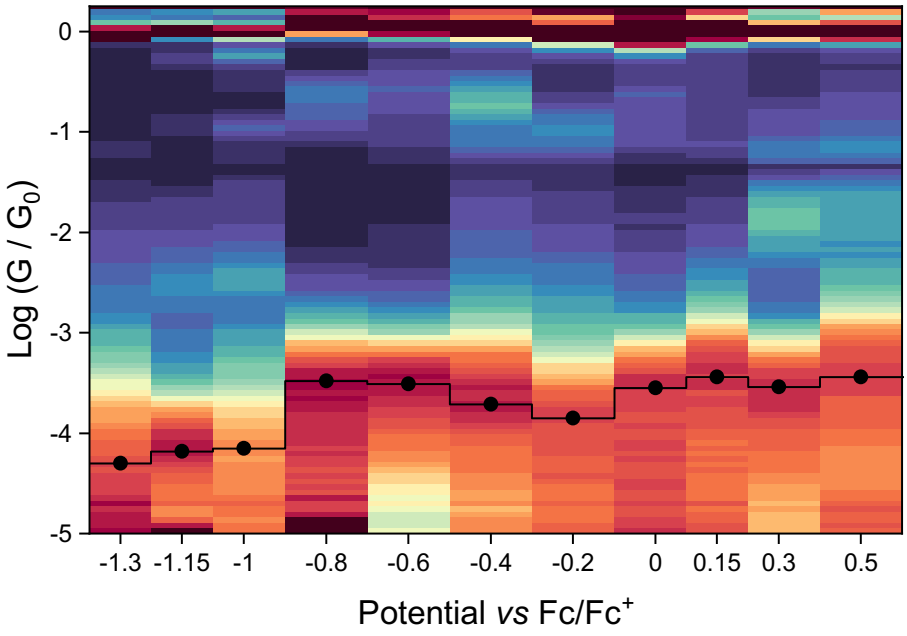

Figure 5.11. The gaussian fit of the peak position is demonstrated in black on a heatmap of single-molecule conductance data all over the investigated electrochemical range. Potential referenced to Fc/Fc^{+}. At each potential point, higher than 2500 individual scans were pilled-up. Legend: blue = low counts; red = high counts. An Au substrate and STM tip were used with a Pt counter-electrode and Ag/AgCl reference electrode in a bipotentiostat setup. STM-break junction was used to make the molecular junction with **1** in the ionic liquid (1-butyl-3-methylimidazolium triflate) electrolyte.

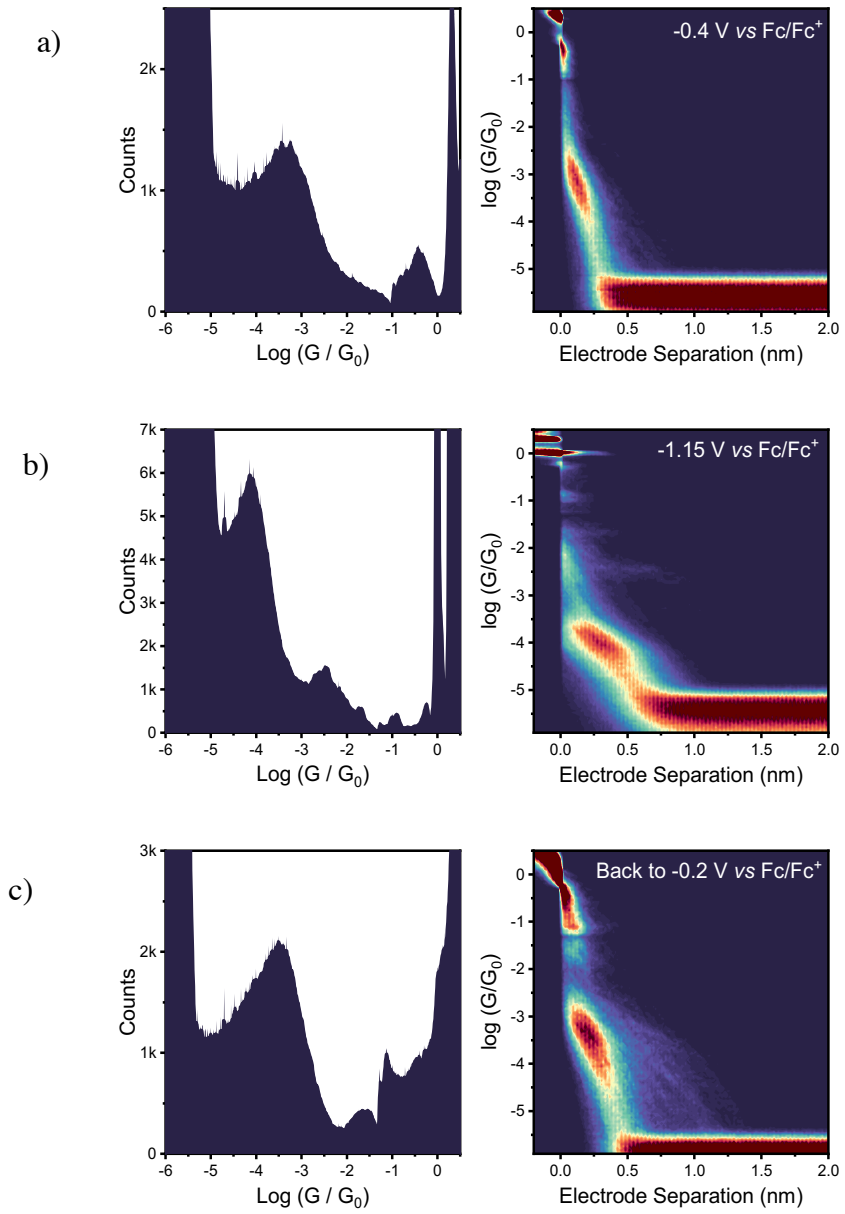

Figure 5.12. STM-Break Junction measurements on compound **1** at 0.2V bias, 1 mM in 1-butyl-methylimidazolium triflate, Pt counter-electrode, Ag/AgCl reference electrode. Measurements were done at -0.4 V potential vs Fc/Fc^+ (open circuit), then the potential was decreased to -1.15 V vs Fc/Fc^+, and then returned to -0.2 V vs Fc/Fc^+. Data obtained from a) 3258, b) 5037, and c) 3160 individual scans. No data selection was used for histograms and 2D density maps compiled, 100 bins / decade, 100 bins / nm.

To summarise these observations, the conductance value in the electrode potential range 0.5 to -0.8 V can be ascribed to transport through the radical

state of **1**, whereas conductance at potentials of -1 V and lower is attributed to the closed-shell anionic state (Figure 5.11). When molecule **1** is in its open-shell form, the conductance rises as the potential is made more negative from -0.2 V to -0.8 V. This suggests that the β-LUSO (the transport resonance) is still at a higher energy level than the electrodes' Fermi level (until the molecule is reduced). The slope of the conductance/potential dependence abruptly switches sign when **1** is reduced. The transport resonance is now the HOMO of the reduced **1**, at a lower energy than the Fermi level.

After showing that the presence of a SOMO improves charge transport through **1**, measuring the single-molecule current-voltage (*I-V*) characteristics of this molecule was done. These data show that the *I-V* behaviours of molecule **1** are not linear (Figure 5.13a). While there is good ohmic behaviour between ±0.7 V, there is rectification at potentials higher than ±1.5 V, with current at negative bias reaching a plateau value of about 25 nA and rapidly rising to values greater than 100 nA at positive bias. There was no rectification or current saturation in the tetrazine **2**, which shows almost symmetrical *I-V* curves (Figure 5.13b).

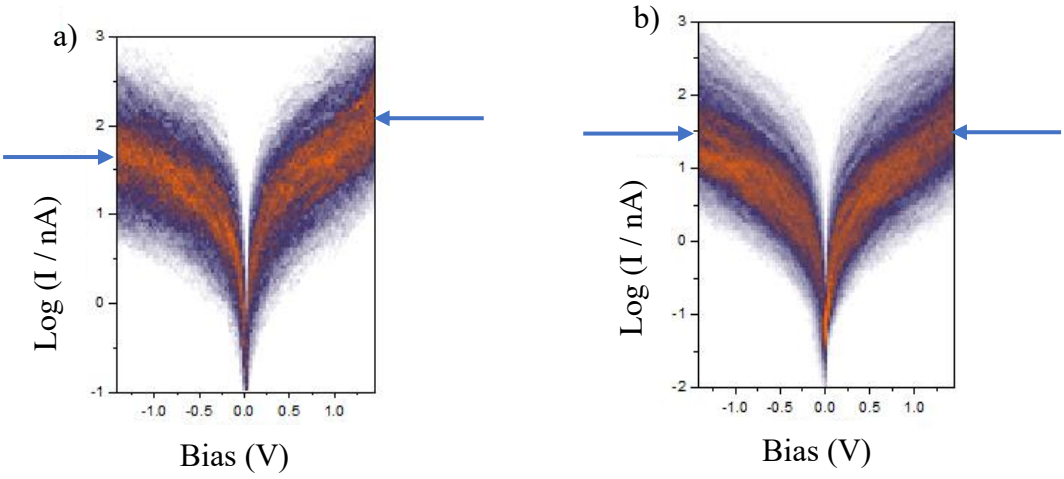

Figure 5.13. Semilogarithmic single-molecule I-V heatmap for a) **1**, and b) **2**. Data compiled from >10000 traces. Heatmap compiled with 20 bins per decade and 50 bins per volt.

This system was studied using bias-dependent DFT computations by the collaborators at the University of Warwick. The bias-dependent calculations show how the transmission spectra are changed by imposition of a bias voltage. Positive bias voltages shift resonances to lower energy values, while when negative bias voltages are applied the shift is towards higher energies.

Figure 5.14 shows a sketch of the relevant orbitals for **1** in a 2-terminal biased electrical junction. The presence of a single occupied energy level in **1** accounts for its enhanced charge transport when compared with **2**. DFT computations of junction transmission for **1** and **2**, are shown in figures 5.15a and 5.15b, respectively. HOMO and LUMO resonance are easily identified in Figure 5.14b for **2**. The transmission curve for **1** is significantly different, with the appearance of SOMO and β-LUSO resonances. The β-LUSO resonance is Figure 5.15a is much closer to the Fermi level than either the HOMO or LUMO resonances in **2** (Figure 5.15b) and this justifies the higher

conductance of **1** and its decrease in conductance when electrochemically reduced.

Figures 5.15a and 5.15b can also be used to understand the rectification seen in **1** but absent in **2**. The *I-V* characteristic of the open-shell **1** exhibits a pronounced asymmetry as seen in Figure 5.13a, while **2** does not (Figure 5.13b). The transmission curve of **2** (Figure 5.15b) shows the Fermi level lying towards the centre of a broad HOMO-LUMO gap in a rather flat region of the transmission curve. Since the Fermi level is near the middle of HOMO-LUMO gap for the closed-shell **2** and the variations in the transmission spectra by applying the bias voltage do not cause significant change in the transmission coefficient at bias values of opposite polarity (Figure 5.15b) while HOMO remains the charge transport orbital, there is consequently no asymmetry in the *I-V* characteristics (Figure 5.13b). This accounts for the lack of rectification for **2**. By contrast, the β-LUSO -SOMO gap in **1** (Figure 5.15a) is much narrower and the Fermi level is aligned to the foot of the β-LUSO resonance. Arrows in Figure 5.15a show how the β-LUSO and SOMO resonances move under applied bias. At positive bias voltages the β-LUSO is responsible of the charge transport for **1**, but the β-LUSO shifts to significant higher energies on moving to negative bias voltages. At the positive bias voltages, the better alignment of the β-LUSO to the Fermi level results in higher junction current values. Although increasing negative bias values do move the SOMO closer to the Fermi level (left arrow in Figure 5.15a) it is never as well aligned with the Fermi level as the β-LUSO is at positive bias values. Using these arguments, the rectifying behaviour of the molecule can

be explained within coherent tunnelling model, without it being attributed to the surrounding environment [204,205], different electronic couplings of the compound to the source and drain electrodes [86,206,207], or asymmetric electrode configurations [86,208].

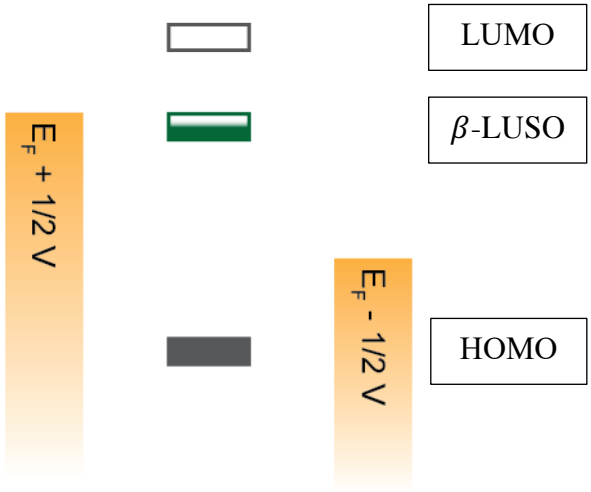

Figure 5.14. An energy level illustration of an open-shell molecule in a molecular junction is shown as an example. The β-LUSO will be aligned with the Fermi energies of the two metal electrodes and will sit in the HOMO-LUMO gap, resulting in greater conductance.

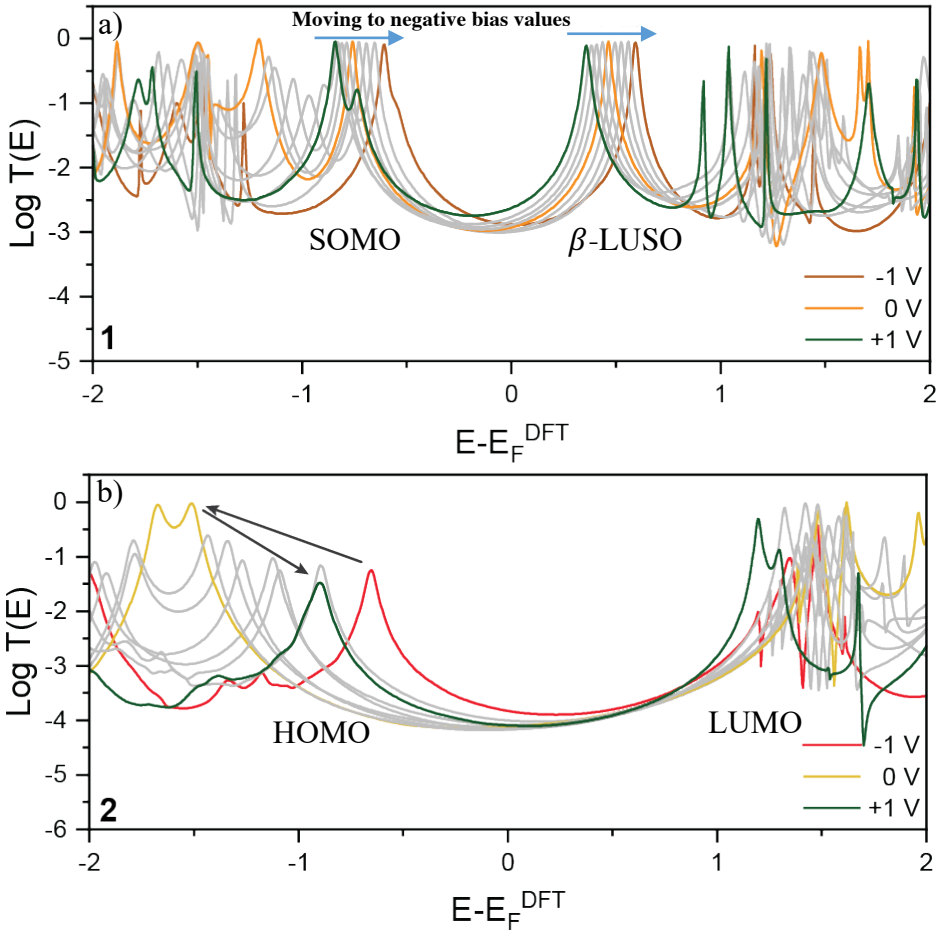

Figure 5.15. (**a**) Calculations of bias-dependent transmission coefficients for Au|**1**|Au junctions. (**b**) Calculations of bias-dependent transmission coefficients for Au|**2**|Au junctions.

To summarise these computational observations, these results show that for molecule **1** the Fermi level lies close to the β-LUSO resonance, while the Fermi level is near the middle of the HOMO-LUMO gap for molecule **2**. Furthermore, the β-LUSO resonance moves closer to the Fermi level upon applying a positive bias voltage in the case of molecule **1**, and as a result, the conductance value increases causing rectification.

5.3. Conclusion

It has been shown that the 6-oxoverdazyl radical **1** preserves its open-shell nature in molecular junctions at ambient temperature. The semi-occupied (SOMO) and unoccupied (β-LUSO) molecular orbitals result to a pair of extra transport resonances due to the open-shell electronic nature of compound **1**. This pair of extra transport resonances that are generated by the semi-occupied molecular orbital in its open-shell configuration, allow **1** to achieve a considerable increase in charge-transport efficiency when compared to its closed-shell counterpart **2**. The additional transport resonances are located in an energy region close enough to the Fermi level so that they can influence junction current at higher positive bias, resulting in a pronounced rectifying behaviour in single-molecule junctions fabricated with **1**. This is accompanied by relatively lower current values at large negative biases in single-molecule junctions fabricated with **1**. In addition, by using electrochemical potential control, it was possible to reversibly convert compound **1** to a closed-shell anion. Characterisation of its charge-transport behaviour in the two different charge states has been shown.

These findings demonstrate a new approach involving the incorporation of stable radicals in single-molecule devices and transistor behaviour of these molecules in the junction. This study opens a new window on molecular electronic studies of stable radicals at room temperature. This could have future impact in the development of new technologies such as molecular spintronics and molecular thermoelectrics.

CHAPTER 6

CONCLUSIONS

The main focus of this thesis has been on studying and controlling the molecular electronic properties of various compounds using different molecular systems. Single-molecule junctions made of metal-molecule-metal have been formed using scanning tunnelling microscopy techniques.

In Chapter 3, the study of N-substituted pyrrolodipyridines demonstrates that changing the substituents and the position of the gold electrode contact to the molecular bridge (the connectivity) makes it possible to chemically modulate conductance. Quantum interference (QI) is caused by meta connection, but it can be turned off in a series of meta- pyrrolodipyridines by changing the substitution on the pyrrolodipyridine's N atom. Since the coupling of the lone pair of the N and the aromatic framework of the pyrrolodipyridine is adjusted by changing the electron density, the conductance of the compounds in the molecular junction can be tuned. This QI effect resulting from meta connection competes with an alternative, high-conductance pathway involving a single atom (pyrrolic N), whose electron density in meta-pyrrolodipyridines can be altered by chemical replacement. The quantum interference that reduces conductance as a result of the meta-connectivity trend can be adjusted simply by substitution on a single nitrogen atom in the conductance path.

In Chapter 4, the intermolecular and intramolecular charge-transport properties of single-molecule and stacked junctions were investigated. A lower conductance value for the stacked dimer junction was seen by comparing through-bond tunnelling in the single-molecule junction with charge transfer across stacked dimers. The solvent shell around the molecular

wire could prevent the molecule from forming stacked dimers. In contrast, measurements under ambient atmosphere conditions revealed that the stacked junction contributed primarily to the conductance histogram with a lower conductance compared to the single-molecule junction. The effect of electrical coupling on single-molecule junctions and its influence on the flicker noise-conductance relationship were discussed. This allows to distinguish between coupling through-bond versus through space coupling.

In Chapter 5, it has shown that at room temperature, the 6-oxoverdazyl maintains its open-shell structure at molecular junctions. Because of the open-shell electronic structure of radicals, the semi-occupied (SOMO) and unoccupied (β-LUSO) molecular orbitals result in a pair of extra transport resonances. When compared to its closed-shell counterpart, the radical can achieve a significant boost in charge-transport efficiency because of the extra transport resonances generated by the semi-occupied molecular orbital in this open-shell configuration. In single-molecule junctions produced with the radical, the extra transport resonances are placed in an energy band close enough to the Fermi level which influences the junction current at higher positive bias, resulting in strong rectifying behaviour. This is accompanied by relatively lower current values at large negative biases in single-molecule junctions fabricated with the radical. Furthermore, reversibly converting a radical molecule to a closed-shell anion via electrochemical potential control was possible. Characterisation of the charge-transport behaviour of the radical molecule in both charge states was shown.

Although there are still many obstacles to practically using single molecules in electrical circuits, this study makes a contribution in that challenging and futuristic direction. However, the greatest contribution of this thesis, and single molecular electronics in general, is towards the further understating of charge transport through molecular structures and junctions and in establishing structure-property relationships.

A number of further experiments are necessary to thoroughly determine the characteristics of the molecules and phenomenon described in this thesis. Especially further single molecular measurements, characterisations are required for Chapter 4. It is intended that this study will serve as a foundation and source of inspiration for future research. It is believed that further interesting discoveries will be made along the way to developing molecular electronic applications.

CHAPTER 7

APPENDICES

7.1. Supplementary Information for Chapter **3**

7.1.1. Conductance Histograms of Meta and Para Pyrrolodipyridines

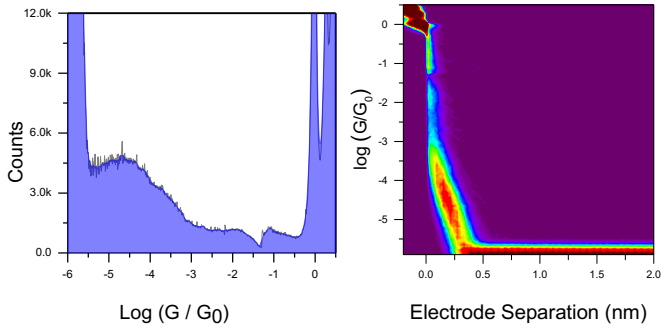

Figure 7.1. STM-BJ measurements on **1M**. 0.2V bias, 1 mM in mesitylene and THF (7:3 v/v). Histogram and 2D density map compiled from 5136 individual scans, no data selection, 100 bins / decade, 100 bins / nm.

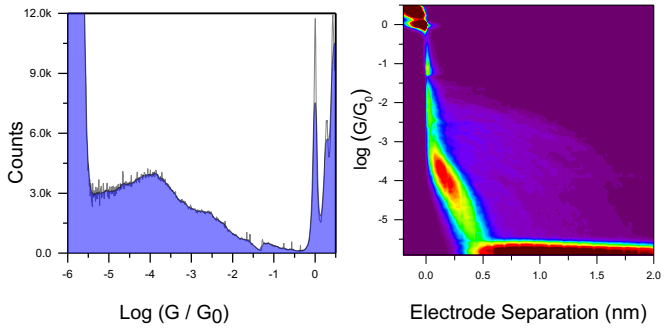

Figure 7.2. STM-BJ measurements on **2M**. 0.2V bias, 1 mM in mesitylene and THF (7:3 v/v). Histogram and 2D density map compiled from 3898 individual scans, no data selection, 100 bins / decade, 100 bins / nm.

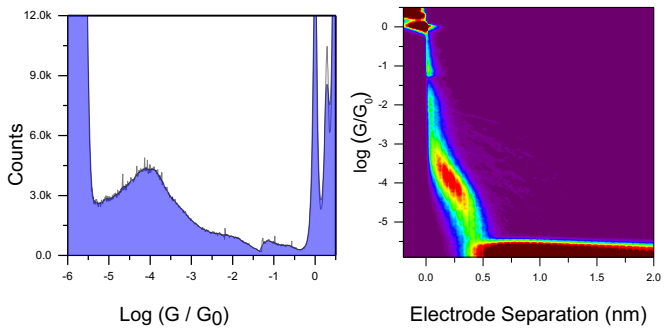

Figure 7.3. STM-BJ measurements on **3M**. 0.2V bias, 1 mM in mesitylene and THF (7:3 v/v). Histogram and 2D density map compiled from 5016 individual scans, no data selection, 100 bins / decade, 100 bins / nm.

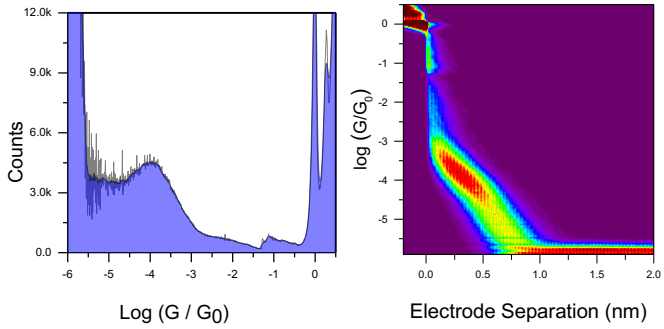

Figure 7.4. STM-BJ measurements on **4M**. 0.2V bias, 1 mM in mesitylene and THF (7:3 v/v). Histogram and 2D density map compiled from 5257 individual scans, no data selection, 100 bins / decade, 100 bins / nm.

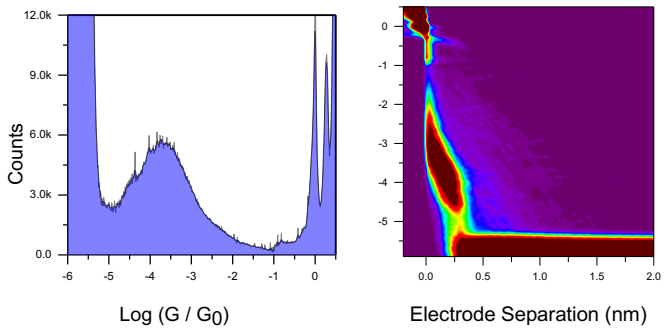

Figure 7.5. STM-BJ measurements on **5M**. 0.2V bias, 1 mM in mesitylene and THF (7:3 v/v). Histogram and 2D density map compiled from 4721 individual scans, no data selection, 100 bins / decade, 100 bins / nm.

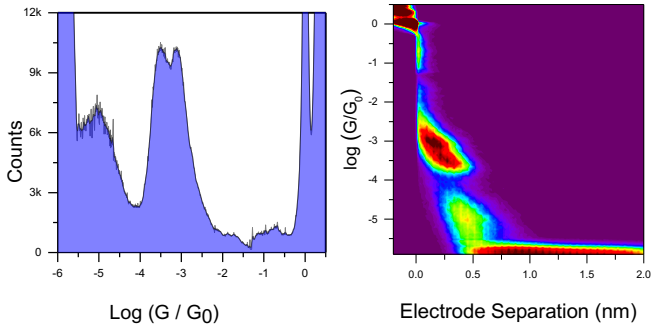

Figure 7.6. STM-BJ measurements on **1P**. 0.2V bias, 1 mM in mesitylene and THF (7:3 v/v). Histogram and 2D density map compiled from 5382 individual scans, no data selection, 100 bins / decade, 100 bins / nm.

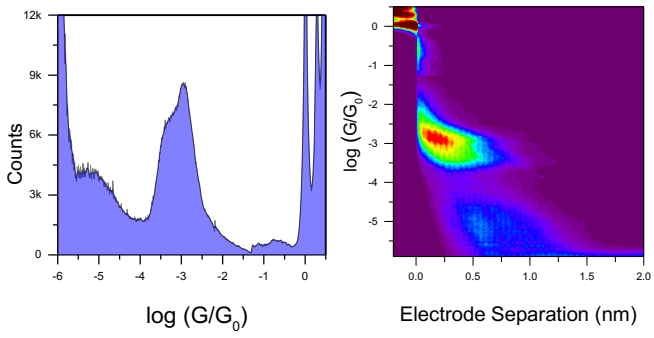

Figure 7.7. STM-BJ measurements on **2P**. 0.2V bias, 1 mM in mesitylene and THF (7:3 v/v). Histogram and 2D density map compiled from 4936 individual scans, no data selection, 100 bins / decade, 100 bins / nm.

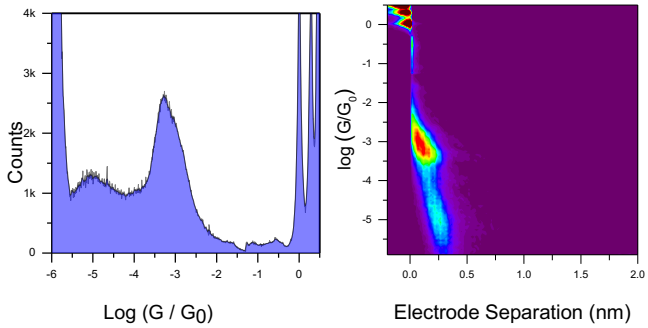

Figure 7.8. STM-BJ measurements on **5P**. 0.2V bias, 1 mM in mesitylene and THF (7:3 v/v). Histogram and 2D density map compiled from 5137 individual scans, no data selection, 100 bins / decade, 100 bins / nm.

For the meta and para-compounds, the experimental break-off distance of about 3-4 Å (end of the high-count region in the 2D density maps) is compatible with molecular length when accounting for an electrode "snap-back" of around 6 Å [209].

7.1.2. UV-Vis Characterisation of Meta and Para Pyrrolodipyridines

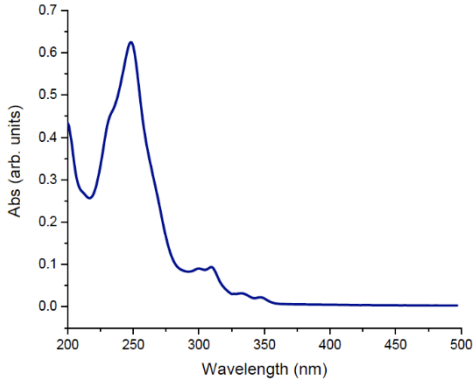

Figure 7.9. UV-Vis spectrum of compound **1M** in dry acetonitrile.

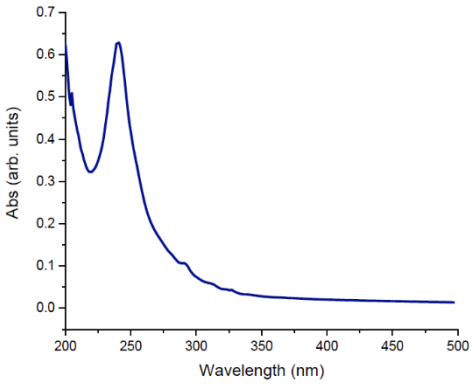

Figure 7.10. UV-Vis spectrum of compound **2M** in dry acetonitrile.

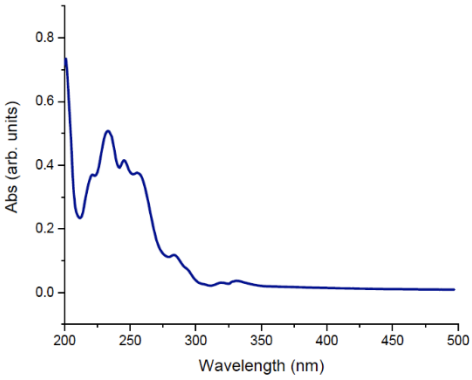

Figure 7.11. UV-Vis spectrum of compound **3M** in dry acetonitrile.

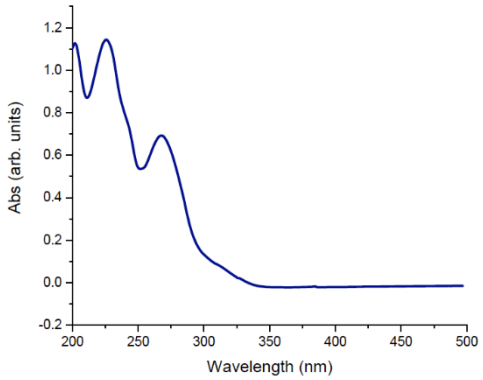

Figure 7.12. UV-Vis spectrum of compound **4M** in dry acetonitrile.

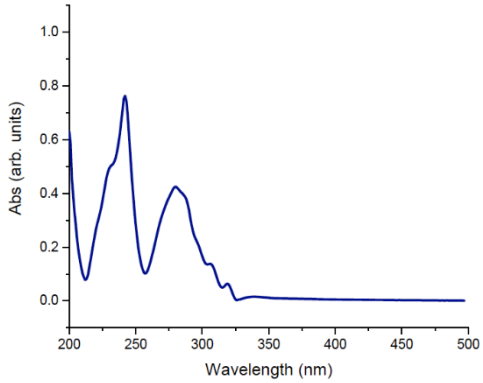

Figure 7.13. UV-Vis spectrum of compound **5M** in dry acetonitrile.

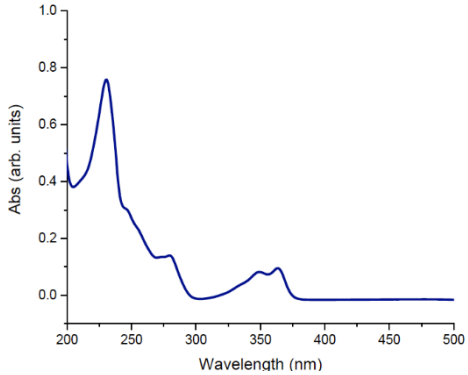

Figure 7.14. UV-Vis spectrum of compound **1P** in dry acetonitrile.

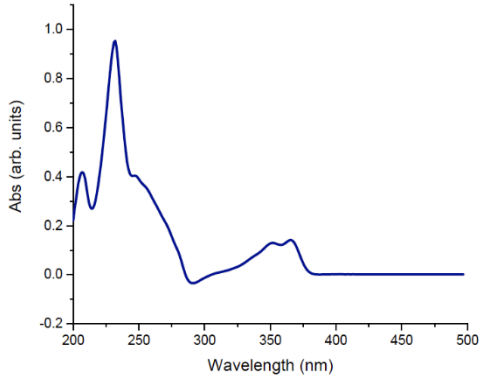

Figure 7.15. UV-Vis spectrum of compound **2P** in dry acetonitrile.

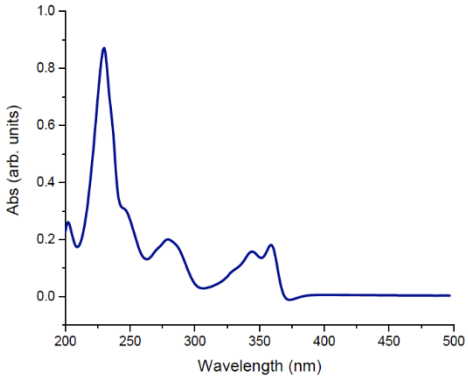

Figure 7.16. UV-Vis spectrum of compound **5P** in dry acetonitrile.

7.1.3. NMR Characterisation of Meta and Para Pyrrolodipyridines

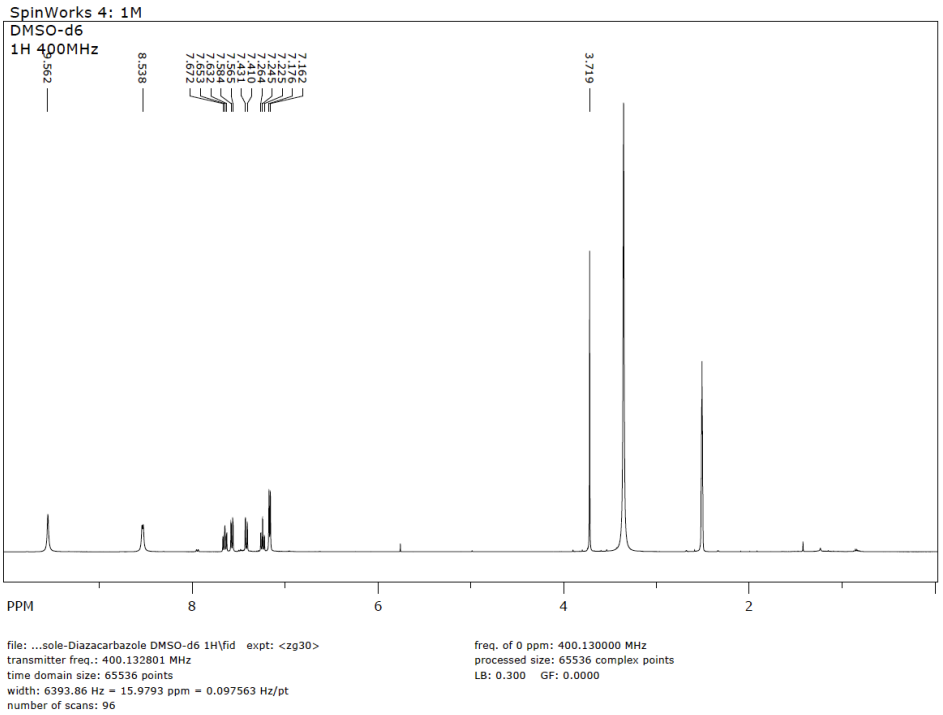

Figure 7.17. Proton NMR spectrum for compound **1M**. Residual solvent peaks: 2.50 ppm = DMSO; 3.33 ppm = H_2O; 5.76 = CH_2Cl

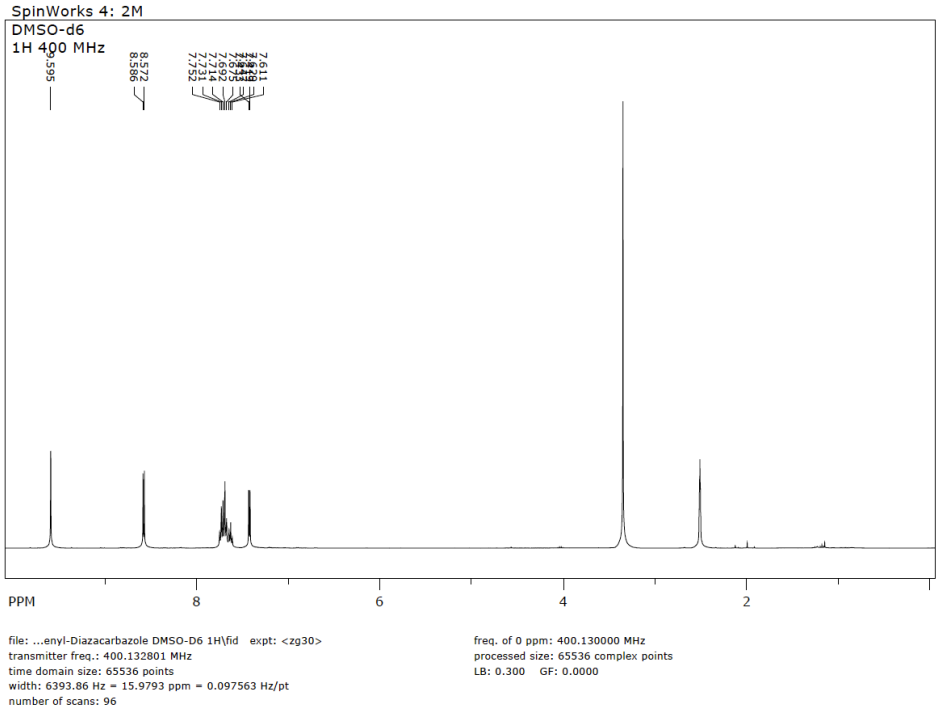

Figure 7.18. Proton NMR spectrum for compound **2M**. Residual solvent peaks: 2.50 ppm = DMSO; 3.33 ppm = H_2O.

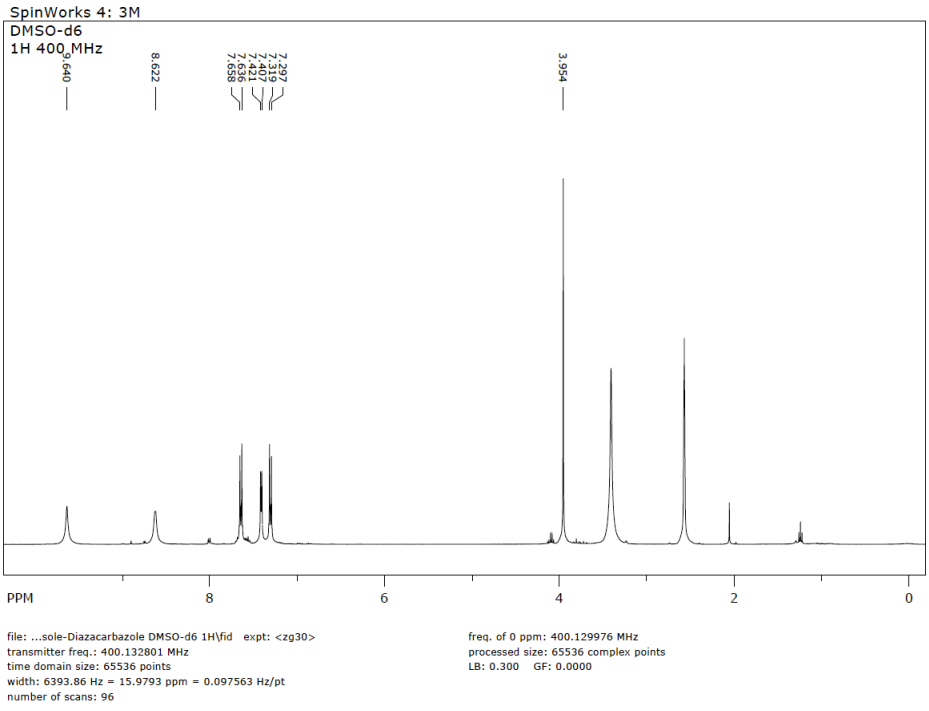

Figure 7.19. Proton NMR spectrum for compound **3M**. Residual solvent peaks: 1.25 ppm = petroleum ether; 2.09 ppm = acetone; 2.50 ppm = DMSO; 3.33 ppm = H_2O

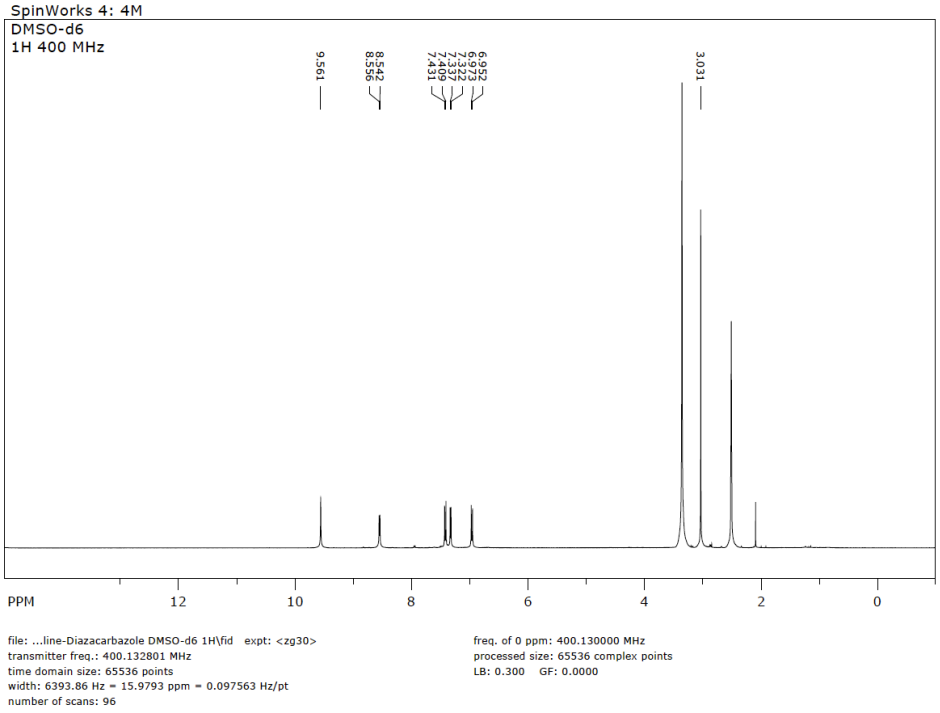

Figure 7.20. Proton NMR spectrum for compound **4M**. Residual solvent peaks: 2.09 ppm = acetone; 2.50 ppm = DMSO; 3.33 ppm = H_2O.

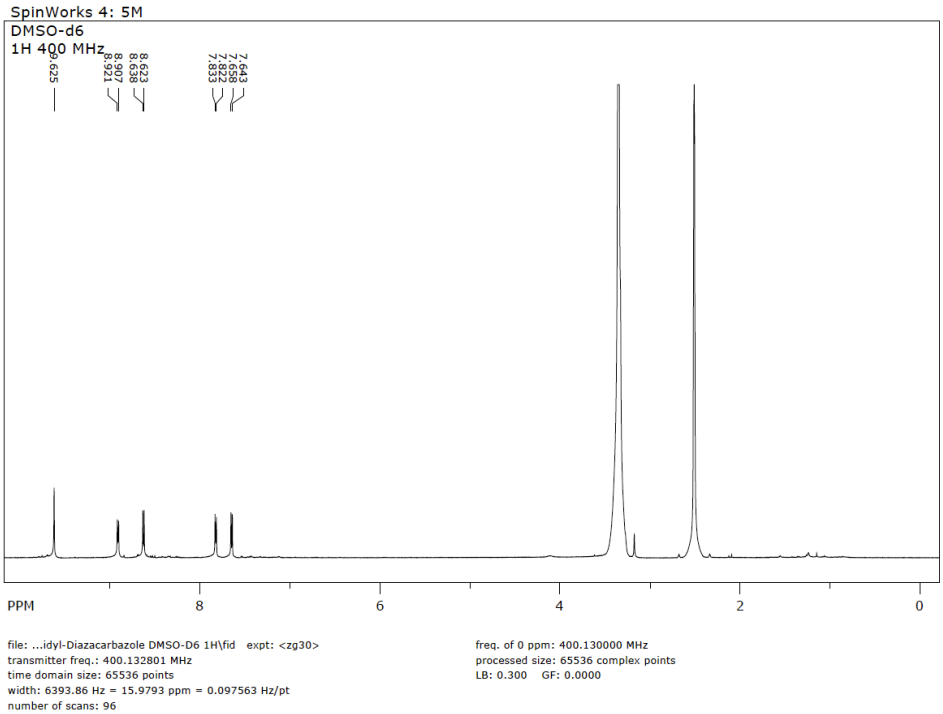

Figure 7.21. Proton NMR spectrum for compound **5M**. Residual solvent peaks: 2.50 ppm = DMSO; 3.33 ppm = H_2O.

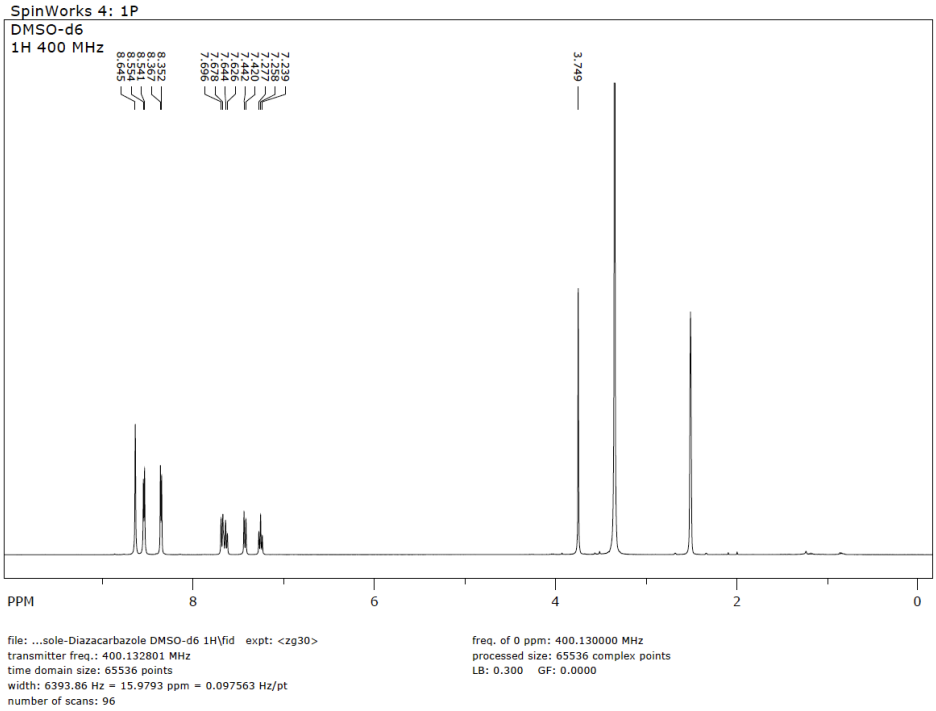

Figure 7.22. Proton NMR spectrum for compound **1P**. Residual solvent peaks: 2.50 ppm = DMSO; 3.33 ppm = H_2O.

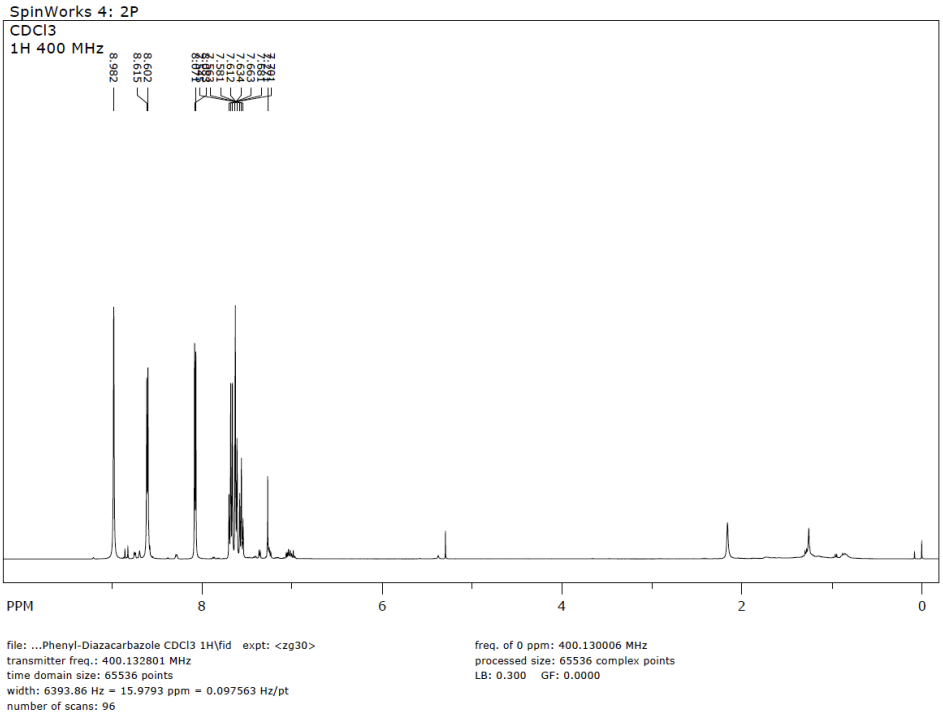

Figure 7.23. Proton NMR spectrum for compound **2P**. Residual solvent peaks: 1.56 = H_2O; 2.16 = acetone; 5.31 = CH_2Cl_2; 7.26 ppm: $CHCl_3$.

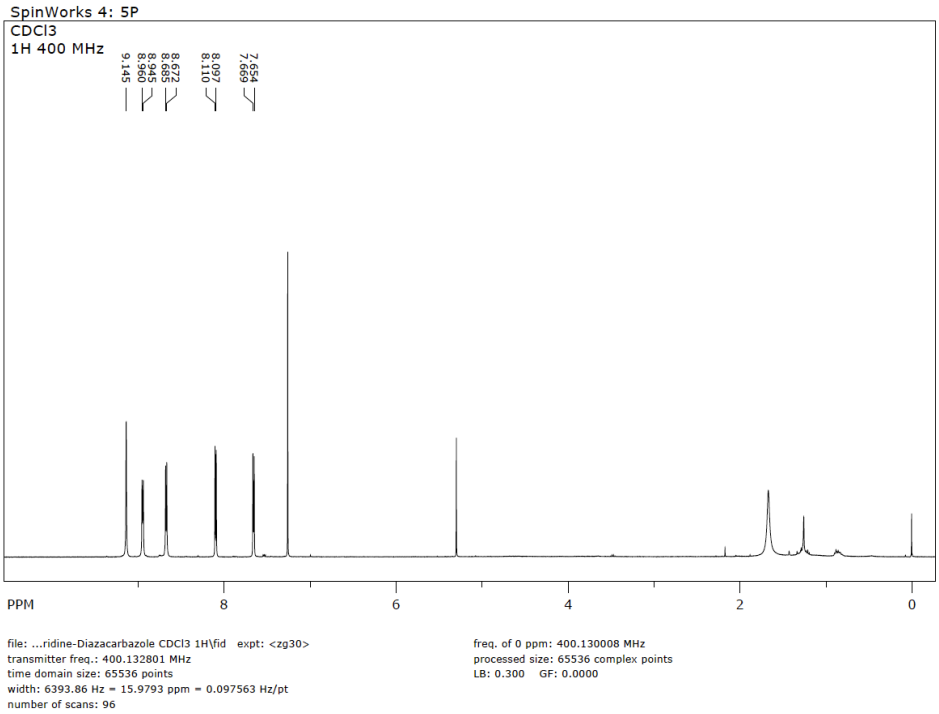

Figure 7.24. Proton NMR spectrum for compound **5P**. Residual solvent peaks: 0.88 – 1.25 = n-hexane; 1.56 = H_2O; 2.16 = acetone; 5.31 = CH_2Cl_2; 7.26 ppm: $CHCl_3$.

7.2. Supplementary Information for Chapter 4

7.2.1. AFM and NMR Characterisations of the Pillararenes

The SAM of guest compounds was investigated by AFM in order to determine the thickness variation of films of the host -guest the complexes on flat gold electrodes. These measurements were made by the collaborators in Zaragoza. The thickness of complex **2⊂4** in SAM surface films on flat gold substrates, as determined by AFM scratching experiments, was 1.8 nm. These studies demonstrated that compound **2** had a propensity to self-assemble on surfaces, resulting in an ordered monolayer, likely produced by off-centre parallel stacking between pillar[5]arenes [210], Figure 6.9.

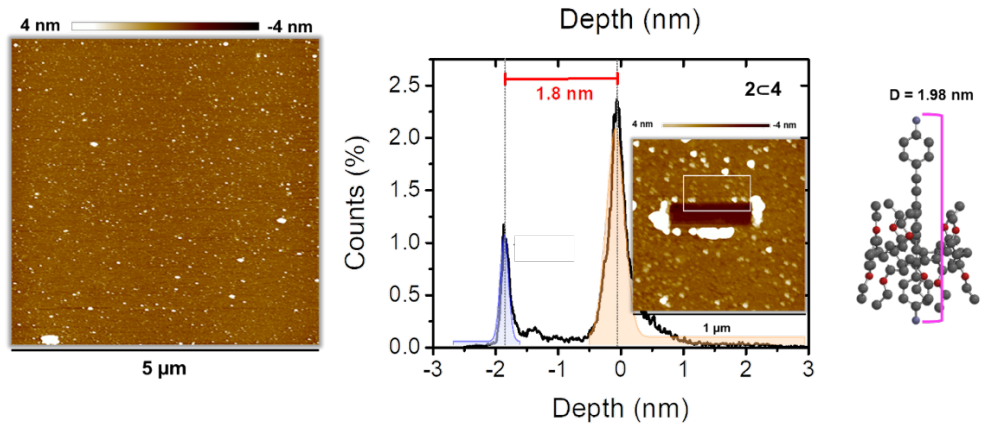

Figure 7.25. AFM image of a SAM of complex **2⊂4** and depth profile obtained from a scratched area.

The formation of complex **2⊂4** was studied by H-NMR. By looking at H-NMR results of complex **2⊂4,** a chemical shift to downfield is detected at *l*, *m*, *j* and *i* protons of compound **2**. The meaningful variation was appreciated for the signal associated to the amines, moving from ca. 3.8 ppm to 1.5 ppm once the complex is formed. For compound **4** spectrum, amine protons appear at 3.83 ppm. This signal moves to ca. 1.50 ppm when complexed at the pillararene cavity. To ensure that this peak corresponds to the amines, 0.5 mL of D_2O were added to the NMR tube, giving place to deuterium-amines exchange.

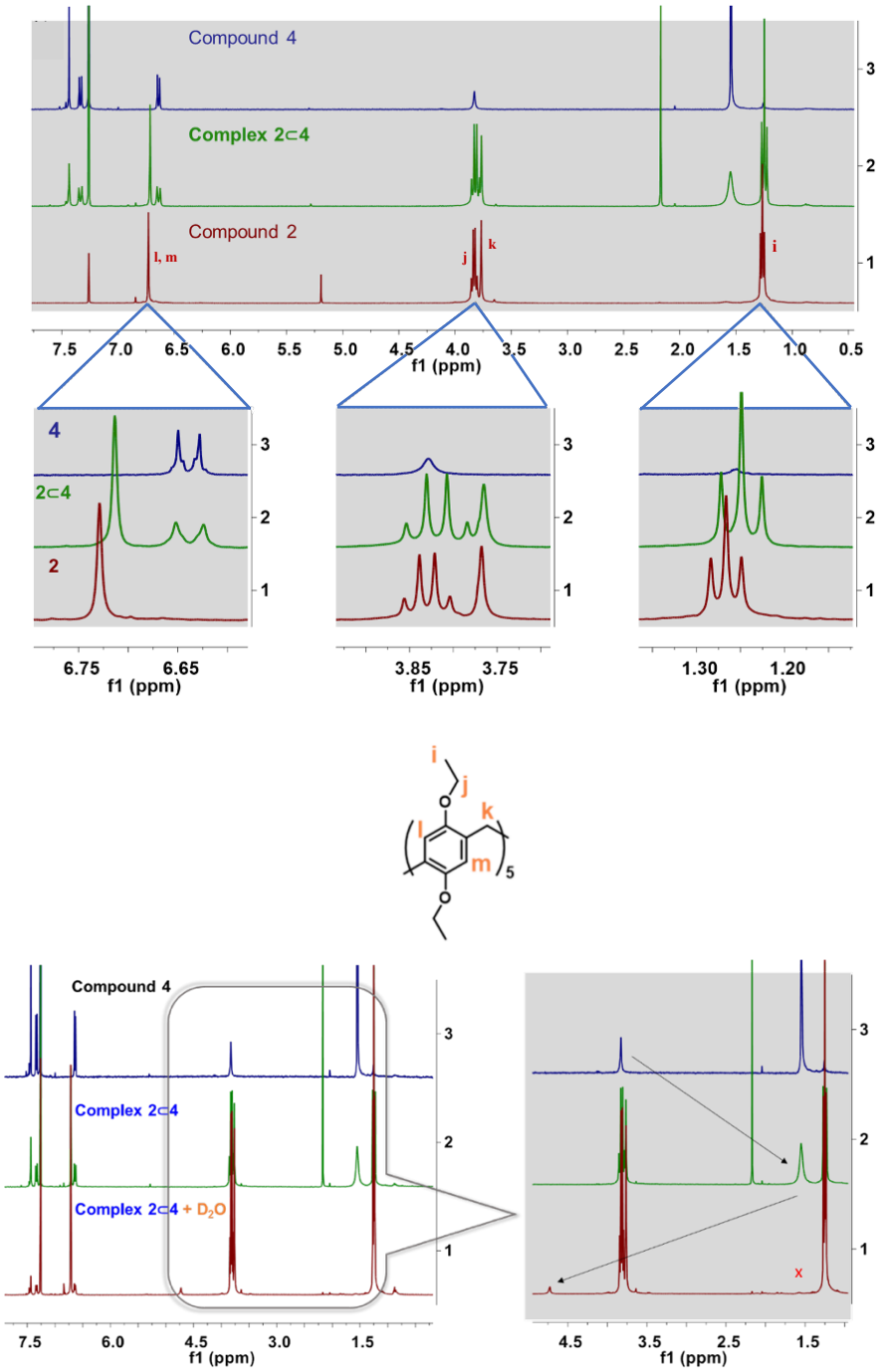

Figure 7.26. H-NMR of compounds, **4** and complex **2⊂4** (DMSO-d6 and D_2O). The spectra on the top show the shift in the position of proton peaks of 2 before and after complexation. The bottom spectra show the shift in the position of proton peaks of amines in 4 before and after complexation and after adding D_2O.

7.2.2. Molecular Electronic Study of **4** (OPE Lead)

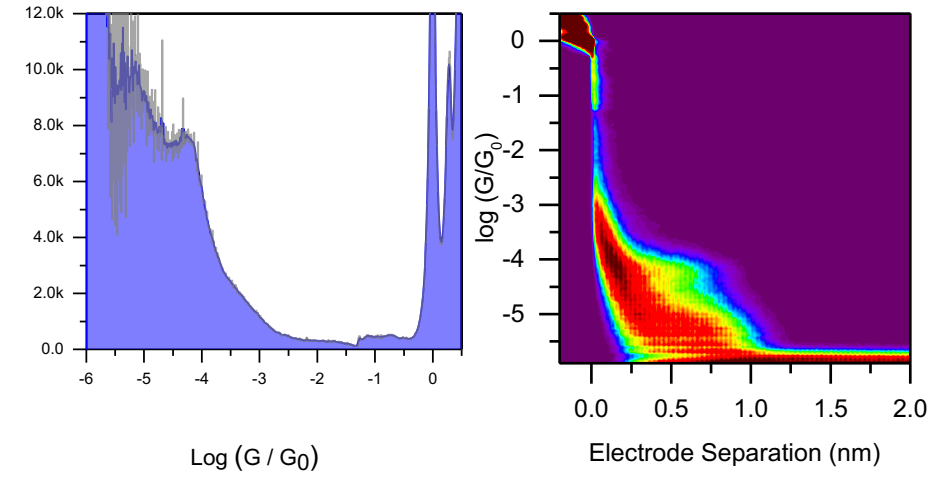

Figure 7.27. STM-BJ measurements on 4. 0.2 V bias, 1 mM solution of 4 in acetone. Measured under atmospheric conditions. Histogram and 2D density map compiled from 5523 individual scans, no data selection, 100 bins / decade, 100 bins / nm.

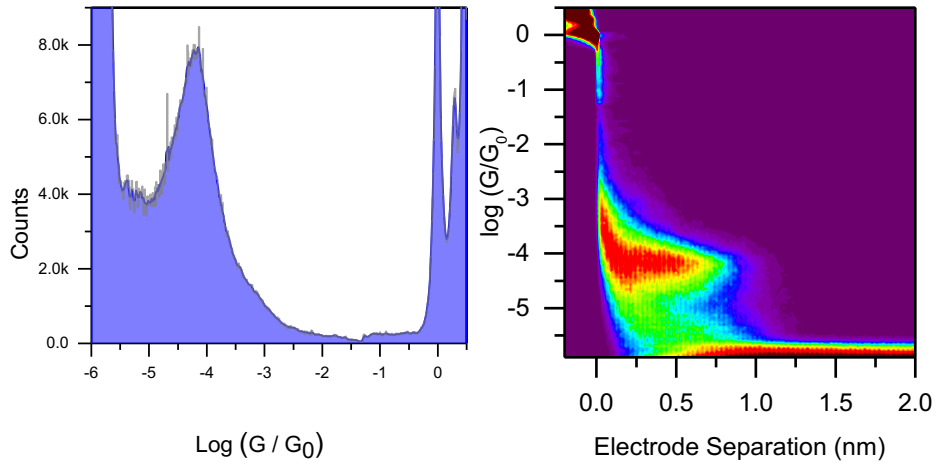

Figure 7.28. STM-BJ measurements on 4. 0.2 V bias, 1 mM in mesitylene and THF (4:1 v/v). Histogram and 2D density map compiled from 3936 individual scans, no data selection, 100 bins / decade, 100 bins / nm.

7.2.3. Molecular Electronic Study of **2⊂4** (Pillararene-OPE) Complex

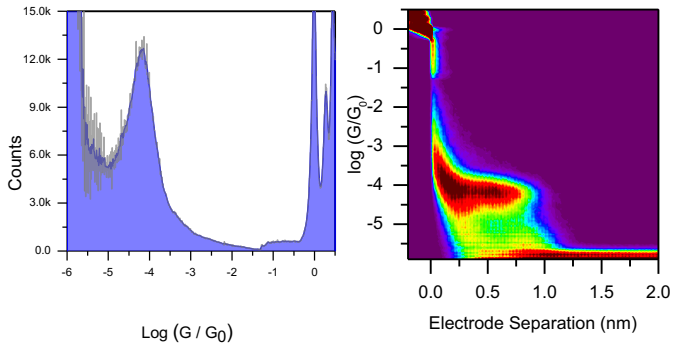

Figure 7.29. STM-BJ measurements on **2⊂4**. 0.2V bias, 1 mM under atmospheric conditions. Histogram and 2D density map compiled from 3597 individual scans, no data selection, 100 bins / decade, 100 bins / nm.

7.2.4. Molecular Electronic Study of 1⊂4 (Pillararene-OPE) Complex

To measure the conductance of compound **1⊂4**, the same STM-BJ approach as **2⊂4** measurements was utilised. In contrast to compound **2**, pillararene with amine termini can interact with metallic electrodes. After complexation, the interaction of compound **1** (Figure 7.14) interfered with the molecular electronic measurements of molecule 4. Consequently, the data for **1⊂4** were not as firm as those for the **2⊂4** complex and working on it was ceased (Figure 7.15).

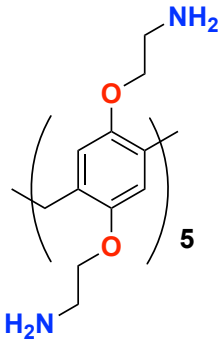

Figure 7.30. Chemical structure of compounds **1.**

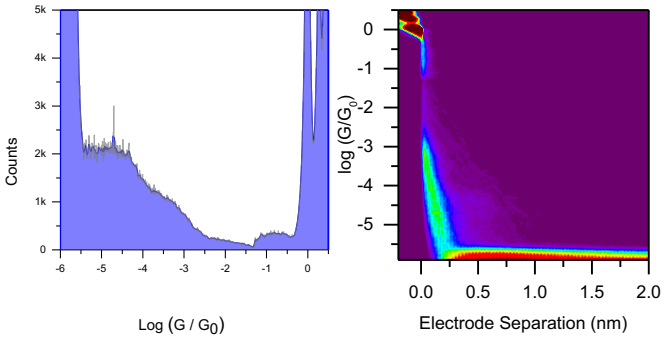

Figure 7.31. STM-BJ measurements on **1⊂4**. 0.2V bias, 1 mM under atmospheric conditions. Histogram and 2D density map compiled from 3838 individual scans, no data selection, 100 bins / decade, 100 bins / nm.

7.3. Supplementary Information for Chapter 5

7.3.1. Molecular Electronic Study of **1** and **2** in the Air

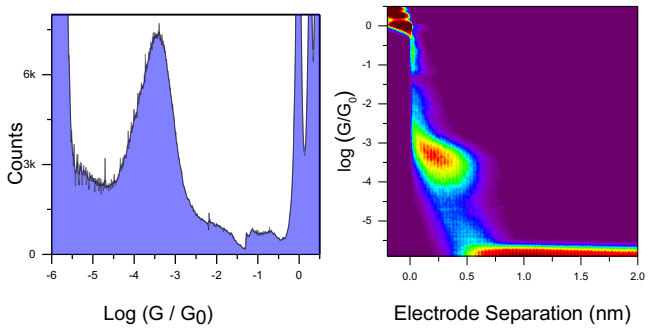

Figure 7.32. STM-BJ measurements on **1**. 0.2V bias, pre-adsorbed from a 1 mM acetone solution and measured under atmospheric conditions. Histogram and 2D density map compiled from 6672 individual scans, no data selection, 100 bins / decade, 100 bins / nm.

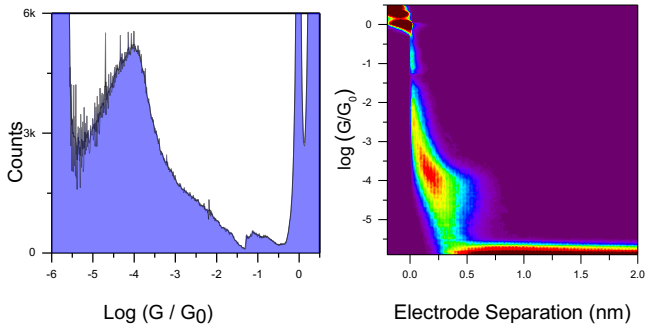

Figure 7.33. STM-BJ measurements on 2. 0.2V bias, pre-adsorbed from a 1 mM acetone solution and measured under atmospheric conditions. Histogram and 2D density map compiled from 6672 individual scans, no data selection, 100 bins / decade, 100 bins / nm.

7.3.2. 2D Histograms of **1** at Different Potentials

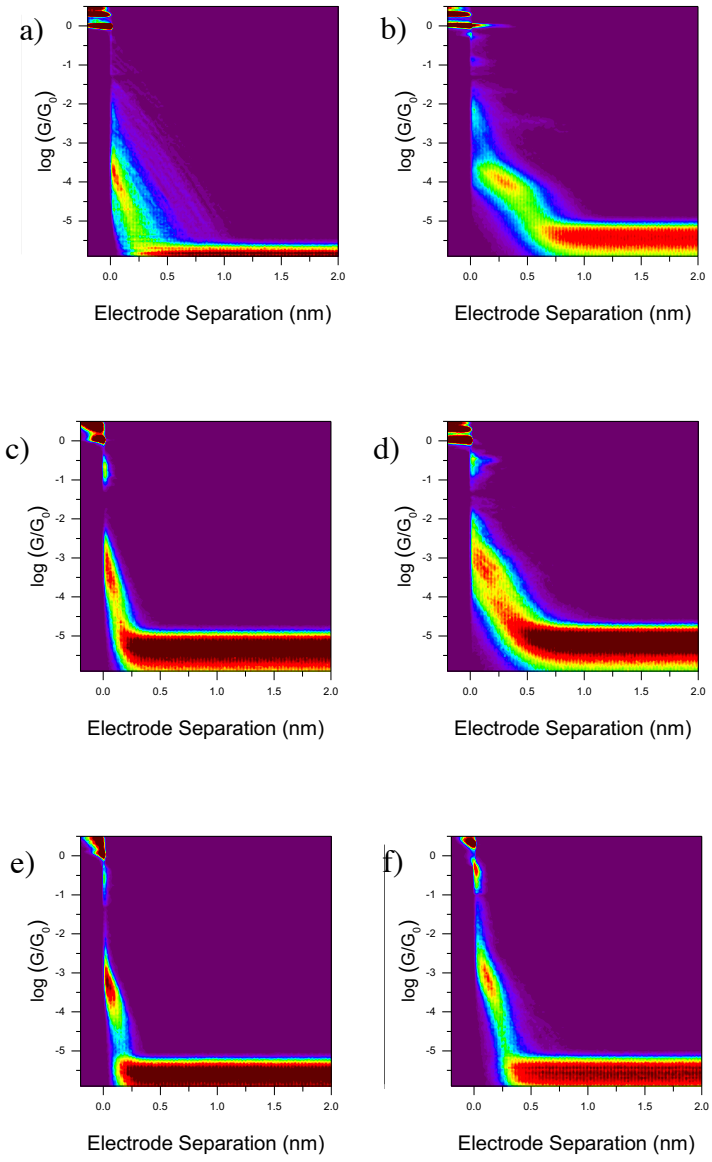

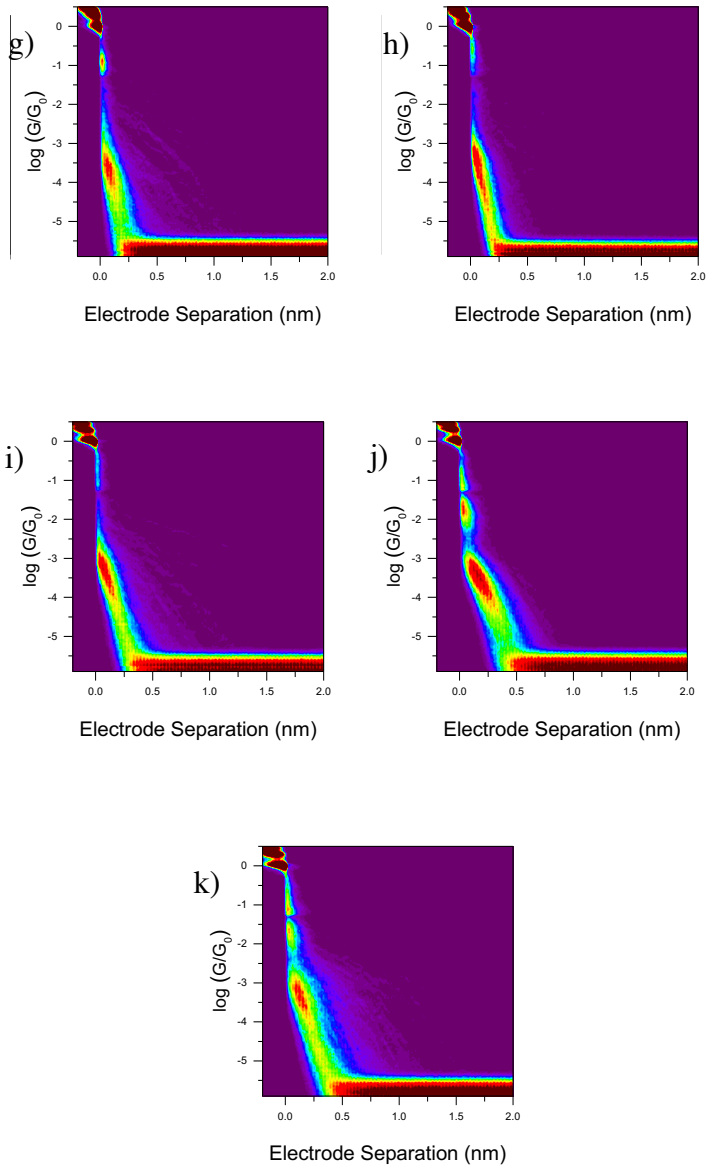

Figure 7.34. 2D conductance histogram of **1** at a) -1.3 V, b) -1.15 V, c) -1 V, d) -0.8 V, e) -0.6 V, f) -0.4 V, g) -0.2 V, h) 0 V, i) 0.1 V, j) 0.3 V, and k) 0.5 V. Potential referenced to Fc/Fc^{+}. More than 2500 individual scans were collected at each potential. To apply a voltage between the STM Au substrate and tip and a Pt counter-electrode against an Ag/AgCl reference electrode a bipotentiostat was used. STM-break junction was used to make the molecular junction with **1** in the ionic liquid (1-butyl-3-methylimidazolium triflate) electrolyte.

7.3.3. UV-Vis Characterisation of **1** and **2**

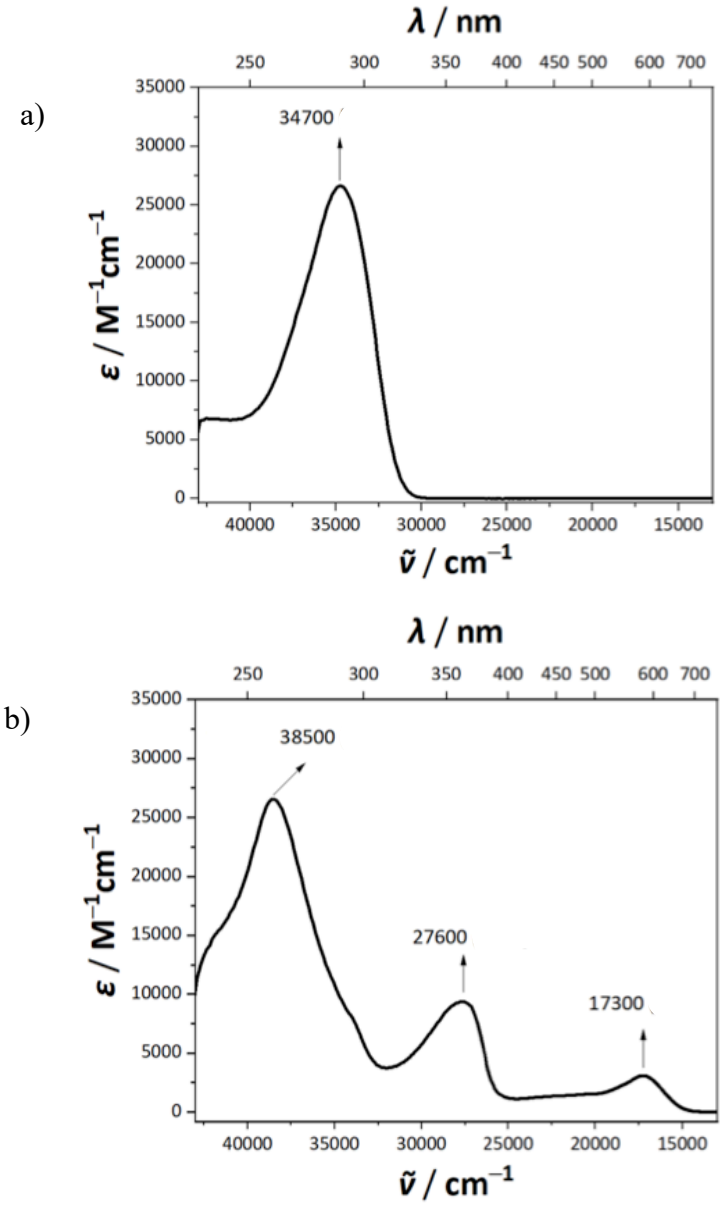

Figure 7.35. UV-Vis spectra of **1** and **2**. a) The peak at 38500 cm^{-1} is related to maximum photon absorption of **1**. b) The peak at 38500 cm^{-1} is related to $\pi\ to\ \pi^*$, at 27600 cm^{-1} is related to $\propto -HUMO\ to\ \propto (LUMO + 1)$ excitation, and at 17300 cm^{-1} is related to $\beta - HOMO\ to\ \beta - LUMO$ excitation of **2**. The UV-Vis characterisation of **1** and **2** were done by our collaborators at the University of Western Australia. The data is presented by the permission of authors.

Bibliography

(1) Xin, N.; Guan, J.; Zhou, C.; Chen, X.; Gu, C.; Li, Y.; Ratner, M. A.; Nitzan, A.; Stoddart, J. F.; Guo, X. Concepts in the Design and Engineering of Single-Molecule Electronic Devices. *Nat Rev Phys.* **2019**, *1* (3), 211–230.

(2) Michael C. Petty. Organic and Molecular Electronics: From Principles to Practice, Second. *Wiley*. **2018**, 13-15.

(3) Zhou, Y.; Han, S.-T.; Roy, V. A. L. Nanocrystalline Materials. *Elsevier*. **2014**, 195–220.

(4) Fuller, C. W.; Padayatti, P. S.; Abderrahim, H.; Adamiak, L.; Alagar, N.; Ananthapadmanabhan, N.; Baek, J.; Chinni, S.; Choi, C.; Delaney, K. J.; Dubielzig, R.; Frkanec, J.; Garcia, C.; Gardner, C.; Gebhardt, D.; Geiser, T.; Gutierrez, Z.; Hall, D. A.; Hodges, A. P.; Hou, G.; Jain, S.; Jones, T.; Lobaton, R.; Majzik, Z.; Marte, A.; Mohan, P.; Mola, P.; Mudondo, P.; Mullinix, J.; Nguyen, T.; Ollinger, F.; Orr, S.; Ouyang, Y.; Pan, P.; Park, N.; Porras, D.; Prabhu, K.; Reese, C.; Ruel, T.; Sauerbrey, T.; Sawyer, J. R.; Sinha, P.; Tu, J.; Venkatesh, A. G.; VijayKumar, S.; Zheng, L.; Jin, S.; Tour, J. M.; Church, G. M.; Mola, P. W. Merriman, B. Molecular Electronics Sensors on a Scalable Semiconductor Chip: A Platform for Single-Molecule Measurement of Binding Kinetics and Enzyme Activity. *PNAS.* **2022**, *119*, 1-12.

(5) Riaz, K. N.; Israr, Z.; Awan, T. I.; Bashir, A.; Tehseen, A. Molecular Electronics. Chemistry of Nanomaterials. *Elsevier*. **2020**, 207–223.

(6) Fan, Y.; Barlow, S. T.; Zhang, B. Single-Molecule Electrochemistry. *Elsevier*. **2021**, 18, 253–293.

(7) Petrangolini, P.; Alessandrini, A.; Facci, P. Hydroquinone-Benzoquinone Redox Couple as a Versatile Element for Molecular Electronics. *J. Phy. Chem. C.* **2013**, *117*, 17451–17461.

(8) Moth-Poulsen, K.; Bjørnholm, T. Molecular Electronics with Single Molecules in Solid-State Devices. *Nat Nanotechnol.* **2009**, *4*, 551–556.

(9) Mann, B.; Kuhn, H. Tunneling through Fatty Acid Salt Monolayers. *J. App. Phys.* **1971**, *42*, 4398–4405.

(10) Ogoshi, T.; Yamagishi, T. A. CHAPTER 1: Historical Background of Macrocyclic Compounds. Monographs in Supramolecular Chemistry. *RSC*. **2016**, 1, 1–22.

(11) Arieh Aviram. Molecular Rectifiers. *Chem Phys. Lett.* **1974**, *29*, 277–283.

(12) Reed, M. A.; Zhou, C.; Muller, C. J.; Burgin, T. P.; Tour, J. M. Conductance of a Molecular Junction. *Science*. **1997**, 278, 252-254.

(13) Aviram, A.; Joachim, C.; Pomerantz, M. EVIDENCE OF SWITCHING AND RECTIFICATION BY A SINGLE MOLECULE EFFECTED WITH A SCANNING TUNNELING MICROSCOPE. *Chem. Phys. Lett.* **1988**, 146, 490-495.

(14) Kim, Y. T.; McCarley, R. L.; Bard, A. J. Scanning Tunnelling Microscopy study of gold(111) derivatized with organothiols. *J. Phys. Chem.* 1992, 96, 7416-7421.

(15) Hayes, D.; Griffin, G. B.; Engel, G. S. Engineering Coherence among Excited States in Synthetic Heterodimer Systems. *Science.* **2013**, *340*,1431–1434.

(16) Peter Atkins, J. D. P. Physical Chemistry. **2009**, 123-143.

(17) Zhao, A.; Tan, S.; Li, B.; Wang, B.; Yang, J.; Hou, J. G. STM Tip-Assisted Single Molecule Chemistry. *Phys. Chem. Chem. Phys*. **2013**, 30, 12428–12441.

(18) Binnig, G.; Rohrer, H.; Gerber, C.; Weibel, E. Real space observation of the 2x1 structure of chemisorbed oxygen on Ni(110) by scanning tunnelling microscopy. *Phys. Rev. Lett*. **1982**, 52, 1304.

(19) Reichert, J.; Ochs, R.; Beckmann, D.; Weber, H. B.; Mayor, M.; Löhneysen, H. v. Driving Current through Single Organic Molecules. *Phys. Rev. Lett.* **2002**, *88*, 4.

(20) Nichols, R. J.; Higgins, S. J. Single-Molecule Electronics: Chemical and Analytical Perspectives. *Annu. Rev. Anal. Chem*. **2015**, 8, 389–417.

(21) Carlos Cuevas, J. Molecular electronics an introduction to theory and experiment. *World. Sci.* **2010**, 293, 19.

(22) Karthäuser, S. Control of Molecule-Based Transport for Future Molecular Devices. *J. Condens. Mater. Phys.* **2011**, 23, 013001.

(23) Cai, L.; Cabassi, M. A.; Yoon, H.; Cabarcos, O. M.; McGuiness, C. L.; Flatt, A. K.; Allara, D. L.; Tour, J. M.; Mayer, T. S. Reversible Bistable Switching in Nanoscale Thiol-Substituted Oligoaniline Molecular Junctions. *Nano Lett.* **2005**, *5*, 2365–2372.

(24) Hines, T.; Diez-Perez, I.; Hihath, J.; Liu, H.; Wang, Z. S.; Zhao, J.; Zhou, G.; Müllen, K.; Tao, N. Transition from Tunneling to Hopping in Single Molecular Junctions by Measuring Length and Temperature Dependence. *J. Am. Chem. Soc.* **2010**, *132*, 11658–11664.

(25) Song, H.; Kim, Y.; Jang, Y. H.; Jeong, H.; Reed, M. A.; Lee, T. Observation of Molecular Orbital Gating. *Nature* **2009**, 462, 1039–1043.

(26) Wang, G.; Kim, T. W.; Jo, G.; Lee, T. Enhancement of Field Emission Transport by Molecular Tilt Configuration in Metal-Molecule-Metal Junctions. *J. Am. Chem. Soc.* **2009**, *131*, 5980–5985.

(27) Xiang, D.; Zhang, Y.; Pyatkov, F.; Offenhausser, A.; Mayer, D. Gap Size Dependent Transition from Direct Tunneling to Field Emission in Single Molecule Junctions. *Chem. Comm.* **2011**, *47*, 4760-4762.

(28) Wang, W.; Lee, T.; Reed, A. Mechanism of Electron Conduction in Self-Assembled Alkanethiol Monolayer Devices. *Phys. Rev. B Condens. Matter.* **2003**, *68*, 035416.

(29) Bruot, C.; Hihath, J.; Tao, N. Mechanically Controlled Molecular Orbital Alignment in Single Molecule Junctions. *Nat. Nanotechnol.* **2012**, *7*, 35–40.

(30) Aradhya, S. V.; Venkataraman, L. Single-Molecule Junctions beyond Electronic Transport. *Nat. Nanotechnol*. **2013**, 8, 399–410.

(31) Natelson, D. Mechanical Break Junctions: Enormous Information in a Nanoscale Package. *ACS Nano*. **2012**, 6, 2871–2876.

(32) Nitzan, A.; Ratner, M. A. Electron Transport in Molecular Wire Junctions. *Science*. **2003**, 300, 1384-1389.

(33) Gschneidtner, T. A.; Diaz Fernandez, Y. A.; Moth-Poulsen, K. Progress in Self-Assembled Single-Molecule Electronic Devices. *J. Mater. Chem. C.* **2013**, *1*, 7127–7133.

(34) Bâldea, I. Why Asymmetric Molecular Coupling to Electrodes Cannot Be at Work in Real Molecular Rectifiers. *Phys. Rev. B.* **2021**, *103*, 195408.

(35) Datta, S.; Tian, W.; Hong, S.; Reifenberger, R.; Henderson, J. I.; Kubiak, C. P. Current-Voltage Characteristics of Self-Assembled Monolayers by Scanning Tunneling Microscopy. *Phys. Rev. Lett.* **1997**, 79, 2530.

(36) Joachim, C.; Ratner, M. A. Molecular Electronics: Some Views on Transport Junctions and Beyond. *PNAS*. **2005**, 102, 8801-8808.

(37) Xue, Y.; Datta, S.; Ratner, M. A. Charge Transfer and "Band Lineup" in Molecular Electronic Devices: A Chemical and Numerical Interpretation. *J. Chem. Phys.* **2001**, *115*, 4292–4299.

(38) Lyshevski. S. E. Nano- and Molecular electronics Handbook. *CRC Press*. **2007**, 25-1.

(39) Yanson, A. I.; Rubio Bollinger, G.; van den Brom, H. E.; Agrait, N. A.; van Ruitenbeek, J. M. Formation and Manipulation of a Metallic Wire of Single Gold Atoms. *Nature*. **1998**, 395, 783-785.

(40) Todorov, T. N.; Sutton, A. P. Jumps in Electronic Conductance Due to Mechanical Instabilities. *Phys. Rev. Lett*. **1993**, 70, 2138.

(41) Rubio, G.; Agrait, N. A.; Vieira, S. Atomic-Sized Metallic Contacts: Mechanical Properties and Electronic Transport, *Phys. Rev. Lett*. **1996**, 76, 2302.

(42) David Bohm. Quantum Theory; *Prentice-Hall*, **1951**, 81-95.

(43) Ioan Baldea. Molecular Electronics: An Experimental and Theoretical Approach. *Pan Stanford Pub*, **2016**, 1, 80-90.

(44) Landau, L. D. and L. E. M. Quantum Mechanics (Non-Relativistic Theory, *Pergamon Press*, **1977**, 3. 110-120

(45) Burstein, E. Tunnelling Phenomena in Solids. *Springer*. **1969**, 235-237.

(46) Simmons, J. G. Electric Tunnel Effect between Dissimilar Electrodes Separated by a Thin Insulating Film. *J. App. Phys.* **1963**, *34*, 2581–2590.

(47) Simmons, J. G. Generalized Formula for the Electric Tunnel Effect between Similar Electrodes Separated by a Thin Insulating Film. *J. App. Phys.* **1963**, *34*,1793–1803.

(48) Holmlin, R. E.; Haag, R.; Chabinyc, M. L.; Ismagilov, R. F.; Cohen, A. E.; Terfort, A.; Rampi, M. A.; Whitesides, G. M. Electron Transport through Thin Organic Films in Metal-Insulator-Metal Junctions Based on Self-Assembled Monolayers. *J Am Chem Soc* **2001**, *123*, 5075–5085.

(49) Simmons, J. G. Low-Voltage Current-Voltage Relationship of Tunnel Junctions. *J. App. Phys.* 1963, 238–239.

(50) Vilan, A. Analyzing Molecular Current-Voltage Characteristics with the Simmons Tunneling Model: Scaling and Linearization. *The J. Phys. Chem. C.* **2007**, *111*, 4431-4444.

(51) Meier, T. T. P. K. S. W. Coherent Semiconductor Optics: From Basic Concepts to Nanostructure Applications. **2007**, 25-33.

(52) Ioan Baldea. Molecular Electronics: An Experimental and Theoretical Approach. *Pan Stanford Pub*. **2016**, 7-9.

(53) Wang, W.; Lee, T.; Kretzschmar, I.; Reed, M. A. Inelastic Electron Tunneling Spectroscopy of an Alkanedithiol Self-Assembled Monolayer. *Nano Lett.* **2004**, *4*, 643–646.

(54) Qian, H.; Hsu, S. W.; Gurunatha, K.; Riley, C. T.; Zhao, J.; Lu, D.; Tao, A. R.; Liu, Z. Efficient Light Generation from Enhanced Inelastic Electron Tunnelling. *Nature*, **2018**, 485–488.

(55) Rawat, A.; Mahavar, H. K.; Chauhan, S.; Tanwar, A.; Singh, P. J. Optical Band Gap of Polyvinylpyrrolidone/Polyacrilamide Blend Thin Films. **2012**, 50, 100-104.

(56) Paul, D. J. Encyclopaedia of Physical Science and Technology. **2003**, 3, 285-301.

(57) Mugarza, A.; Robles, R.; Krull, C.; Korytár, R.; Lorente, N.; Gambardella, P. Electronic and Magnetic Properties of Molecule-Metal Interfaces: Transition-Metal Phthalocyanines Adsorbed on Ag(100). *Phys. Rev. B.* **2012**, *85*, 155437.

(58) Oncel, N.; Hallback, A. S.; Zandvliet, H. J. W.; Speets, E. A.; Ravoo, B. J.; Reinhoudt, D. N.; Poelsema, B. Coulomb Blockade of Small Pd Clusters. *J. Chem. Phys.* **2005**, *123*, 044703.

(59) Andres, R. P.; Bein, T.; Dorogi, M.; Feng, S.; Henderson, J. 1; Kubiak, C. P.; Mahoney, W.; Osifchin, R. G.; Reifenberger, R. "Coulomb Staircase" at Room Temperature in a Self-Assembled Molecular Nanostructure. *Europe PMC*. **1996**, 272, 1323-1325.

(60) Nesvorńy, D.; Bottke, W. F.; Dones, L.; Levison, H. F. The Recent Breakup of an Asteroid in the Main-Belt Region. *Nature* **2002**, *417*, 720–722.

(61) Berkelaar, R. P.; Söde, H.; Mocking, T. F.; Kumar, A.; Poelsema, B.; Zandvliet, H. J. W. Molecular Bridges. *J. Phys. Chem. C.* **2011**, 115, 2268–2272.

(62) Adibi. A. Comprehensive Semiconductor Science and Technology. *Elsevier*, **2011**, 5, 376-380.

(63) Lee, K.; Kulkarni, G.; Zhong, Z. Coulomb Blockade in Monolayer MoS2 Single Electron Transistor. *Nanoscale,* **2016**, *8*, 7755–7760.

(64) Horiuchi, T.; Ebisawa, F.; Tabei, H. New Inelastic Electron Tunneling Spectrometer with an Absolute Peak Intensity. *Rev. Sci. Instrum.* **1989**, *60*, 993–996.

(65) Wang, W.; Lee, T.; Reed, M. A. Electron Tunnelling in Self-Assembled Monolayers. *Rep. Prog. Phys.* **2005**, *68*, 523–544.

(66) Aviram, A. E.; Molecular Electronics II. *The Annals of the New York Academy of Sciences*, **2002**, 960.

(67) Sze, S. M. Physics of Semiconductor Devices. *Wiley*. **2012**, 242-243.

(68) Rhoderick, E. H. Metal-Semiconductor Contacts. *Oxford*. **1988**, 168-185.

(69) Ho Choi, S.; Kim, B.; Frisbie, C. D. Electrical Resistance of Long Conjugated Molecular Wires. *Science.* **1979**, *320, 1482-1486*.

(70) Fowler, R. H. and N. L. Electron Emission in Intense Electric Fields. *Proc. R. Soc.* **1928**, *119*, 173-181.

(71) Xiu-Juan Yan, S.-L. C. Electronic Devices and Functional Structures Based on Nanostructured Semiconductors. Nanostructured Semiconductor Oxides for the Next Generation of Electronics and Functional Devices; Elsevier, **2014**, 185-186.

(72) Awan, T. I.; Bashir, A.; Tehseen, A.; Bibi, S. Electrons in Nanostructures. In *Chemistry of Nanomaterials*. *Elsevie*r. **2020**, 183-184.

(73) Noguchi, Y.; Nagase, T.; Ueda, R.; Kamikado, T.; Kubota, T.; Mashiko, S. Fowler–Nordheim Tunneling in Electromigrated Break Junctions with Porphyrin Molecules. *Jpn. J. Appl. Phys.* **2007**, *46*, 2683.

(74) Wang, W.; Lee, T.; Reed, M. A. Intrinsic Electronic Conduction Mechanisms in Self-Assembled Monolayers. In Introducing Molecular Electronics. *Springer*. **2005**, 680, 275-300.

(75) Xu, B. Measurement of Single-Molecule Resistance by Repeated Formation of Molecular Junctions. *Science.* **1979**, *301*, 1221-1223.

(76) Landauer, R. Spatial Variation of Currents and Fields Due to Localized Scatterers in Metallic Conduction. *IBM J. Res. Dev.* **1988**, *32*, 303-316.

(77) Tang, Y.; Zhou, Y.; Zhou, D.; Chen, Y.; Xiao, Z.; Shi, J.; Liu, J.; Hong, W. Electric Field-Induced Assembly in Single-Stacking Terphenyl Junctions. *J Am Chem Soc.* **2020**, *142*, 19101-19109.

(78) el Abbassi, M.; Zwick, P.; Rates, A.; Stefani, D.; Prescimone, A.; Mayor, M.; van der Zant, H. S. J.; Dulić, D. Unravelling the Conductance Path through Single-Porphyrin Junctions. *Chem. Sci.* **2019**, *10*, 8299–8305.

(79) Inkpen, M. S.; Lemmer, M.; Fitzpatrick, N.; Milan, D. C.; Nichols, R. J.; Long, N. J.; Albrecht, T. New Insights into Single-Molecule Junctions Using a Robust, Unsupervised Approach to Data Collection and Analysis. *J Am Chem Soc.* **2015**, *137*, 9971–9981.

(80) Lemmer, M.; Inkpen, M. S.; Kornysheva, K.; Long, N. J.; Albrecht, T. Unsupervised Vector-Based Classification of Single-Molecule Charge Transport Data. *Nat. Commun.* **2016**, *7*, 12922.

(81) Vladyka, A.; Albrecht, T. Unsupervised Classification of Single-Molecule Data with Autoencoders and Transfer Learning. *Machine Learning: Sci. Technol.* **2020**, *1*, 035013.

(82) Albrecht, T.; Slabaugh, G.; Alonso, E.; Al-Arif, S. M. R. Deep Learning for Single-Molecule Science. *Nanotechnology.* **2017**, *28*, 423001.

(83) Magyarkuti, A.; Balogh, N.; Balogh, Z.; Venkataraman, L.; Halbritter, A. Unsupervised Feature Recognition in Single-Molecule Break Junction Data. *Nanoscale.* **2020**, *12*, 8355–8363.

(84) Huang, F.; Li, R.; Wang, G.; Zheng, J.; Tang, Y.; Liu, J.; Yang, Y.; Yao, Y.; Shi, J.; Hong, W. Automatic Classification of Single-Molecule Charge Transport Data with an Unsupervised Machine-Learning Algorithm. *Phys. Chem. Chem. Phys.* **2020**, *22*, 1674–1681.

(85) Cabosart, D.; el Abbassi, M.; Stefani, D.; Frisenda, R.; Calame, M.; van der Zant, H. S. J.; Perrin, M. L. A Reference-Free Clustering Method for the Analysis of Molecular Break-Junction Measurements. *Appl. Phys. Lett.* **2019**, *114*, 143102.

(86) Vezzoli, A.; Brooke, R. J.; Ferri, N.; Higgins, S. J.; Schwarzacher, W.; Nichols, R. J. Single-Molecule Transport at a Rectifying GaAs Contact. *Nano Lett.* **2017**, *17, 1109-1115*.

(87) Pires, E.; Macdonald, J. E.; Elliott, M. Chain Length and Temperature Dependence of Alkanedithiol Molecular Conductance under Ultra High Vacuum. *Nanoscale.* **2013**, *5*, 9397-9403.

(88) Leary, E.; Limburg, B.; Alanazy, A.; Sangtarash, S.; Grace, I.; Swada, K.; Esdaile, L. J.; Noori, M.; González, M. T.; Rubio-Bollinger, G.; Sadeghi, H.; Hodgson, A.; Agrait, N.; Higgins, S. J.; Lambert, C. J.; Anderson, H. L.; Nichols, R. J. Bias-Driven Conductance Increase with Length in Porphyrin Tapes. *J Am Chem Soc.* **2018**, *140*, 12877-12883.

(89) Komoto, Y.; Isshiki, Y.; Fujii, S.; Nishino, T.; Kiguchi, M. Evaluation of the Electronic Structure of Single-Molecule Junctions Based on Current-Voltage and Thermopower Measurements: Application to C_{60} Single-Molecule Junction. *Chem. Asian J.* **2017**, 12, 440-445.

(90) Zhao, J.; Yu, C.; Wang, N.; Liu, H. Molecular Rectification Based on Asymmetrical Molecule−Electrode Contact. *J. Phys. Chem.* **2010**, 114, 4135-4141.

(91) Isshiki, Y.; Matsuzawa, Y.; Fujii, S.; Kiguchi, M. Investigation on Single-Molecule Junctions Based on Current–Voltage Characteristics. *Micromachines.* **2018**, *9*, 67.

(92) Cuevas, J. C. The Birth of Molecular Electronics. In Molecular Electronics. *WORLD SCIENTIFIC*. **2017**, 3-18.

(93) Su, T. A.; Neupane, M.; Steigerwald, M. L.; Venkataraman, L.; Nuckolls, C. Chemical Principles of Single-Molecule Electronics. *Nat. Rev. Mater.* **2016**, *1*, 16002.

(94) Venkataraman, L.; Klare, J. E.; Tam, I. W.; Nuckolls, C.; Hybertsen, M. S.; Steigerwald, M. L. Single-Molecule Circuits with Well-Defined Molecular Conductance. *Nano. Lett*. **2006**, 6, 458-462.

(95) Ulman, A. An Introduction to Ultrathin Organic Films. *Elsevier*. **1991**, 240-241.

(96) Su, T. A.; Neupane, M.; Steigerwald, M. L.; Venkataraman, L.; Nuckolls, C. Chemical Principles of Single-Molecule Electronics. *Nat. Rev. Mater.* **2016**, *1*,16002.

(97) Kim, T.; Vázquez, H.; Hybertsen, M. S.; Venkataraman, L. Conductance of Molecular Junctions Formed with Silver Electrodes. *Nano Lett.* **2013**, *13*, 3358–3364.

(98) He, C.; Zhang, Q.; Gao, T.; Liu, C.; Chen, Z.; Zhao, C.; Zhao, C.; Nichols, R. J.; Dappe, Y. J.; Yang, L. Charge Transport in Hybrid Platinum/Molecule/Graphene Single Molecule Junctions. *Phys. Chem. Chem. Phys.* **2020**, *22*, 13498–13504.

(99) Catarelli, S. R.; Higgins, S. J.; Schwarzacher, W.; Mao, B.-W.; Yan, J.-W.; Nichols, R. J. Ionic Liquid Based Approach for Single-Molecule Electronics with Cobalt Contacts. *Langmuir.* **2014**, *30*, 14329-14336.

(100) Brooke, R. J.; Jin, C.; Szumski, D. S.; Nichols, R. J.; Mao, B.-W.; Thygesen, K. S.; Schwarzacher, W. Single-Molecule Electrochemical Transistor Utilizing a Nickel-Pyridyl Spinterface. *Nano Lett.* **2015**, *15*, 275–280.

(101) Vezzoli, A.; Brooke, R. J.; Higgins, S. J.; Schwarzacher, W.; Nichols, R. J. Single-Molecule Photocurrent at a Metal–Molecule–Semiconductor Junction. *Nano Lett.* **2017**, *17*, 6702–6707.

(102) Zhang, Q.; Liu, L.; Tao, S.; Wang, C.; Zhao, C.; González, C.; Dappe, Y. J.; Nichols, R. J.; Yang, L. Graphene as a Promising Electrode for Low-Current Attenuation in Nonsymmetric Molecular Junctions. *Nano Lett.* **2016**, *16*, 6534–6540.

(103) Ko, C.-H.; Huang, M.-J.; Fu, M.-D.; Chen, C. Superior Contact for Single-Molecule Conductance: Electronic Coupling of Thiolate and Isothiocyanate on Pt, Pd, and Au. *J Am Chem Soc.* **2010**, *132*, 756-764.

(104) Seminario, J. M.; de La Cruz, C. E.; Derosa, P. A. A Theoretical Analysis of Metal−Molecule Contacts. *J Am Chem Soc.* **2001**, *123*, 5616-5617.

(105) Young, R.; Ward, J.; Scire, F. The Topografiner: An Instrument for Measuring Surface Microtopography. *Rev. Sci. Instrum.* **1972**, *43*, 999.

(106) Bock, S. Molecular Design Strategies for Molecular Electronics, The University of Western Australia, Perth, **2017**, 96.

(107) Saheb, A.; Janata, J.; Josowicz, M. Reference Electrode for Ionic Liquids. *Electroanalysis.* **2006**, *18*, 405-409.

(108) Mészáros, G.; Li, C.; Pobelov, I.; Wandlowski, T. Current Measurements in a Wide Dynamic Range—Applications in Electrochemical Nanotechnology. *Nanotechnology*. **2007**, *18*, 424004.

(109) Magyarkuti, A.; Adak, O.; Halbritter, A.; Venkataraman, L. Electronic and Mechanical Characteristics of Stacked Dimer Molecular Junctions. *Nanoscale.* **2018**, *10*, 3362-3368.

(110) Lambert, C. J. Basic Concepts of Quantum Interference and Electron Transport in Single-Molecule Electronics. *Che. Soc. Rev.* **2015**, *44*, 875-888.

(111) Vezzoli, A. Metal Complexes and Clusters in Single-Molecule Electronics. In Encyclopedia of Inorganic and Bioinorganic Chemistr*y*. Wiley. **202**1, 1–21.

(112) Sedghi, G.; García-Suárez, V. M.; Esdaile, L. J.; Anderson, H. L.; Lambert, C. J.; Martín, S.; Bethell, D.; Higgins, S. J.; Elliott, M.; Bennett, N.; Macdonald, J. E.; Nichols, R. J. Long-Range Electron

Tunnelling in Oligo-Porphyrin Molecular Wires. *Nature Nanotechnology.* **2011**, *6*, 517–523.

(113) Zhao, X.; Huang, C.; Gulcur, M.; Batsanov, A. S.; Baghernejad, M.; Hong, W.; Bryce, M. R.; Wandlowski, T. Oligo(Aryleneethynylene)s with Terminal Pyridyl Groups: Synthesis and Length Dependence of the Tunneling-to-Hopping Transition of Single-Molecule Conductances. *Chem. Mater.* **2013**, *25*, 4340–4347.

(114) Gunasekaran, S.; Greenwald, J. E.; Venkataraman, L. Visualizing Quantum Interference in Molecular Junctions. *Nano Lett.* **2020**, *20*, 2843-2848.

(115) Miao, R.; Xu, H.; Skripnik, M.; Cui, L.; Wang, K.; Pedersen, K. G. L.; Leijnse, M.; Pauly, F.; Wärnmark, K.; Meyhofer, E.; Reddy, P.; Linke, H. Influence of Quantum Interference on the Thermoelectric Properties of Molecular Junctions. *Nano Lett.* **2018**, *18*, 5666-5672.

(116) Garner, M. H.; Li, H.; Chen, Y.; Su, T. A.; Shangguan, Z.; Paley, D. W.; Liu, T.; Ng, F.; Li, H.; Xiao, S.; Nuckolls, C.; Venkataraman, L.; Solomon, G. C. Comprehensive Suppression of Single-Molecule Conductance Using Destructive σ-Interference. *Nature.* **2018**, *558*, 415-419.

(117) Li, Y.; Buerkle, M.; Li, G.; Rostamian, A.; Wang, H.; Wang, Z.; Bowler, D. R.; Miyazaki, T.; Xiang, L.; Asai, Y.; Zhou, G.; Tao, N. Gate Controlling of Quantum Interference and Direct Observation of Anti-Resonances in Single Molecule Charge Transport. *Nat. Mater.* **2019**, *18*, 357-363.

(118) Debray, P.; Raichev, O. E.; Vasilopoulos, P.; Rahman, M.; Perrin, R.; Mitchell, W. C. Ballistic Electron Transport in Stubbed Quantum Waveguides: Experiment and Theory. *Phys. Rev. B.* **2000**, *61*, 10950.

(119) Porod, W.; Shao, Z.; Lent, C. S. Resonance-Antiresonance Line Shape for Transmission in Quantum Waveguides with Resonantly Coupled Cavities. *Phys. Rev. B.* **1993**, *48*, 8495.

(120) Baer, R.; Neuhauser, D. Phase Coherent Electronics: A Molecular Switch Based on Quantum Interference. *J Am Chem Soc.* **2002**, *124*, 4200-4201.

(121) Stadler, R. Quantum Interference Effects in Electron Transport: How to Select Suitable Molecules for Logic Gates and Thermoelectric Devices. *J. Appl. Phys*. **2013**, 074308.

(122) Papadopoulos, T. A.; Grace, I. M.; Lambert, C. J. Control of Electron Transport through Fano Resonances in Molecular Wires. *Phys. Rev. B.* **2006**, *74*, 193306.

(123) Cardamone, D. M.; Stafford, C. A.; Mazumdar, S. Controlling Quantum Transport through a Single Molecule. *Nano Lett.* **2006**, *6*, 2422-2426.

(124) Stafford, C. A.; Cardamone, D. M.; Mazumdar, S. The Quantum Interference Effect Transistor. *Nanotechnology.* **2007**, *18*, 424014.

(125) Ke, S.-H.; Yang, W.; Baranger, H. U. Quantum-Interference-Controlled Molecular Electronics. *Nano Lett.* **2008**, *8, 3257-3261*.

(126) Andrews, D. Q.; Solomon, G. C.; van Duyne, R. P.; Ratner, M. A. Single Molecule Electronics: Increasing Dynamic Range and

Switching Speed Using Cross-Conjugated Species. *J Am Chem Soc.* **2008**, *130*, 17309-17319 .

(127) Solomon, G. C.; Andrews, D. Q.; Goldsmith, R. H.; Hansen, T.; Wasielewski, M. R.; van Duyne, R. P.; Ratner, M. A. Quantum Interference in Acyclic Systems: Conductance of Cross-Conjugated Molecules. *J Am Chem Soc.* **2008**, *130*, 17301-17308.

(128) Solomon, G. C.; Andrews, D. Q.; van Duyne, R. P.; Ratner, M. A. When Things Are Not as They Seem: Quantum Interference Turns Molecular Electron Transfer "Rules" Upside Down. *J Am Chem Soc.* **2008**, *130*, 7788-7789.

(129) Markussen, T.; Schiötz, J.; Thygesen, K. S. Electrochemical Control of Quantum Interference in Anthraquinone-Based Molecular Switches. *Chem. Phys.* **2010**, *132, 224104*.

(130) Naghibi, S.; Ismael, A. K.; Vezzoli, A.; Al-Khaykanee, M. K.; Zheng, X.; Grace, I. M.; Bethell, D.; Higgins, S. J.; Lambert, C. J.; Nichols, R. J. Synthetic Control of Quantum Interference by Regulating Charge on a Single Atom in Heteroaromatic Molecular Junctions. *J. Phys. Chem. Lett.* **2019**, *10*, 6419-6424.

(131) Ohtani, B. Photocatalysis by Inorganic Solid Materials. *Adv. Inorg. Chem*. **2011**, 63, 395-430.

(132) Gantenbein, M.; Wang, L.; Al-jobory, A. A.; Ismael, A. K.; Lambert, C. J.; Hong, W.; Bryce, M. R. Quantum Interference and Heteroaromaticity of Para- and Meta-Linked Bridged Biphenyl Units

in Single Molecular Conductance Measurements. *Sci. Rep.* **2017**, *7*, 1794.

(133) Chen, W.; Li, H.; Widawsky, J. R.; Appayee, C.; Venkataraman, L.; Breslow, R. Aromaticity Decreases Single-Molecule Junction Conductance. *J. Am. Chem. Soc.* **2014**, *136*, 918-920.

(134) Klausen, R. S.; Widawsky, J. R.; Su, T. A.; Li, H.; Chen, Q.; Steigerwald, M. L.; Venkataraman, L.; Nuckolls, C. Evaluating Atomic Components in Fluorene Wires. *Chem. Sci.* **2014**, *5*, 1561-1564.

(135) Bai, J.; Daaoub, A.; Sangtarash, S.; Li, X.; Tang, Y.; Zou, Q.; Sadeghi, H.; Liu, S.; Huang, X.; Tan, Z.; Liu, J.; Yang, Y.; Shi, J.; Mészáros, G.; Chen, W.; Lambert, C.; Hong, W. Anti-Resonance Features of Destructive Quantum Interference in Single-Molecule Thiophene Junctions Achieved by Electrochemical Gating. *Nat. Mater.* **2019**, *18*, 364-369.

(136) Huang, B.; Liu, X.; Yuan, Y.; Hong, Z.-W.; Zheng, J.-F.; Pei, L.-Q.; Shao, Y.; Li, J.-F.; Zhou, X.-S.; Chen, J.-Z.; Jin, S.; Mao, B.-W. Controlling and Observing Sharp-Valleyed Quantum Interference Effect in Single Molecular Junctions. *J. Am. Chem. Soc.* **2018**, *140*, 17685-17690.

(137) Guillory, J. K. Book Review of CRC Handbook of Chemistry and Physics. 91st Edition. *J. Med.l Chem.* **2010**, *53*.

(138) Ferrer, J.; Lambert, C. J.; García-Suárez, V. M.; Manrique, D. Z.; Visontai, D.; Oroszlany, L.; Rodríguez-Ferradás, R.; Grace, I.; Bailey,

S. W. D.; Gillemot, K.; Sadeghi, H.; Algharagholy, L. A. GOLLUM: A next-Generation Simulation Tool for Electron, Thermal and Spin Transport. *New. J. Phy.* **2014**, *16*, 093029.

(139) Hung, Y.-C.; Jiang, J.-C.; Chao, C.-Y.; Su, W.-F.; Lin, S.-T. Theoretical Study on the Correlation between Band Gap, Bandwidth, and Oscillator Strength in Fluorene-Based Donor−Acceptor Conjugated Copolymers. *J. Phys. Chem. B.* **2009**, *113*, 8268-8277.

(140) Lof, R. W.; van Veenendaal, M. A.; Jonkman, H. T.; Sawatzky, G. A. Band Gap, Excitons and Coulomb Interactions of Solid C60. *Phys. Rev. Lett.* **1995**, *72, 3924*.

(141) Neaton, J. B.; Hybertsen, M. S.; Louie, S. G. Renormalization of Molecular Electronic Levels at Metal-Molecule Interfaces. *Phys. Rev. Lett.* **2006**, *97*, 216405.

(142) Fiorentini, V.; Baldereschi, A. Dielectric Scaling of the Self-Energy Scissor Operator in Semiconductors and Insulators. *Phys. Rev. B.* **1995**, *51, 17196*.

(143) Godby, R. W.; Schlüter, M.; Sham, L. J. Self-Energy Operators and Exchange-Correlation Potentials in Semiconductors. *Phys. Rev. B.* **1988**, *37*, 10159.

(144) Ramsden, J. Applied Nanotechnology. *Elsevier*, **2014**, 85-86.

(145) Lehn, J. Molecular and Supramolecular Devices. In Supramolecular Chemistry; *Wiley-VCH Verlag GmbH & Co*. **2006**.

(146) *Calixarenes and Beyond*; Neri, P., Sessler, J. L., Wang, M.-X., Eds.; Springer International Publishing: Cham, 2016.

(147) Vasile, C. Polymeric Nanomaterials in Nanotherapeutics; *Elsevier*, **2019**, 237-238.

(148) Moulin, E.; Busseron, E.; Giuseppone, N. Supramolecular Materials in Organic Electronics. *RSC*. **2014**, 1-2.

(149) Lah, N. A. C.; Zubir, M. N. M.; Samykano, M. A. Engineered Nanomaterial in Electronics and Electrical Industries, Handbook of nanomaterials for industrial applications. *MNT*, **2018**, 324-364.

(150) Sebastian, A.; le Gallo, M.; Khaddam-Aljameh, R.; Eleftheriou, E. Memory Devices and Applications for In-Memory Computing. *Nat. Nanotechnol.* **2020**, *15*, 529-544.

(151) Martins, T. D.; Ribeiro, A. C. C.; Colmati, F.; de Souza, G. A.; de Camargo, H. S.; Dias, D. L.; Filho, P. A. da C.; Cordeiro, D. de S. Supramolecular Materials for Optical and Electrochemical Biosensors. In Biosensors - Micro and Nanoscale Applications; *InTech*, **2015**.

(152) Salahuddin, N.; Galal, A. Improving Chemotherapy Drug Delivery by Nanoprecision Tools. In Nanostructures for Cancer Therapy. *Elsevier*. **2017**, 87-128.

(153) Peixoto, A. C.; Silva, A. F. Smart Devices. In Bioinspired Materials for Medical Applications. *Elsevier*. **2017**, 131-132.

(154) Cea, P.; Ballesteros, L. M.; Martín, S. Nanofabrication Techniques of Highly Organized Monolayers Sandwiched between Two Electrodes for Molecular Electronics. *Nanofabrication.* **2014**, 10, 6064.

(155) Liu, Y.; Wei, Z. Molecular Electronic Junctions Based on Self-Assembled Monolayers. In Nanogap Electrodes. *Wiley*. **2021**, 301–343.

(156) Park, S.; Jang, J.; Yoon, H. J. Validating the Mott Formula with Self-Assembled Monolayer (SAM)-Based Large-Area Junctions: Effect of Length, Backbone, Spacer, Substituent, and Electrode on the Thermopower of SAMs. *J. Phys. Chem. C.* **2021**, *125*, 20035–20047.

(157) YALIRAKI, S. N.; RATNER, M. A. Interplay of Topology and Chemical Stability on the Electronic Transport of Molecular Junctions. *Ann. N. Y. Acad. Sci.* **2006**, *960*, 153-162.

(158) Collier, C. P. Electronically Configurable Molecular-Based Logic Gates. *Science.* **1979**, *285*, 391-394.

(159) Chen, Z.; Adil, K.; Weseliński, Ł. J.; Belmabkhout, Y.; Eddaoudi, M. A Supermolecular Building Layer Approach for Gas Separation and Storage Applications: The Eea and Rtl MOF Platforms for CO_2 Capture and Hydrocarbon Separation. *J. Mater. Chem. A.* **2015**, *3*, 6276–6281.

(160) Chen, H.; Zeng, W.; Liu, Y.; Dong, W.; Cai, T.; Tang, L.; Li, J.; Li, W. Unique MIL-53(Fe)/PDI Supermolecule Composites: Z-Scheme Heterojunction and Covalent Bonds for Uprating Photocatalytic Performance. *ACS App. Mater. Interfaces.* **2021**, *13*, 16364–16373.

(161) Ogoshi, T.; Yamagishi, T. Chapter 1. Historical Background of Macrocyclic Compounds. *RSC*. **2015**, 1-19.

(162) Li, H.; Yang, Y.; Xu, F.; Liang, T.; Wen, H.; Tian, W. Pillararene-Based Supramolecular Polymers. *ChemComm.* **2019**, *55*, 271-285.

(163) Ogoshi, T.; Kanai, S.; Fujinami, S.; Yamagishi, T.; Nakamoto, Y. Para-Bridged Symmetrical Pillar[5]Arenes: Their Lewis Acid Catalyzed Synthesis and Host–Guest Property. *J. Am. Chem. Soc.* **2008**, *130*, 5022–5023.

(164) Ogoshi, T.; Yamagishi, T. Chapter 5. Host–Guest Properties of Pillar[n]Arenes. *RSC*. **2015**, 90–133.

(165) Wang, Y.; Ping, G.; Li, C. Efficient Complexation between Pillar[5]Arenes and Neutral Guests: From Host–Guest Chemistry to Functional Materials. *ChemComm.* **2016**, *52*, 9858-9872.

(166) Griessl, S.; Lackinger, M.; Edelwirth, M.; Hietschold, M.; Heckl, W. M. Self-Assembled Two-Dimensional Molecular Host-Guest Architectures From Trimesic Acid. *Single Mol.* **2002**, *3*, 25-31.

(167) Ogoshi, T.; Takashima, S.; Yamagishi, T. Molecular Recognition with Microporous Multilayer Films Prepared by Layer-by-Layer Assembly of Pillar[5]Arenes. *J. Am. Chem. Soc.* **2015**, *137*, 10962-10964.

(168) Luo, L.; Nie, G.; Tian, D.; Deng, H.; Jiang, L.; Li, H. Dynamic Self-Assembly Adhesion of a Paraquat Droplet on a Pillar[5]Arene Surface. *Angew. Chem. Int. Ed.* **2016**, *55*, 12713-12716.

(169) Zhou, T.; Song, N.; Yu, H.; Yang, Y.-W. Pillar[5,6]Arene-Functionalized Silicon Dioxide: Synthesis, Characterization, and Adsorption of Herbicide. *Langmuir.* **2015**, *31*, 1454-1461.

(170) Yang, K.; Pei, Y.; Wen, J.; Pei, Z. Recent Advances in Pillar[n]Arenes: Synthesis and Applications Based on Host–Guest Interactions. *Chem. Commun.* **2016**, *52*, 9316-9326.

(171) Ogoshi, T.; Yamagishi, T. Pillar[5]- and Pillar[6]Arene-Based Supramolecular Assemblies Built by Using Their Cavity-Size-Dependent Host–Guest Interactions. *Chem. Commun.* **2014**, *50*, 4776-4787.

(172) Dong, S.; Zheng, B.; Yao, Y.; Han, C.; Yuan, J.; Antonietti, M.; Huang, F. LCST-Type Phase Behavior Induced by Pillar[5]Arene/Ionic Liquid Host-Guest Complexation. *Advanced Materials* **2013**, *25*, 6864-6867.

(173) Ghane, T.; Nozaki, D.; Dianat, A.; Vladyka, A.; Gutierrez, R.; Chinta, J. P.; Yitzchaik, S.; Calame, M.; Cuniberti, G. Interplay between Mechanical and Electronic Degrees of Freedom in π-Stacked Molecular Junctions: From Single Molecules to Mesoscopic Nanoparticle Networks. *J. Phys. Chem. C.* **2015**, *119*, 6344–6355.

(174) Fu, T.; Smith, S.; Camarasa-Gómez, M.; Yu, X.; Xue, J.; Nuckolls, C.; Evers, F.; Venkataraman, L.; Wei, S. Enhanced Coupling through π-Stacking in Imidazole-Based Molecular Junctions. *Chem. Sci.* **2019**, *10*, 9998-10002.

(175) Wu, S.; González, M. T.; Huber, R.; Grunder, S.; Mayor, M.; Schönenberger, C.; Calame, M. Molecular Junctions Based on Aromatic Coupling. *Nat. Nanotechnol.* **2008**, *3*, 569-574.

(176) Zheng, J.-T.; Yan, R.-W.; Tian, J.-H.; Liu, J.-Y.; Pei, L.-Q.; Wu, D.-Y.; Dai, K.; Yang, Y.; Jin, S.; Hong, W.; Tian, Z.-Q. Electrochemically Assisted Mechanically Controllable Break Junction Studies on the Stacking Configurations of Oligo(Phenylene Ethynylene)s Molecular Junctions. *Electrochim. Acta.* **2016**, *200, 2-8*.

(177) Frisenda, R.; Janssen, V. A. E. C.; Grozema, F. C.; van der Zant, H. S. J.; Renaud, N. Mechanically Controlled Quantum Interference in Individual π-Stacked Dimers. *Nat. Chem.* **2016**, *8*, 1126-1132.

(178) Mao, J.-C.; Peng, L.-L.; Li, W.-Q.; Chen, F.; Wang, H.-G.; Shao, Y.; Zhou, X.-S.; Zhao, X.; Xie, H.-J.; Niu, Z. Influence of Molecular Structure on Contact Interaction between Thiophene Anchoring Group and Au Electrode. *J. Phys. Chem. C.* **2017**, *121*, 1472–1476.

(179) Hicks, R. G. What's New in Stable Radical Chemistry? *Org. Biomol. Chem.* **2007**, *5*, 1321-1338.

(180) Karlsson, C.; Suga, T.; Nishide, H. Quantifying TEMPO Redox Polymer Charge Transport toward the Organic Radical Battery. *ACS Applied Materials & Interfaces* **2017**, *9* (12).

(181) Beldjoudi, Y.; Nascimento, M. A.; Cho, Y. J.; Yu, H.; Aziz, H.; Tonouchi, D.; Eguchi, K.; Matsushita, M. M.; Awaga, K.; Osorio-Roman, I.; Constantinides, C. P.; Rawson, J. M. Multifunctional Dithiadiazolyl Radicals: Fluorescence, Electroluminescence, and Photoconducting Behavior in Pyren-1′-Yl-Dithiadiazolyl. *J. Am. Chem. Soc.* **2018**, *140*, 10692-10698.

(182) Wang, Z.; Zhao, J.; Barbon, A.; Toffoletti, A.; Liu, Y.; An, Y.; Xu, L.; Karatay, A.; Yaglioglu, H. G.; Yildiz, E. A.; Hayvali, M. Radical-Enhanced Intersystem Crossing in New Bodipy Derivatives and Application for Efficient Triplet–Triplet Annihilation Upconversion. *J. Am. Chem. Soc.* **2017**, *139*, 7831-7842.

(183) Slota, M.; Keerthi, A.; Myers, W. K.; Tretyakov, E.; Baumgarten, M.; Ardavan, A.; Sadeghi, H.; Lambert, C. J.; Narita, A.; Müllen, K.; Bogani, L. Magnetic Edge States and Coherent Manipulation of Graphene Nanoribbons. *Nature.* **2018**, *557*, 691-695.

(184) Gilroy, J. B.; McKinnon, S. D. J.; Koivisto, B. D.; Hicks, R. G. Electrochemical Studies of Verdazyl Radicals. *Org. Lett.* **2007**, *9*, 4837-4840.

(185) Brook, D. J. R. Coordination Chemistry of Verdazyl Radicals. *Comments Inorg. Chem.* **2015**, *35*. 1-17.

(186) Petunin, P. v.; Martynko, E. A.; Trusova, M. E.; Kazantsev, M. S.; Rybalova, T. v.; Valiev, R. R.; Uvarov, M. N.; Mostovich, Evgeny. A.; Postnikov, P. S. Verdazyl Radical Building Blocks: Synthesis, Structure, and Sonogashira Cross-Coupling Reactions. *EurJOC,* **2018**, 34, 4802-4811.

(187) Ratera, I.; Veciana, J. Playing with Organic Radicals as Building Blocks for Functional Molecular Materials. *Chem. Soc. Rev.* **2012**, *41*, 303-349.

(188) Gomberg, M. AN INSTANCE OF TRIVALENT CARBON: TRIPHENYLMETHYL. *J. Am. Chem. Soc.* **1900**, *22*, 757-771.

(189) Ji, L.; Shi, J.; Wei, J.; Yu, T.; Huang, W. Air-Stable Organic Radicals: New-Generation Materials for Flexible Electronics?. *Adv. Mater.* **2020**, *32*, 1908015.

(190) Wang, K.; Vezzoli, A.; Grace, I. M.; McLaughlin, M.; Nichols, R. J.; Xu, B.; Lambert, C. J.; Higgins, S. J. Charge Transfer Complexation Boosts Molecular Conductance through Fermi Level Pinning. *Chem. Sci.* **2019**, *10*, 2396-2403.

(191) Perrin, M. L.; Eelkema, R.; Thijssen, J.; Grozema, F. C.; van der Zant, H. S. J. Single-Molecule Functionality in Electronic Components Based on Orbital Resonances. *Phys. Chem. Chem. Phys.* **2020**, *22*, 12849-12866.

(192) Gryn'ova, G.; Coote, M. L.; Corminboeuf, C. Theory and Practice of Uncommon Molecular Electronic Configurations. *Wiley Interdiscip. Rev. Comput. Mol. Sci.* **2015**, *5*, 440–459.

(193) Sangtarash, S.; Sadeghi, H. Radical Enhancement of Molecular Thermoelectric Efficiency. *Nanoscale Adv.* **2020**, *2*, 1031-1035.

(194) Cui, L.; Miao, R.; Jiang, C.; Meyhofer, E.; Reddy, P. Perspective: Thermal and Thermoelectric Transport in Molecular Junctions. *J. Chem. Phys.* **2017**, *146*, 092201.

(195) Frisenda, R.; Gaudenzi, R.; Franco, C.; Mas-Torrent, M.; Rovira, C.; Veciana, J.; Alcon, I.; Bromley, S. T.; Burzurí, E.; van der Zant, H. S. J. Kondo Effect in a Neutral and Stable All Organic Radical Single Molecule Break Junction. *Nano Lett.* **2015**, *15, 3109-2114*.

(196) Herrmann, C.; Solomon, G. C.; Ratner, M. A. Organic Radicals As Spin Filters. *J. Am. Chem. Soc.* **2010**, *132*, 3682-3684.

(197) Mas-Torrent, M.; Crivillers, N.; Mugnaini, V.; Ratera, I.; Rovira, C.; Veciana, J. Organic Radicals on Surfaces: Towards Molecular Spintronics. *J. Mater. Chem.* **2009**, *19*, 1691-1695.

(198) Hayakawa, R.; Karimi, M. A.; Wolf, J.; Huhn, T.; Zöllner, M. S.; Herrmann, C.; Scheer, E. Large Magnetoresistance in Single-Radical Molecular Junctions. *Nano Lett.* **2016**, *16*, 4960-4967.

(199) Low, J. Z.; Kladnik, G.; Patera, L. L.; Sokolov, S.; Lovat, G.; Kumarasamy, E.; Repp, J.; Campos, L. M.; Cvetko, D.; Morgante, A.; Venkataraman, L. The Environment-Dependent Behavior of the Blatter Radical at the Metal–Molecule Interface. *Nano Lett.* **2019**, *19*, 2543-2548.

(200) Bejarano, F.; Olavarria-Contreras, I. J.; Droghetti, A.; Rungger, I.; Rudnev, A.; Gutiérrez, D.; Mas-Torrent, M.; Veciana, J.; van der Zant, H. S. J.; Rovira, C.; Burzurí, E.; Crivillers, N. Robust Organic Radical Molecular Junctions Using Acetylene Terminated Groups for C–Au Bond Formation. *J. Am. Chem. Soc.* **2018**, *140*, 1691-1696.

(201) Paniagua, J. C.; Mugnaini, V.; Gabellieri, C.; Feliz, M.; Roques, N.; Veciana, J.; Pons, M. Polychlorinated Trityl Radicals for Dynamic Nuclear Polarization: The Role of Chlorine Nuclei. *Phys. Chem. Chem. Phys.* **2010**, *12*, 5824-5829.

(202) Mugnaini, V.; Calzolari, A.; Ovsyannikov, R.; Vollmer, A.; Gonidec, M.; Alcon, I.; Veciana, J.; Pedio, M. Looking Inside the Perchlorinated

Trityl Radical/Metal Spinterface through Spectroscopy. *J. Phys. Chem. Lett.* **2015**, *6*, 2110-2106.

(203) Barr, C. L.; Chase, P. A.; Hicks, R. G.; Lemaire, M. T.; Stevens, C. L. Synthesis and Characterization of Verdazyl Radicals Bearing Pyridine or Pyrimidine Substituents: A New Family of Chelating Spin-Bearing Ligands. *J. Org. Chem.* **1999**, *64*, 8893-8897.

(204) Capozzi, B.; Xia, J.; Adak, O.; Dell, E. J.; Liu, Z.-F.; Taylor, J. C.; Neaton, J. B.; Campos, L. M.; Venkataraman, L. Single-Molecule Diodes with High Rectification Ratios through Environmental Control. *Nat. Nanotechnol.* **2015**, *10*, 522-527.

(205) Atesci, H.; Kaliginedi, V.; Celis Gil, J. A.; Ozawa, H.; Thijssen, J. M.; Broekmann, P.; Haga, M.; van der Molen, S. J. Humidity-Controlled Rectification Switching in Ruthenium-Complex Molecular Junctions. *Nat. Nanotechnol.* **2018**, *13*, 117–121.

(206) Gao, D.; Scholz, F.; Nothofer, H.-G.; Ford, W. E.; Scherf, U.; Wessels, J. M.; Yasuda, A.; von Wrochem, F. Fabrication of Asymmetric Molecular Junctions by the Oriented Assembly of Dithiocarbamate Rectifiers. *J. Am. Chem. Soc.* **2011**, *133*, 5921-5930.

(207) Díez-Pérez, I.; Hihath, J.; Lee, Y.; Yu, L.; Adamska, L.; Kozhushner, M. A.; Oleynik, I. I.; Tao, N. Rectification and Stability of a Single Molecular Diode with Controlled Orientation. *Nat. Chem.* **2009**, *1*, 635-641.

(208) Aragonès, A. C.; Darwish, N.; Ciampi, S.; Sanz, F.; Gooding, J. J.; Díez-Pérez, I. Single-Molecule Electrical Contacts on Silicon Electrodes under Ambient Conditions. *Nat. Commun.* **2017**, *8* , 15056.

(209) Yanson, A. I.; Bollinger, G. R.; van den Brom, H. E.; Agraït, N.; van Ruitenbeek, J. M. Formation and Manipulation of a Metallic Wire of Single Gold Atoms. *Nature.* **1998**, *395*, 783-785.

(210) Martinez, C. R.; Iverson, B. L. Rethinking the Term "Pi-Stacking." *Chem. Sci.* **2012**, *3*, 2191-2201.

List of Publications (published, and ready to submit)

- Naghibi, S.; Sahebi, H. Employment of modified Fe_3O_4 nanoparticles using thermo-sensitive polymer for extraction and pre-concentration of cefixime in biological samples. *Biomed. Chromatogr.* **2018**, 32, 1-11

- Naghibi, S.; Ismael, A.K.; Vezzoli, A.; Al-Khaykanee, M.K.; Zheng, X.; Grace, I.M. Synthetic Control of Quantum Interference by Regulating Charge on a Single Atom in Heteroaromatic Molecular Junctions. *J. Phys. Chem. Lett.* **2019.** 10 (20), 6419–24.

- Escorihuela, E.; Cea, P.; Bock, S.; Milan, D.C.; Naghibi, S.; Osorio, H.M. Towards the design of effective multipodal contacts for use in the construction of Langmuir–Blodgett films and molecular junctions. *J. Mat. Chem. C.* **2020**, 8 (2), 672–82.

- Naghibi, S.; Sangtarash, S.; Kumar, V.J.; Wu, J.; Judd, M.M.; Qiao, X. Redox-Addressable Single-Molecule Junctions Incorporating a Persistent Organic Radical. *Angew. Chem. Int. Ed.* **2022,** 1-11.

- Naghibi, S.; Herrer, L.; Marín, I.; Vezzoli, A.; Martín, S.; Cea, P.; Nichols, R.; Wire holder scaffolding based on Pillar[5]arenes for molecular electronics. *In preparation for publication soon.*

- Naghibi, S.; Nichols, R.; Martin, S.; Sangtarash, S.; Davidson, R. Characterisation, and determination of thiourea molecular junctions. *In preparation for publication soon.*